Electrical and magnetic studies on Bi-based perovskite –AFe_2O_4 (A=Co, Ni) composite structures

A

Thesis

by

MINTU TYAGI

(Regn. No. 901112016)

Submitted for the award of

DOCTOR OF PHILOSOPHY

Under the supervision of

Dr. Puneet Sharma
Associate Professor
SPMS, Thapar University

Prof. Ratnamala Chatterjee
Department of Physics IIT Delhi

School of Physics and Materials Science

Thapar University, Patiala-147004

(Punjab) India

July-2015

Dedicated to My Parents

CERTIFICATE

This is to certify that the thesis entitled, "**Electrical and magnetic studies on Bi-based perovskite –AFe_2O_4 (A=Co, Ni) composite structures**", being submitted by Mintu Tyagi for the award of the degree of Doctor of Philosophy (Ph.D) to the Thapar University Patiala, Punjab, is a record of bonafide research work carried out by him under our guidance and supervision.

In our opinion, the thesis has reached the standard of fulfilling the requirements of all the regulations related to the degree. The results contained in this thesis have not been submitted in part or full, to any other University or Institute for the award of any degree or diploma.

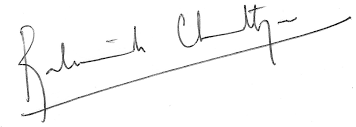

Dr. Puneet Sharma
Associate Prof. (SPMS)
Thapar university, Patiala-147004
(Punjab)

Prof. Ratnamala Chatterjee
Department of Physics
Indian Institute of Technology, Delhi
New Delhi – 110016, INDIA

Dated: 20th July 2015

Place: Patiala

ACKNOWLEDGEMENT

I am grateful to **GOD, MY PARENTS AND MY ELDER BROTHER (MONU TYAGI)** to provide me an opportunity to complete my Ph.D work.

First of all, I would like to express my deepest gratitude to my supervisors Dr. Puneet Sharma, Associate Prof. (SPMS) Thapar University, Patiala, Punjab and Prof. Ratnamala Chatterjee, Physics Department, IIT, Delhi, for their intellectual guidance, continuous interest, generous support and constant encouragement throughout my research work.

I am grateful to them to give me such an interesting topic (Multiferroics) for research, which could keep me fascinated throughout the period of research and would help me pursuing greater goals in future. I would especially like to mention that they provided a very healthy and enthusiastic environment in the labs that kept us motivated in our research activities. Being a very good researcher as well as teacher they are a very kind human being also. Apart from this I simply want to say that I cannot express my feelings in some words that how much they have done for me in this period.

I am very thankful to my doctoral committee members Dr. O. P. Pandey, Dr. B.C. Mohanty and Dr. Amjad Ali for their guidance, suggestions and support during my six months progress report. My special thanks are also to all the respective faculty of School of Physics and Materials Science, Dr. K.K. Raina, Distinguished Professor, Dr. N.K. Verma, Senior Professor, Dr. Kulvir Singh, Associate Dean, Dr. M.K. Sharma, Head of the department, Dr. S.D. Tiwari, Dr. D.P. Singh, Ms. Loveleen Brar, Dr. Alka Upadhyay, Dr. Punam Uniyal and Dr. Soumendu Jana for their encouragement and moral supports.

I would also thank to my lab members and friends for helping me during research work. I also thank the technical staff at Thapar University for their valuable help and technical support.

I greatly thank University Grant commission (UGC) and Department Of Science And Technology (DST), India for providing fellowship.

During my Ph.D work there are many people who helped in various stages. I could not able to write the names for those persons, but I am thankful to all those persons for their valuable support.

MINTU TYAGI

LIST OF PUBLICATIONS

1. **M. Tyagi**, Mukesh Kumari, R. Chatterjee, P. Sharma "Large Magnetoelectric Response in Modified BNT Based Ternary Piezoelectric [72.5($Bi_{1/2}Na_{1/2}TiO_3$)-22.5($Bi_{1/2}K_{1/2}TiO_3$)-5($BiMg_{1/2}Ti_{1/2}O_3$)] - Magnetostrictive ($NiFe_2O_4$) Particulate (0-3) Composite" **Appl. Phys. Lett. 106, 202904 (2015).**
2. **M. Tyagi**, R. Chatterjee, P. Sharma "Structural, optical and ferroelectric behavior of pure $BiFeO_3$ thin films synthesized by the sol-gel method" **J. Mater. Sci.-Mater. Electron**. 26, 1987–1992 (2015).
3. **M. Tyagi**, R. Chatterjee, P. Sharma "Improved dielectric and magnetic properties of multiferroic $BiFeO_3$-$NiFe_2O_4$ nanocomposite thin films" **J. Sol-Gel Sci. Technol.** 74, 692-697 (2015).
4. **M. Tyagi**, Mukesh Kumari, R. Chatterjee, A. Sun, P. Sharma "Electrical and Magnetic Properties of Multiferroic (1-x) $BiFeO_3$-x$CoFe_2O_4$ nanocomposite thin films derived by Sol-gel process**" IEEE Transactions on Magnetics**. 1, 2500704 (2014).
5. **M. Tyagi**, Mukesh Kumari, R. Chatterjee, P. Sharma "Raman scattering spectra, magnetic and ferroelectric properties of $BiFeO_3$-$CoFe_2O_4$ nanocomposite thin films structure" **Physica B.** 448 128–131(2014).
6. **M. Tyagi**, Mukesh Kumari, R. Chatterjee, P. Sharma "Magnetoelectric Coupling in Lead Free multiferroic [72.5($Bi_{1/2}Na_{1/2}TiO_3$)-22.5($Bi_{1/2}K_{1/2}TiO_3$)-5($BiMg_{1/2}Ti_{1/2}O_3$)] - ($CoFe_2O_4$) nanocomposites"(**Under Review).**

National and international conference attended

1. **Mintu Tyagi**, Ratnamala Chatterjee, Puneet Sharma "Synthesis and characterization of piezoelectric thin films for MEMS applications" National Seminar on Advanced Materials and Devices (NSAMD) held on (3-4 July, 2011) in GVM College Sonipat, Haryana, India.
2. **Mintu Tyagi,** Mukesh Kumari, Ratnamala Chatterjee, Puneet Sharma " Raman scattering spectra, ferroelectric and magnetic properties of $BiFeO_3$-$CoFe_2O_4$ nanocomposite thin films" International conference on magnetic materials and applications (MAGMA), held on (5-7 December, 2013) in IIT Guwahati, Assam-India
3. **Mintu Tyagi,** Mukesh Kumari, Ratnamala Chatterjee, Puneet Sharma "Improved dielectric and magnetic properties of multiferroic $BiFeO_3$-$NiFe_2O_4$ nanocomposite thin films" International conference on magnetic materials and applications (IC-MAGMA), held on (15-17 December, 2014) in Pondicherry university, Tamilnadu-India
4. 58^{th} DAE-SSPS Thapar University, Patiala-147004, Punjab
5. **Mintu Tyagi,** Ratnamala Chatterjee, Puneet Sharma "Optical and electrical properties of pure $BiFeO_3$ thin films synthesized by the sol-gel method" 23^{rd} Annual General Meeting on Functional Materials for Sustainable Energy and Advanced Technologies, held on (13-15 February, 2012) in Thapar University, Patiala-147004, Punjab
6. **Mintu Tyagi,** Ratnamala Chatterjee, Puneet Sharma "Electrical and magnetic properties of multiferroic $BiFeO_3$-$CoFe_2O_4$ nanocomposite thin films" National conference in advanced in engineering materials (NEAM) held on (20-22 March, 2015) in Department of Physics, Dehradun university, Dehradun-India
7. Workshop on NANO SCIENCE AND TECHNOLOGY (13-17 April, 2015), Beant College of engineering and technology, Gurdaspur-Punjab, India

TABLE OF CONTENTS

LIST OF FIGURES CAPTIONS

Chapter IV : Results and discussion

LIST OF TABLES

LIST OF SYMBOLS

d_{33} : Piezoelectric coefficient

k_p : Electromechanical coupling coefficient

λ_{11} : Magnetostriction coefficient

K_l : Manetocrystalline anisotropy constant

q_{11} : Piezomagnetic coupling coefficients

α_E : Mannetoelectric voltage coefficient

(V_{out}) : Induced output voltage

(H_{AC}) : AC magnetic field

ε_r' : Real part of dielectric constant

ε_r'' : Imaginary part of dielectric constant

ε_0 : Permittivity of Free Space

Rq :Root mean square roughness

f : Frequency

P : Polarization

P_r : Remnant Polarization

E : Electric Field

E_c : Coercive field (Electric)

T_c^{FE} : Ferroelectric Transition Temperature

M : Magnetization

H : Magnetic Field

M_r : Remnant Magnetization

M_s : Spontaneous Magnetization

T_C : Curie Temperature

T_N : Neel Temperature

H_c : Coercive Field (Magnetic)

k_B : Boltzmann Constant

λ : Wavelenght

R : Resistance

C : Capacitance

tan δ :Dielectric Loss

A :Area of the Electrode

t :Thickness of the sample

ABSTRACT

Multiferroic materials have recently drawn increasing interest and provoked a great number of research activities due to their potential applications for multifunctional devices. Multiferroism refer to any combination of ferroelectric and magnetic order parameters in single phase as well as in artificial composites. The coexistence of several interactions, particularly existence of a cross-coupling between ferroelectric and magnetic orders, known as "**magnetoelectric** (*ME*) **coupling**", brings about novel physical phenomena and offer possibilities for new multifunctional devices such as sensors, transducers, memories and spintronics. Observation of *ME* coupling in a material implies that the electric polarization/magnetization can be induced by application of magnetic/electric field; are termed as direct and converse *ME* effect respectively. Bismuth ferrite $BiFeO_3$ (BFO) is one of the most extensively studied single phase multiferroic having magnetic order (magnetic transition temperature T_N = 643 K) and ferroelectric order (ferroelectric transition temperature T_c^{FE} = 1103 K) at room temperature. However, magnetic properties of BFO is weak and limits its applications in electronic devices. Therefore, many approaches have been developed to improve the multiferroic properties by combining the ferroelectric and ferromagnetic orders named as artificial composite type materials. Among various non lead based multiferroic composites, Bi based multiferroic composites are most extensively studied. Recently, there is a surge in research on Bi based material e.g., BFO and ($Bi_{1/2}Na_{1/2}TiO_3$) BNT to be used as a ferroelectric/piezoelectric component for preparation of multiferroic composites. Therefore thesis focuses on the development of non lead Bi based multiferroic composites. In this work, studies based on sol-gel driven $BiFeO_3$-AFe_2O_4(A=Ni, Co) nanocomposite thin films and $Bi_{1/2}Na_{1/2}TiO_3$(BNT)-$Bi_{1/2}K_{1/2}TiO_3$(BKT)-$BiMg_{1/2}Ti_{1/2}O_3$(BMgT)-AFe_2O_4 (A = Co, Ni) particulate composites are presented.

The thesis is organized into five chapters

Chapter I (Introduction) gives a brief introduction about the multiferroic materials and need or advantages of the Multiferroic materials. The appropriate definitions of various terms related to the field (*e.g*, definitions of multiferroics, magnetoelectric coupling coefficient, types of multiferroicity) are given. Multiferroic materials are classified on the basis of single phase as well as composite structures. Further, composites are classified on

the basis of lead and non lead based composites. Finally the different connectivity schemes of composites have been discussed.

Chapter II (Literature Review) gives historical development in this field of multiferroic, followed by an extensive summary of the research carried out in single phase multiferroic as well as composite structures.

Chapter III (Experimental and characterization techniques) This chapter give details the processing methods employed for synthesizing the samples of different compositions. A brief details of the various characterization techniques used to study structural, microstructural, dielectric, ferroelectric, magnetic and magnetoelectric properties are provided.

Chapter IV (Results and discussion) In this chapter, the experimental results of the synthesized samples are presented. This chapter is organized in two sections. In the first section, preparation and characterization of BFO is discussed, followed by development of $BiFeO_3$-AFe_2O_4 (A = Co, Ni) composites are given. The effect of addition of ferrites in BFO matrix has been studied on their structural, dielectric, magnetic and ferroelectric properties. In the second section, studies based sol-gel assisted BNT-BKT-BMgT-AFe_2O_4 (A = Co, Ni) particulate magnetoelectric composites have been discussed. The effect of weight ratio of ferrites on their structural, dielectric, ferroelectric, magnetic and magnetoelectric properties has been systematically studied. Brief summary of the results are give below:

Studies on BFO thin films

This study details the work on BFO thin films annealed at different temperature. BFO thin films were synthesized by the sol-gel spin-coating technique followed by annealing at different temperatures. The effect of annealing temperature on structural, dielectric and ferroelectric properties of BFO thin film has been investigated. Single phase polycrystalline BFO films are confirmed by X-ray diffraction patterns. A strong dependence of grain size and shape on annealing temperature was observed. The film annealed at 500 ºC showed a well saturated polarization-electric field loops. The remnant polarization and saturation polarization values are decreased with increasing annealing temperature. The anomaly in temperature dependent dielectric permittivity was observed at magnetic transition point.

Studies on $BiFeO_3$-$CoFe_2O_4$ composite thin films

In this study (1-*x*)BFO–*x*CFO (*x* = 0, 0.1, 0.2, 0.3) nanocomposite thin films were deposited using sol-gel spin coating technique. The annealing of the films were carried out at 600ºC and 650 ºC. X-ray diffraction, transmission electron microscopy examinations confirm the coexistence of both perovskite BFO and spinel CFO phases. The magnetic and dielectric properties are improved by incorporation of CFO grains in matrix of BFO. The saturation magnetization (M_s) increases as *x* varies from 0 to 0.3. For *x* = 0.3, M_s is found as high as ~ 115 emu/cm^3 and 158 emu/cm^3 for the films annealed at 600ºC and 650 ºC respectively. Coercivity is increased with CFO concentration and found maximum (H_c ~ 107 Oe) for *x* = 0.30. However for x=0.3, ferroelectric behaviour degraded for the films annealed at 600 ^{o}C and 650 ^{o}C. Higher magnetic content as well as bismuth loss with increasing annealing temperature is responsible for decrease the ferroelectric behaviour.

Studies on $BiFeO_3$–$NiFe_2O_4$ composite thin films

In this part of the thesis (1-*x*)BFO–*x*NFO (*x* = 0, 0.1, 0.2, 0.3) nanocomposite thin films were prepared by sol-gel technique and their structural, electrical and magnetic properties were studied. X-ray diffraction and transmission electron microscopy examinations confirmed that NFO nanoparticles were well distributed in BFO matrix. The magnetic and dielectric properties were significantly improved by incorporation of NFO nanoparticle in matrix of BFO. The saturation magnetization (M_s) and remnant magnetization (M_r) increased as high as ~34 emu/cm^3 and ~7 emu/cm^3 respectively for *x* = 0.1. The dielectric constant of the films increased from 160 (for *x* = 0) to 280 (for *x* = 0.3). However**,** the values of ferroelectric polarization were decreased with increasing *x*. Importantly, the sample with (*x* = 0.1),the best sample in this study demonstrates improved ferroelectric as well as magnetic properties.

Studies on BNT-BKT-BMgT/NFO Particulate composite

This section discusses the details of modified BNT based magnetoelectric composites. In first part of this section the results on BNT-BKT-BMgT/NFO (where *x*=0, 0.1, 0.2, 0.3) *ME* composite have been discussed. The effect of NFO weight ratio on the structural, dielectric, ferroelectric, magnetic and magnetoelectric properties has been systematically studied. Lead free ternary solid solution 72.5BNT-22.5BKT-5BMgT) with effective piezoelectric

coefficient (d_{33}) of 180 pC/N has been prepared. Further, particulate composite consisting of $(1-x)$[72.5(BNT)-22.5(BKT)-5(BMgT)]$-x$NFO (x = 0, 0.1, 0.2, 0.3) were synthesized and its magnetoelectric (*ME*), magnetic, ferroelectric and dielectric properties were studied. The composite with x = 0.2, showed the large value of *ME* voltage coefficient (α_E) ~73 mV/cmOe accompanied by higher d_{33} (~125 pC/N). The temperature dependent dielectric spectra of samples indicated two anomalies at 200 °C and 320 °C are ascribed to ferroelectric to antiferroelectric, and anti-ferroelectric to paraelectric phase transitions respectively.

Studies on BNT-BKT-BMgT/CFO Particulate composite

In this study the results on BNT-BKT-BMgT/CFO (where x = 0, 0.1, 0.2, 0.3) particulate *ME* composite are discussed. As prepared lead free ternary solid solution 72.5(BNT)-22.5(BKT)-5(BMgT) was used to synthesis of $(1-x)$[72.5(BNT)-22.5(BKT)-5(BMgT)]$-x$$CoFe_2O_4$ (CFO) (x = 0, 0.1, 0.2, 0.3) particulate composite. Further its structural, dielectric, ferroelectric and magnetoelectric properties were studied. The composite showed that the ferroelectric as well as ferromagnetic properties are sustained in the composite. The composite with x = 0.2, is the best sample of our series having large value of *ME* voltage coefficient (α_E) ~112 mV/cmOe. The temperature dependent dielectric anomalies are found similar to NFO based composites.

Chapter V (Conclusions and future scope) gives an important conclusions and future scope in this field of research.

.

CHAPTER I

INTRODUCTION

Overview

This chapter gives a brief introduction about the multiferroic materials and need or advantages of the Multiferroic materials. The appropriate definitions of various terms related to the field (*e.g*, definitions of multiferroics, magnetoelectric coupling coefficient, types of multiferroicity) are given. Multiferroic materials are classified on the basis of single phase as well as composite structures. Further, composites are classified on the basis of lead and non lead based composites. Finally the different connectivity schemes of composites have been discussed.

1.1 Multiferroic materials

The materials, which simultaneously posses more than one of the ferroic order parameters like ferroeletricity, (anti-) ferromagnetism and ferroeleasticity termed as **"multiferroics"** **[1-5].** Among them, the coexistence of ferroelectricity and ferromagnetism is highly desired for magnetoelectric (*ME*) materials. Recently, *ME* materials have attracting increasing interest and offer a significant technical promise for potential applications in novel multifunctional devices such as sensors, transducers, memories and spintronics **[3-7].** Usually, a spatial class of materials in literature exhibit the ferroelectric and ferromagnetic order simultaneously **[2, 3].** Basically, the ferroelectricity is the property of materials which contain spontaneous stable electric polarization behaviour which is switchable in presence of an applied electric field are called ferroelectric materials **[2, 4]**. On the other hand the ferromagnetism contain the stable magnetization and the magnetic dipoles can be tuned by the external applied magnetic field are called the ferromagnetic materials. Moreover, the term '**multiferroic**' also extensively used in literature for the materials in which ferromagnetism and ferroelectricity coexist in the same phase as well as the multiphase composite type materials **[8-13].**

Recently, a huge interest has been paid to **multiferroic magnetoelectric (*ME*)** materials not only because they exhibit simultaneously both ferroelectric/piezoelectric and ferromagnetic properties, but also a coupling interaction between the different orders lead to additional functionalities called as *ME* effect **[6, 7].** In such materials the observation of *ME* coupling implies that magnetic field control the magnetic spins but electric dipoles as well and vice versa. This additional functionality offer an attracted renewed interest toward multiferroic *ME* materials for several scientific and technological importance **[5-13].**

The concept of multiferroic/magneto-electrics pictorially depicted by several authors using a schematic diagram as shown in Fig. 1.1**[1, 2]**. The intersection (red hatching) represents materials that are multiferroic and the blue hatching represents the materials that would show *ME* coupling. In principle the coupling between two order (piezoelectric/ferroelectric and ferromagnetic) parameter permit the data to be written

electrically and read magnetically. These attractive features make them very useful for ferroelectric random access memory (Fe-RAM) and magnetic data storage devices**[14].**

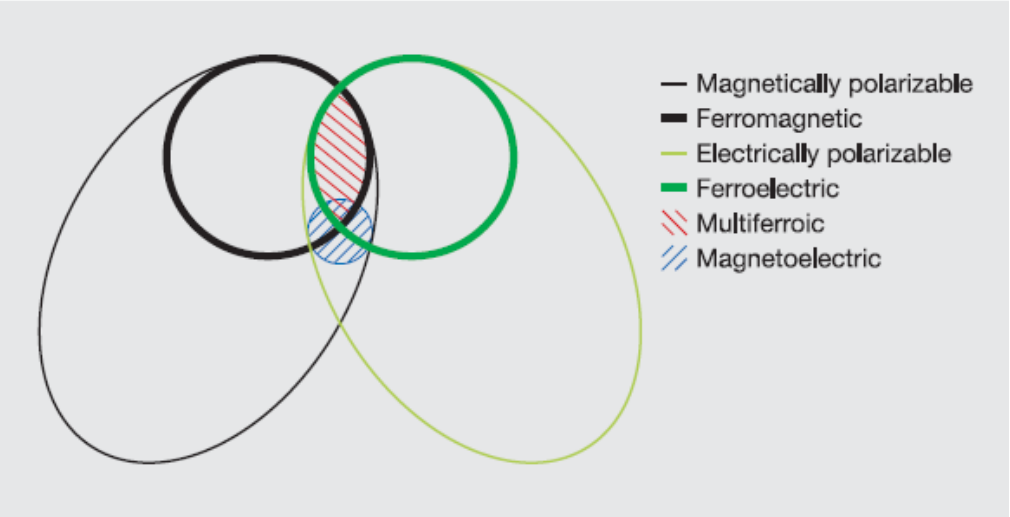

Fig. 1.1 : The relationship between the multiferroic and magnetoelectric materials **[1].**

The *ME* coupling in multiferroic materials is traditionally described in Landau's theory **[15]** by writing the free energy (F (E, H) equation for magneto-electrically system in terms of applied magnetic and electric fields. Here E and H denotes the electric and magnetic fields respectively. For ferroic materials the free energy equation is given by;

$$F(\vec{E},\vec{H}) = F_0 - P_i^S E_i - M_i^S H_i - \frac{1}{2}\varepsilon_0\varepsilon_{ij}E_iE_j - \frac{1}{2}\mu_0\mu_{ij}H_iH_j - \alpha_{ij}E_iH_j - \frac{1}{2}\beta_{ijk}E_iH_jH_k - \frac{1}{2}\gamma_{ijk}H_iE_jE_k \ldots\ldots \quad (1.1)$$

Where P_i^S and M_i^S are the spontaneous polarization and magnetization respectively.

The magneto-electric effect can easily be established in the form of polarization P_i (H_j) and magnetization M_i (E_j). Differentiation of equation (1.1) with respect to electric field E_i gives the polarization

$$P(\vec{E},\vec{H}) = -\frac{\partial F}{\partial E_i} = P_i^S + \varepsilon_0 \varepsilon_{ij} E_j + \alpha_{ij} H_j + \frac{1}{2}\beta_{ijk} H_j H_k + \gamma_{ijk} H_i E_j - ..... \quad 1.2$$

Similarly the differentiation of equation (1.1) with respect to magnetic field H_i gives magnetization

$$M_i(\vec{E},\vec{H}) = -\frac{\partial F}{\partial H_i} = M_i^S + \mu_0 \mu_{ij} H_j + \alpha_{ij} E_i + \beta_{ijk} E_i H_j + \frac{1}{2}\gamma_{ijk} E_j E_k - ..... \quad 1.3$$

The tensor quantity $\alpha_{ij}(T)$ quantifies the induction of polarization by a magnetic field or of magnetization by an electric field which is used to describe as **linear magneto-electric coupling coefficient** in the system. The tensors β_{ijk} (T) and γ_{ijk} (T) are associated with the higher order magneto-electric coupling coefficients. The majority of research on multiferroic magnetoelectric materials are focused on **linear magneto-electric coupling coefficient.**

1.2 Classification of multiferroic *ME* materials

The multiferroic *ME* materials can be divided into single phase and composite type (artificial) multiferroics

1.2.1 Single phase multiferroics

So far, many compounds have been investigated as single phase multiferroic *ME* materials such as BFO and rare-earth magnetite **[15-21]**. However, all the single phase multiferroic materials are not very much useful for the technical importance because of anti-ferromagnetic nature and their associated Neel temperature much below the room temperature **[18, 19, 21]**. The single phase multiferroics are further divided in two types. The type-I multiferroics contain perovskite compounds with independently originating ferroelectricity (cations at A-site) and ferromagnetism (cations at B-site). BFO, $YMnO_3$, $BiMnO_3$ are the examples of type–I multiferroic materials **[15-21].** Among the **type-I multiferroics**, BFO is perhaps one of the most commonly studied

multiferroic with high Neel (T_N = 643 K) and Curie (T_c^{FE} = 1103 K) temperature far above room temperature. BFO exhibits the spontaneous electric polarization directed along one of the [111] directions of the perovskite structure (fig1.2) **[16, 17]**.

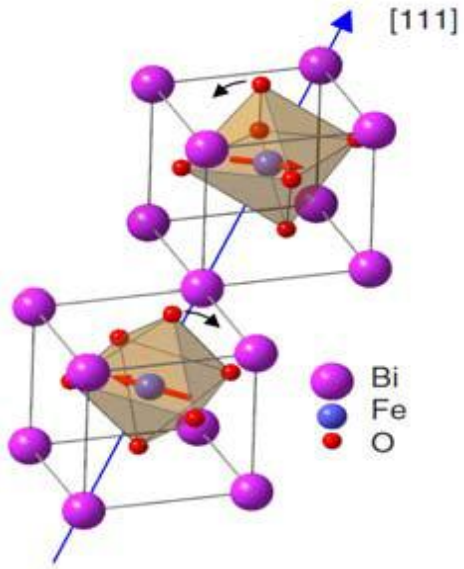

Fig. 1.2. Crystal structure of BFO **[20]**

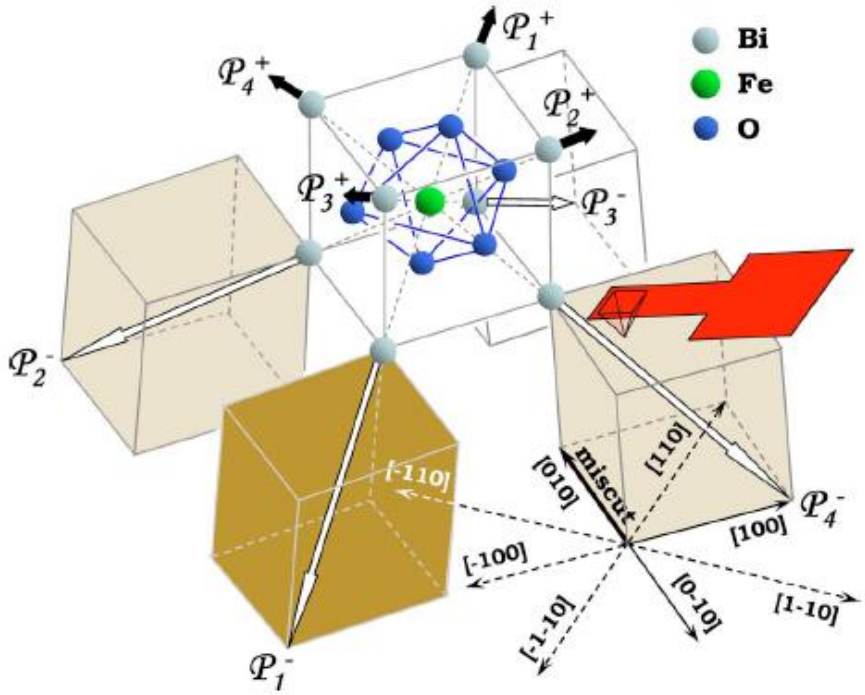

Fig. 1.3. A schematic picture of the four different structural variants in (001) rhombohedral films. Pi ± {i =1,4} denote the polarization vectors. The central unit represents the perovskite building block of the rhombohedral structure **[21].**

Basically, the ferroelectric state of BFO is attributed to a large displacement of the Bi ions relative to the FeO_6 octahedra. Moreover, the polarization of BFO along the <111> direction, leading to the formation of eight possible polarization directions (positive and negative orientations along the four cube diagonals, Pi ± with I = {1,4}) which correspond to four structural variants (fig. 1.3) **[15, 21]**.

Being a good ferroelectric the major drawback of weak magnetic behaviour due to G-type anti-ferromagnetic nature and weak coupling between two order parameters hinder their practical applications. **[16, 17]**. Various studies are reported for magnetic structure of BFO using XRD, neutron diffraction and Mossbauer measurements. As per their report, the spin ordering in BFO shows incommensurate cycloid spin structure of the anti-ferromagnetically ordered sublattices. This cycloid has a very long repeat distance of 62-64 nm, and a propagation vector along the direction as shown in fig.1.4. The magnetic structure of BFO showed that each Fe^{+3} spin is surrounded by six anti-parallel spins on the nearest Fe neighbors as shown in fig.1.5. In fact the spins are not anti-parallel, as there is a weak canting magnetic moment caused by local magnetoelectric coupling to the polarization.

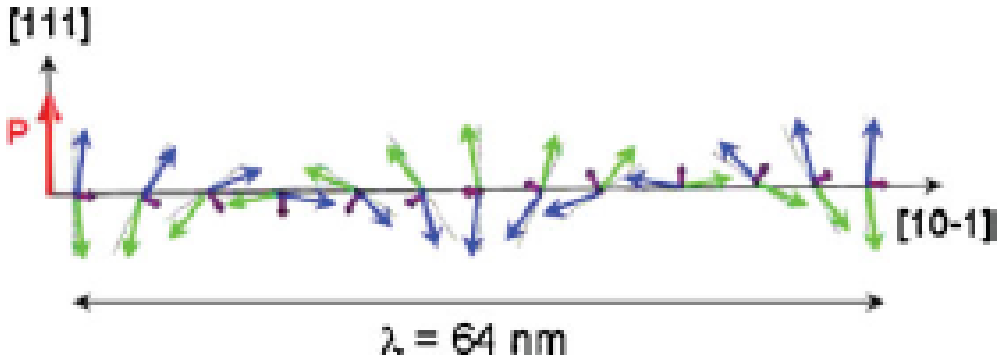

Fig. 1.4 Schematic representation of the spin cycloid. The canted antiferromagnetic spins (blue and green arrows) give rise to a net magnetic moment (purple arrows) that is spacially averaged out to zero due to the cycloidal rotation **[16].**

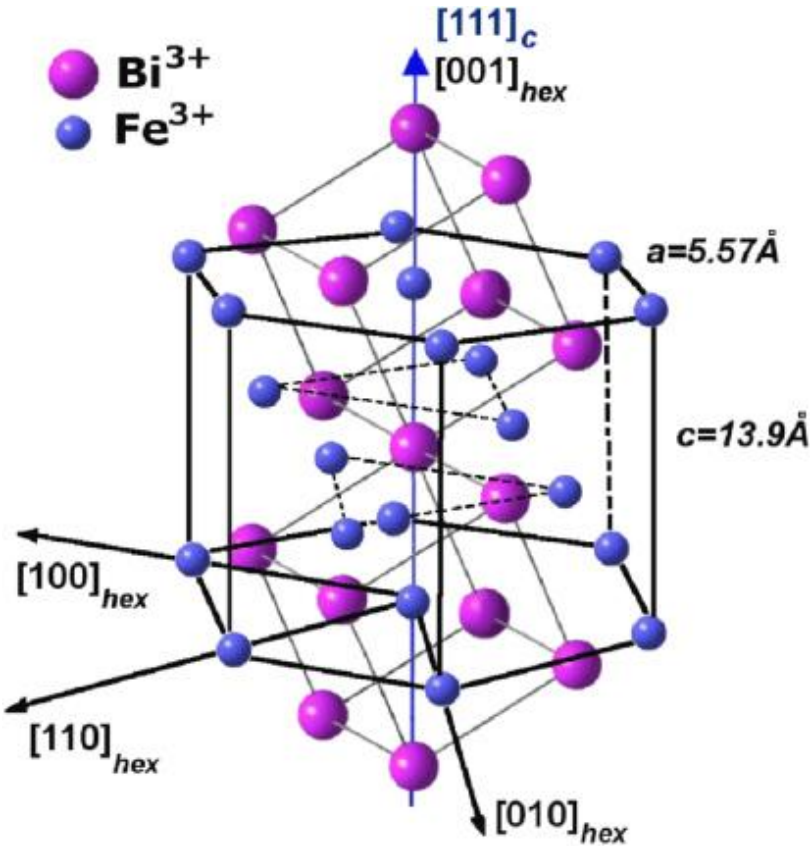

Fig. 1.5. Schematic presentation of the $BiFeO_3$ unit cell in the hexagonal and pseudo cubic settings of *R*3*c* space group. The blue arrows indicate the Fe^{3+} moment direction **[12].**

The type II multiferroics includes the materials exhibiting rather low ferroelectric as well as magnetic transition temperatures which excludes their applications in multiferroic devices. $TbMnO_3$ and $TbMn_2O_5$, a perovskite having anti-ferromagnetic ordering at T_N = 41K and the second magnetic transition at T_N = 28K are examples of type II multiferroics **[22, 23].** The low temperature magneto-electric coupling in such compounds was discovered by Kimura *et al* **[22].** However, as compared to type I multiferroics the polarization in these materials is rather small (10^{-2} μC/cm^2) **[21-25].**

1.2.2 Multiferroic magneto-electric composites

Due to small room temperature magneto-electric coupling coefficient in single phase multiferroic materials, the focus of the researchers are shifted to the *ME* composites. multiferroic *ME* composites, where an artificial room temperature coupling is engineered between two ferroic order parameters like ferroelectric/piezoelectric and

ferri/ferromagnetic are of particularly interest. Several strategies have been envisaged to achieve high *ME* coupling in composite materials **[10, 11, 13].** Many approaches have been explored to develop strain induce coupling between the piezoelectric (via the piezoelectric effect) and magnetic (via the magnetostriction) phase **[10, 11].** In order to achieve large *ME* response in such composites, the piezoelectric and magnetostrictive phase should have a high value of piezoelectric co-efficient and magnetostrictive co-efficient respectively along with high resistivity. Structurally, *ME* coupling coefficient in particulate composites should posses adequate interface contact between the two phases for better strain induced coupling. Also piezoelectric and piezomagnetic phases should be chemically inert to avoid any inter-diffusion during sintering which may deteriorate *ME* response of composites. The mechanism of *ME* effect in composite materials can be described as shown in figure 1.6.

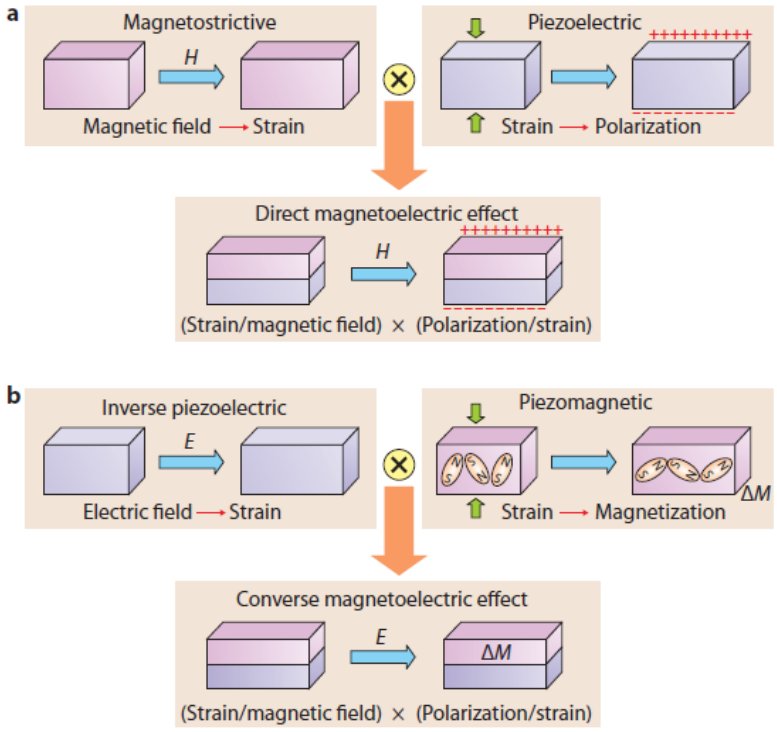

Fig. 1.6. Systematic illustration of *ME* effect in composite materials **[8].**

For the fabrication of *ME* composites lead based piezoelectric ceramics such as $PbZrTiO_3$(PZT) is the primary choice owing to its high dielectric constant and piezoelectric coefficient and extensively studied. However, Pb is a toxic in nature and environmentally hazardous. Thus, due to toxicity of lead, the research interest is now shifted toward the non lead based piezoelectric materials used for preparation of multiferroic *ME* composites. The various constituents which have been used ferroelectric as well as magnetic constituents for synthesis of *ME* composites are shown in table 1.

Table 1.1 Various constituent phases used for preparation of multiferroic *ME* composites.

Piezoelectric components	Magnetostrictive components
PZT	CFO
BT	NFO
PT	LSMO
BNT	ZFO
PMN-PT	NZFO
Terfenol-D	CZFMO

Most of the investigated lead free multiferroic *ME* composites are based on BFO, BT and $Bi_{0.5}N_{0.5}TiO_3$(BNT) used as piezoelectric components **[26-30].** There are several reports on non lead based multiferroic composites using BFO as ferroelectric/piezoelectric component and spinel ferrites as magnetic component. BFO itself a well studied single phase multiferroic material as discussed above**[26-30].** But, the major drawback of weak magnetic behaviour of BFO limit its use for multifunctional device based applications **[30].** This week magnetism in BFO can be improved by modification with ferrite oxides in the form of composites **[31-35].** Further, modification in BFO in the form of BNT or modified BNT based ferroelectric/piezoelectric materials by several researcher lead to improvement in dielectric and piezoelectric response which could be a potential piezoelectric candidate for preparation of non lead based *ME* composites.

The BNT based piezoelectric materials recently have been focused as an alternate of lead based piezoelectric materials for multiferroic *ME* composites. However, high piezoelectric coefficient (d_{33} ~ 600pm/V) and high electromechanical coupling coefficient (k_p ~ 0.7) of PZT is difficult to match with other non lead based piezoelectric materials **[36].** Therefore, to improve its piezoelectric properties, BNT has been modified with solid solutions of $BaTiO_3$(BT), $(Bi_{0.5}K_{0.5})TiO_3$ (BKT), $(K_{0.5}Na_{0.5})NbO_3$ (KNN) and $Bi(Mg_{0.5}Ti_{0.5})O_3$ (BMgT) **[37-40].** Recently, Jarupoom *et al*. reported d_{33} values greater than 500pm/V in ternary 72.5BNT-22.5BKT-5BMgT based solid solution **[41].** Hence, this modified ternary solid solution could be a potential candidate for lead free multiferroic *ME* composites. In addition to choices of ferroelectric/piezoelectric component, the selection of magnetic component based on the magnetostriction, resistivity, permeability and chemical stability also important for better performance of *ME* composites. Thus the choice for magnetostrictive materials narrows down toward the spinel ferrites $NiFe_2O_4$(NFO), $CoFe_2O_4$(CFO) having high values of magnetostriction coefficient and good chemical stability **[42-45].**

Further, based on structure, multiferroic *ME* composites can be divided in two categories; Bulk composite structure and thin films composites.

1.3. Bulk composite structure

Bulk composites are designed using various connectivity schemes such as 0-3 type particulate composite consists of ferri/ferromagnetic particles dispersed in ferroelectric/piezoelectric matrix, 2-2 type laminate composites connecting two dimensionally (e.g., a bilayers or multilayer) between two constituent phases and 1-3 type composite structure with one phase of fiber embedded in the matrix of another phase **[33, 42, 43, 47-51].** In composite structures the various connectivity schemes between individual components plays an significant role in determining the overall properties of composite structures. Among them, 0-3 type particulate composites are easily prepared using the conventional solid state method as well as sol-gel method.

1.4. Thin films composites

An interest toward multiferroic composites has been driven by the development of various thin films growth techniques. Thin films offer a pathway to discover a number of new high quality multiferroic composites. Recently, various growth techniques are used to fabricate the variety of thin films including, spin coating, sputtering, metal-organic chemical vapor deposition, pulse laser deposition, molecular beam epitaxy and more **[8, 9, 11, 12, 31, 34, 35].** multiferroic *ME* composite thin/thick films structures can also be divided into three types based on microstructural point of view: (i) a 0-3 structure, which is generally a magnetic component distributed in a ferroelectric/piezoelectric matrix, (ii) a 2-2 structure, which is generally multilayer thin films of magnetostrictive and piezoelectric materials, and (iii) 1-3 structure, such as monolayer self-assembled nanostructures. The schematic illustration of *ME* composites with different connectivity schemes are shown in fig.1.7 **[8].**

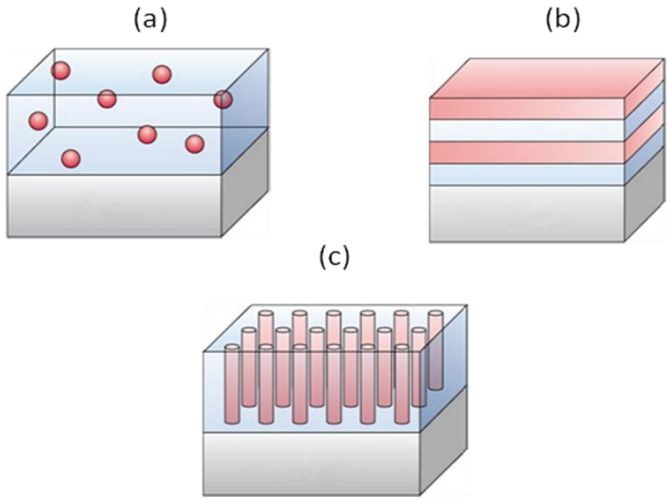

Fig. 1.7: Schematic illustration of three ME composite films with the three common connectivity schemes: (a) 0-3 particulate composite, (b) 2-2 laminate composite, and (c) 1-3 fiber/rod composite films **[8].**

MOTIVATION

Functional ferroelectric and magnetic materials are a vital part of modern technology. Recently magnetic materials are extensively used for data storage devices, such as hard disk drives and ferroelectric materials having spontaneous polarization are used for ferroelectric random access memories (FE-RAMs). Moreover, the ferroelectric materials having favourable piezoelectric properties also have been employed for vide range of applications including actuators/transducers and surface acoustic wave (SAW) devices. In recent years, the spurred research interest towards device miniaturization paid huge attention by combining ferroelectric and magnetic materials into multifunctional devices to perform more than one task. Therefore, the focus of researchers has shifted towards the development of Multiferroic composites. Artificial synthesis of *ME* devices solve the problem of weak *ME* coupling that exists in single phase Multiferroic materials, since the intrinsic electric and magnetic properties can be tuned by application of magnetic and electric field respectively.

Still, there are some open questions for researchers from the view point of choice of materials. *ME* composites consisting of piezoelectric and magnetostrictive are widely studied in literature. More emphasis is given to lead based piezoelectric oxide e.g, PZT to synthesis of *ME* composites. However, due to the toxic nature of Pb, the non lead based *ME* composites were also studied. Looking among the non lead based oxides, $Ba(ZrTi)O_3$ (BZT), $BaTiO_3$ (BT), BFO and BNT are the well known piezoelectric materials and can be used for synthesis of non Pb based *ME* composites.

Therefore, the focus of the thesis is to investigate ferroelectric, magnetic and magnetoelectric properties of non lead Bi-based perovskite and spinel composites. The BFO and modified BNT is chosen as ferroelectric and CFO/NFO as magnetic phase for the fabrication of multiferroic composites.

CHAPTER II

LITERATURE REVIEW

Overview

This chapter gives historical development in this field of multiferroic, followed by an extensive summary of the research carried out in single phase multiferroic as well as composite structures.

2.1 Historical background of multiferroics

The basic idea about the multiferroic materials dates back to as early as 1894, when Pierre Currie originated the concept that the crystal could be simultaneously ferroelectric and ferromagnetic **[52].** However, no further work was reported on multiferroic materials until 1958 when possibility of the polarization P and magnetization M in certain crystals on the basis of the crystal symmetry proved by Landau and Lifshitz **[15].** It was first theoretically predicted multiferroic properties in Cr_2O_3 by Dzyaloshinskii in 1960 and further experimentally confirmed in that materials by Astrov in the temperature range of 80 to 330 K. **[53, 54].** Despite the number of theoretical and experimental investigations concerning the coupling interactions between order parameters in multiferroic materials, the field languished a number of years **[55, 56, 57, 58].** The study toward multiferroics re-energized when the Kimura and co-workers realized the catalysing results in TbMnO3 **[59].** In this report Kimura *et al* found the observation of magnetically controlled electric order and vice-versa and interaction between order parameters. This strong correlation between spins and charge provide a new track for investigators toward multiferroic materials.

Many other single phase compounds have been investigated as multiferroic *ME* materials such as well known perovskite BFO, and hexagonal manganites $YMnO_3$**[60].** But, all the single phase multiferroic *ME* materials suffer from the major drawback of considerably weak *ME* behaviour at room temperature. Among all the promising single phase multiferroic material, Smolenskii's group started to study of bismuth ferrite, and found bismuth ferrite samples were highly conducting caused by oxygen vacancies created during the processing of the samples **[61].** The ferroelectric measurements performed by several authors on bulk BFO samples in 1960s and 1970s yielded only small values of polarization.

Several authors tried to solve the conductivity problem in BFO by doping other ions at different lattice sites (A and B sites both) **[62, 63-65].** Still problem was the same and no practical use devices were obtained. However, Teague *et al.* reported the small value of polarization (P_r = 6μC/cm^2) with lack of saturated ferroelectric loops for single crystal BFO and they also remarked that the actual polarization value may be

higher by an order of magnitude **[57].** To overcome the conductivity problem as well as improve the ferroelectric properties, an interest has been paid by several author toward the development of thin films. Various growth techniques including sputtering, pulsed laser deposition, spin coating, molecular beam epitaxy, chemical vapor deposition and more, offer a pathway to preparation of high quality thin films material for future potential applications **[26-28].**

2.2 Single phase multiferroic thin films

Ramesh group started work on the growth and properties of single phase multiferroic BFO thin films in 2003. The high quality BFO thin films were prepared with large value of remnant polarization (P_r ~ 60μC/cm^2). The reported P_r value in such BFO thin films was the 15 times larger than previously reported in bulk BFO samples **[27, 66].** This work motivated the other groups to work in this area, e.g., Yun *et al.* in 2003, also prepared and report the prominent ferroelectric behaviour for BFO thin films having saturated *P-E* loops with ($2P_r$ = 71.3μC/cm^2), ($2E_c$ = 125 kV/cm) and stable current density **[67].** Yun *et al.* continued the work on BFO thin films and their structural and *RT* multiferroic properties were studied. The effect of deposition pressure on their crystal structure and multiferroic properties have been investigated. The stable current density with well saturated *P-E* hysteresis loops are observed **[68].**

An alternative ways have been adopted to solve the issue of leakage current in BFO thin films. The substitution on the Bi and Fe sites improved the electrical properties of BFO thin films **[69-72].** The substitution on Bi site greatly suppressed the bismuth loss during the annealing process of the films causing to reduce the leakage current of the films **[69-72].** The substitution of ions also showed change its phase transition from rhombohedral-orthorhombic-cubic as a function of pressure **[73, 74].** The effect of chemical pressure induced by iso-valent ions substitution with different ionic radii was also investigated. Most commonly used ion, substituted for Bi^{3+} is La^{3+} which enhanced the ferroelectric properties by reducing the bismuth loss at A site of BFO **[73, 74].** Further, to improve the ferroelectric properties with sufficiently remnant polarization values, BFO has also been modified with Ce at bismuth site. Ce which belong to the family of lanthanides and the ionic radii of La (0.101 nm) and Ce

(0.103nm) are approximately similar to Bi (0.103). Quan *et al.* prepared Ce doped $Bi_{0.80}Ce_{0.20}FeO_3$ thin films and improved remanent polarization value of ($2P_r$ ~ 3.12 μC/cm^2), due to the structural distortion of BFO and the reduction in oxygen vacancies **[75].** Wang *et al*. also reported an improvement in remnant polarization and leakage current density value by Ce doping at the Bi site **[76].** Other Nd doped single-phase BFO ($Bi_{1-x}Nd_xFeO_3$ where x = 0 – 0.2) multiferroic thin films were fabricated to study the effect of Nd doping on their Raman scattering spectra and ferroelectric properties. The evolvements of different normal modes of Raman scattering spectra suggests that the structural change is accompanied by increasing x along with good ferroelectric order **[77].**

Still, a considerable drawback that limits their multifunctional applications was the weak magnetic behaviour such as low saturated magnetization (M_s) and remnant magnetization (M_r) because of G-type antiferromagnetic structure with nearest neighbour spin canting **[29, 30].** Therefore, to overcome deficiency of single-phase multiferroics an attempts have been made to develop composite type artificial multiferroics to provide innovative approach to improve magnetic properties as well as the magnetoelectric coupling mechanisms. The current research also focussed on the class of composite-type artificial multiferroics materials in thin film nano-heterostructures. It was observed that composite-type multiferroic materials which mainly include both ferroelectric and magnetic phases, yield a massive *ME* coupling coefficient even above room temperature.

2.3 Composite multiferroics

Van Suchtelen and his group proposed the concept of bulk multiferroic *ME* composites in 1972 at Philips Laboratories in Netherlands **[46].** Although, the experimental values of *ME* voltage coefficient calculated by Suchtelen were far below the theoretically predicted for bulk composites **[46, 77-79]**. Few groups from USA, Russia, and India were involved in the preparation multiferroic bulk *ME* composites via conventional solid state method in early 1990s. However, the values of *ME* coefficient for these particulate composites were too small around 1 mV/cmOe. Before year 2000, the development in the field of two phase bulk multiferroic *ME* composites

considering the ferroelectric/piezoelectric and ferrites as components did not get much attention **[80, 81]**. Also the experimental studies of composites did not present a great step forward. However, the experiments inspired to researchers for some theoretical works in the field of *ME* composites. In that period the most of the works was theoretical and proved the quantitative understanding of the bulk multiferroic *ME* composites. An upsurge interest toward multiferroic *ME* composites created in the early 2000 due to the appearance of giant magnetostriction in rare-earth-iron alloy $Tb_{1-x}D_yFe_2$ (Terfenol-D) **[82, 83]**. Ryu *et al.* (2001) prepared bulk *ME* composite and the effect of sintering temperature on their microstructure and *ME* behaviour has been studied **[83].** It was found that the sintering temperature played a key role for preparation of *ME* composite and the higher value of *ME* coefficient about 10-100 mV/cm Oe have been obtained in this composite structure **[82].**

Dong *et al.* 2003 have also been reported the bulk *ME* composites and the *ME* coefficient of the order of $1Vcm^{-1}Oe^{-1}$ in Terfenol-D based bulk *ME* composites was observed both in experimental as well as theoretical studies **[84].** The high value of *ME* voltage coefficient in such composites made them attractive for technological applications. However, Terfenol-D based *ME* composites are brittle in nature and also exhibit high eddy current losses. To reduce the eddy current losses and overcome the problem of brittleness of the Terfenol-D based composites, the three phase composites of Terfenol-D/Piezoceramics/Polymers have been reported **[85-88].** These three phase composites have been reported with different connectivity schemes including 0-3, 2-2 and 1-3. The value of *ME* voltage coefficient of the order of 0.1 V/cm Oe was observed at room temperature in such multiferroic *ME* composites **[85-90]**.

Moreover, there are several choices in literature for preparation of *ME* composites depending on the piezoelectric coefficient, permittivity, permeability, sintering temperature, chemical reactivity as well as magnetostriction coefficients of the ferrites. In this sprit, many researchers tested a number of multiferroic *ME* composite materials by combining a piezoelectric as well as ferrite phase using different connectivity schemes. These multiferroic composites were considered to produce large value of *ME* coefficients. The *ME* coefficients of these bulk composites were observed in the range

of 10 to 100 mV/cmOe depending on preparation method and respective compositions **[13, 90-98].** However, the *ME* values so far observed in such particulate composites were far below than that theoretically predicted due to inherent preparation problems in such composites like thermal expansion mismatch and the inter-diffusion during high temperature sintering process at the interface between two phases **[91-96].** The large thermal expansion coefficient between two phases leads to lower densification as well as the micro-cracks in the composite samples. Moreover, the high temperature sintering process in such composites yields the unwanted impurity phases by chemical reaction and inter-diffusion at the interface. For example, the $BaFe_{12}O_{19}$ and $BaCo_6Ti_6O_{19}$ were observed in $BaTiO_3/CoFe_2O_4$ composite structures **[13, 96-98].**

These impurity phases were deteriorate the piezoelectricity of the piezoelectric phase and the magnetostriction coefficient of the magnetic phase and also reduce the strain transfer between two constituent phases. Different techniques were employed to overcome the problem of lower densification and achieve sufficient bulk density of composite samples as well as to avoid the possible chemical reactions at the interface between two constituent phases **[99-102].** The spark plasma technique was employed by G. Srinivasan *et al.* in 2004 to replace the conventional sintering **[101].** Further, spark plasma technique was employed by Q. H. Jiang *et al.* in 2007 and found to be large improvement in the *ME* behaviour of the composite samples as compared to conventional sintering process **[102].** Especially, the short time and low sintering temperature is required for the efficient sintering of the samples, which reduces the possibility for unwanted reaction to occur. For example, PZT/NFO multiferroic composite with relative density of about 99% was prepared using spark plasma sintering technique **[101].** Moreover, sol-gel method was also employed by Ren *et al.* in order to achieve good mixing of two powders and reduce the unwanted phases at the interface of piezoelectric BTO and CFO ferrite oxides **[13].** The *ME* coefficient value of the samples was approximately three times larger than that prepared by conventional solid state reaction route **[13, 98, 99].**

More efforts also have been done by several authors to improve the value of *ME* coefficient in laminate composite (2-2) systems. Laminates composite are generally

synthesised by co-firing of ferrite and piezoelectric oxide layers. Various combinations of ferroelectric/piezoelectric oxides and ferrites have been reported by Srinivasan *et al*. including the PZT, BT, PT, BNT, PMN-PT piezoelectric layers are laminated with ferrite phases e.g., NFO, CFO and LSMO **[103-107].** Laminated ceramic composites exhibited higher value of *ME* voltage coefficients as compared to particulate composite. Another significant difference between the particulate and laminate ceramic composite is that the laminate composites exhibit the larger anisotropy energy as compared to particulate composite **[103, 104, 106, 108].** As in the particulate composites, the inter-diffusion between two components also occur in layered composites during the high temperature sintering process, which lead to deteriorate the properties of the composites **[107, 101].** In order to prevent the inter-diffusion and the unwanted secondary phases during sintering of the composites, the hot pressing technique has been employed **[101].** Srinivasan *et al*. employed a direct comparison of *ME* composites made by hot pressing and the conventional sintering process**[101].** The *ME* composite made by hot pressing exhibited more than one order higher value of *ME* coefficient **[101].**

The progress towards multiferroic nanocomposite thin films motivated by a pioneer work reported by Zheng *et al.* in 2004 **[35, 109].** To explore the thin film type multiferroic nanocomposites, keeping effective multiferroic properties for device base applications, various techniques were employed for preparation of thin films. Multiferroic nanocomposite thin films of ferroelectric (e.g., BFO, BTO, PZT, PTO) and ferrites (e.g., NFO, CFO, NZFO, CZFMO) prepared via chemical solution deposition, chemical vapour deposition, pulse laser deposition, RF sputtering e.t.c **[110-113].** Among the various deposition technique, the chemical solution deposition is a convenient and inexpensive deposition method to fabricate nanocomposite thin films. In comparison to bulk *ME* composites the nanocomposite thin films provide a more degree of freedom to modify the multiferroic behaviour. The coupling interaction between two phases in the nanocomposite thin films is still same as in the bulk composite structures **[111, 112].** However, good bonding between two phases in nanocomposite thin films has reduced interface losses because the interface between

the piezoelectric and piezomagnetic combined at the atomic level **[114, 115].** While, the laminate *ME* composites usually combined by adhesive bonding or co-sintering, resulted losses at the interface. From microstructural point of view multiferroic nanocomposites thin films also can be divided into three types. (i) Particulate nanocomposite films **(0-3 structure)**, generally a magnetic component is distributed in a ferroelectric matrix (ii)Horizontal structure **(2-2 structure)**, which is generally consisting of multilayer composites with alternating layer of ferroelectric and magnetic phases (iii) Vertical heterostructures **(1-3 nanostructures)**, where magnetic nanopilars are embedded in ferroelectric matrix.

In comparison to 0-3 type bulk ceramic composites, thin films based multiferroic composites have received the significant research interest due to unique ferroelectric and ferromagnetic properties and strong cross coupling between two order parameters. For example, Wan *et al.* **[27]** prepared polycrystalline composite thin films using the sol-gel method in which CFO particles dispersed randomly in PZT matrix. In the same manner Zhong *et al.* reported multiferroic thin films using $Bi_{3.15}Nd_{0.85}Ti_3O_{12}$ (BNTO) as the ferroelectric component and CFO as magnetic component to constitute *x*BNT/(1–*x*)CFO polycrystalline multiferroic films **[115]**. In both studies multiferroic composite thin films exhibit the ferroelectric, magnetic properties. *ME* voltage coefficients were also measured in both the composite thin films. Liu *et al* also developed a modified sol-gel process to preparation of PZT/CFO multuferroic composite thin films **[116].** Enhancement in ferroelectric and magnetic properties was observed keeping sufficiently *ME* coupling coefficient in composite thin films. The *ME* voltage coefficient in these composite samples was measured by applied external magnetic field induced electric polarization change. Recently Sone *et al*. reported BFO/CFO particulate nanocomposite thin films using chemical solution deposition route **[34]**. CFO nanoparticles (~10 nm) were uniformly dispersed in the BFO matrix. The ferroelectric switching of BFO/CFO nanocomposite films was similar as BFO thin films, although a larger electric field was needed to saturate the ferroelectric loops. The magnetic properties of BFO/CFO nanocomposite thin films were significantly improved by incorporation of CFO nanoparticles into BFO matrix. The saturated

magnetization and the coercive field were observed of 80emu/cm^3 and 450Oe respectively at 300 K.

Multilayer nanocomposite thin films consisting of alternating layer of ferroelectric and spinel ferrites usually exhibit weak *ME* behaviour due to clamping effect from the substrate **[117].** However the value of *ME* coefficients were comparable to that in bulk counterparts. The first work on *ME* composite thin films with (2-2) interconnectivity have been developed by Bichurin in 2003 using a sol-gel process and spin-coating technique **[118].** Zhang *et al.* reported a 2-2 multilayer nanocomposite thin films of BTO/CFO grown on STO substrate prepared by pulse laser deposition. Comparable to bulk *ME* composites the large value of *ME* coefficient around 66 mV/cmOe was observed **[119].** To overcome the problem of clamping effect in such multilayer nanocomposite thin films, He *et al.* tried to modify the interface using LNO as buffer layer in between the substrate and the composite film **[10].** This results in the different ferroelectric behaviour of the nanocomposite thin films as well as enhancement in the *ME* voltage coefficient. To explore the multiferroic properties in multilayer nanocomposite thin films, works have been reported by several authors. Li *et al.* developed a magnetic field dependent Raman scattering to study the strain mediated *ME* behaviour in multilayer nanocomposite thin films **[120].** In this study, the stress developed by magnetostriction of CFO layer transferred to the PZT layer causes in Raman mode changes in the nanocomposite thin films. Similar work on multilayered nanocomposite thin films has been conducted by many groups. For example, a multilayer epitaxial nanocomposite thin films have been reported by Ryu *et al.*, Ziese *et al.* and Ma *et al.* **[121-123].** To reduce the clamping effect and improve the multiferroic behaviour, the vertical hetrostructures of ferroelectric/piezoelectric and ferrites have been developed.

The work on vertical hetrostructures consisting of spinel phase embedded in a ferroelectric matrix reported by Zneng *et al.* **[35].** In this report nanocomposite thin films with 1-3/Vertically aligned structure grown on $SrTiO_3$ by pulse laser deposition in 2004 using the piezoelectric and ferrimagnetic phases of $BaTiO_3/CoFe_2O_4$ (BTO/CFO). The nanocomposite films grown with 1-3 type structure exhibit distinct

magnetoelectric coupling behavior. Basically the *ME* effect in (1-3) type composites is caused by the strain-induced charge at the interface between two phases. So it is essential to achieve a strong interfacial bonding at the interface between two phases in 1-3 types composites. There are several reports in literature to study the interface effect on the ferroelectric and magnetic properties as well as *ME* coefficient of vertical nanostructures **[111, 124].** In comparison to 2-2 type multiferroic thin films, 1-3 type was attributed to reduce the clamping effect demonstrating the substantial *ME* coupling in such nanocomposite thin films. Recently, multiferroic thin films have been prepared by F. Zavaliche *et al.* **[125]** and H. Zheng *et al.* **[126]** in 2011 having 1-3/vertically structure using the pulse laser deposition. In these reports the effect of interface between the substrate and the films have been studied.

2.4 Progress on BNT based multiferroic composites

Among, perovskite based piezoelectric oxides, PZT exhibits the highest value of piezoelectric coefficient. However, due to environmental concern the lead free piezoelectric materials are preferred. Therefore, we are motivated to search new high performance Pb free Bi-based perovskite oxides, while Bi^{3+} has a similar electronic configuration structure to Pb^{2+}. Among non lead based piezoelectric oxides, BNT is a perovskite piezoelectric oxide which was discovered by Smolenskii *et al.* in 1961 **[127].** But, researchers did not give much attention toward BNT based lead free piezoelectric systems until the initial dielectric and optical properties were reported by various groups in 1990s **[128, 129].** The better structural understanding of BNT provided by Jones and Thomas in 2002 that shows the rhombohedral *R3c* space group at room temperature and changes to tetragonal and subsequently cubic with increasing temperature **[130].** Also, the temperature dependent dielectric spectra of BNT samples reported by several author indicated two anomalies at 200 °C and 320 °C. The dielectric anomalies at 200 °C(T_d) and 320 °C ascribed to ferroelectric to antiferroelectric and and anti-ferroelectric to paraelectric phase transitions respectively **[37, 128, 130].** However, few reports in literature claim that the low temperature anomaly corresponds to T_d is not fully antiferroelectric, leaving this question unresolved **[37, 130, 131]**.

Moreover, BNT being a rhombohdral ferroelectric perovskite at room temperature, is reported to have superior ferroelectric properties with large remnant polarization ~38 μC/cm^2 and high Curie temperature ~ 603 K. It can be an excellent substitute for Pb based oxides **[37].** However, BNT in pure form has been reported an electrically hard material having coercive electric field (E_c ~ 73 kV/cm) which makes it difficult to pole electrically, resulting into a smaller piezoelectric coefficient (d_{33} ~ 80 pC/N) **[37, 38].** So in search of high performance piezoelectric oxides BNT based binary and ternary piezoelectric oxides have been reported by many groups **[37-40].**

BKT is an another ferroelectric material reported with perovskite structure at room temperature. BKT based perovskite oxides are expected with a high piezoelectric working temperature. There are few reports in literature on BKT based piezoelectric oxides. It is very difficult to prepare with dense ceramic body using conventional ceramic fabrication process and their poor electrical properties have been reported. To obtain a dense ceramic as well as to improve the electrical properties of BKT based perovskite oxides, attempts to sinter have been made using the hot pressing method. In addition, a small amount of BT also added to improve its electrical properties. For example, Bichurin *et al* reported study on synthesis, phase transition and piezoelectric properties on binary piezoelectric ceramics. This system exhibits the phase transition corresponding to orthorhombic, tetragonal and cubic phases. The excellent piezoelectric properties lies on boundary of orthorhombic and tetragonal phase in such binary systems.

It has also been reported that the solid solution of rhombohedral BNT and tetragonal perovskites like BKT, BT and KNN with morphotropic phase boundary (MPB) exhibit improved piezoelectric response **[37-40].** Takenaka *et al.* reported phase diagram of solid solution BNT-BT presenting the morphotropic phase boundary (MBP). In this report the piezoelectric coefficient was found to be 125 pC/N along with decreasing the curie temperature T_c and the depolarizing temperature T_d, also called ferroelectric to anti-ferroelectric transition temperature **[38].** In addition, there are some other reports in literature in which, BNT has been modified with other solid solutions of

$BaTiO_3$(BT), $(Bi_{0.5}K_{0.5})TiO_3$ (BKT), $(K_{0.5}Na_{0.5})NbO_3$ (KNN) and $Bi(Mg_{0.5}Ti_{0.5})O_3$ (BMgT) **[37-40].** However, comparable to PZT, the piezoelectric response and electric field strains were not achieved in such BNT based binary systems. The addition of small amount of third component, e.g., BMgT and KNN in such binary systems seems to improve its both piezoelectric and electric field induced strain behaviour. For the ternary system of BNT-BKT-KNN phase diagram and switching characteristics of morphotropic phase boundary has been studied **[39].** KNN addition induces the transition from tetragonal to pseudo cubic phase and a significant jump of the electric field induced strain was observed. More importantly, In this study the observed giant strain was related to the distortion induced by electric field from the pseudo cubic structure of ternary system **[87].** Zhang *et al.* also reported several papers on ternary piezoelectric oxides $(0.94-x)Bi_{0.5}Na_{0.5}TiO_3–0.06BaTiO_3–xK_{0.5}Na_{0.5}NbO_3$**[132-134].** The giant strain of 0.45% for particular composition x=0.02. with enhanced piezoelectric behaviour was observed. In 2008 Kounga *et al.* reported $(1-x)Bi_{0.5}Na_{0.5}TiO_3$-$xK_{0.5}Na_{0.5}NbO_3$ lead free piezoelectric oxide for $0 \leq x \leq 0.12$. At x~0.07 and found a morphotropic phase boundary (MPB) between a rhombohedral *FE* phase and a tetragonal AFE phase **[135].**

Jarupoom *et al* reported d_{33} value greater than 500pm/V in ternary 72.5BNT-22.5BKT-5BMgT based solid solution **[41].** Recently, Singh *et al.* (2013) reported BNT-KNN-LTS ternary piezoelectric having large electric induced strain ~ 40% for tetragonal composition. The value of piezoelectric coefficient and dielectric constant of around 169 pC/N and 3000 respectively was observed **[42].** Hence, BNT and modified BNT based piezoelectric oxides could be a potential candidate for lead free particulate *ME* composites. For example, a sintered BNT-NFO particulate composite has been reported by Babu *et al* consisting of random NFO particles are distributed in BNT matrix. The composite exhibits a *ME* response of 0.14% under 6kOe at 1MHz **[136].** Babu *et al.* also report the BNT/CFO particulate composite synthesized by solid state reaction method. A large converge *ME* coefficient of 109 Oe-cm Kv^{-1} was observed in this system **[136].** The results of *ME* response signifies that BNT is a potential ferroelectric phase could be effective alternative for lead free *ME* devices. The studies on BNT

based particulate composite are very scarce [50, 51]. However, no report is available in literature on the modified BNT based particulate composites. Table 2.1 summarises few important work reported in literature for two phase multiferroic composite systems prepared by different methods in various connectivity patterns.

Table 2.1 Few important work reported on two phase multiferroic composites.

Composition	Connectivity	Fabrication Method	~ P_r	~ M_s	α_E	Ref []
PZT-NFO	0-3	Solid-state route	-----	28 emu/g	80 (mV/cmOe)	[94]
PZT-LSMO	2-2	Tape casting	-----	-----	60 (mV/cmOe)	[103]
PZT-CFO	0-3	Sol-gel	-----	-----	115 (mV/cmOe)	[93]
PZT-CFO	0-3	Sol-gel	8 µC/cm^2	120 emu/cm^3	-----	[116]
PZT-CZFMO	0-3	Solid-state route	-----	60 emu/g	60 (mV/cmOe)	[44]
PZT-CZFMO	0-3	Solid-state route	-----	16 emu/g	0.3 (mV/cmOe)	[99]
BFO-CFO	1-3	PLD	60 µC/cm^2	205 emu/cm^3	-----	[31]
BFO-CFO	1-3	PLD	86 µC/cm^2	400 emu/cm^3	-----	[32]
BFO-CFO	0-3	Sol-gel	40 µC/cm^2	80 emu/cm^3	-----	[34]
BFO-NFO	0-3	Sol-gel	3 µC/cm^2	80 emu/cm^3	-----	[7]
BFO-CFO	1-3 type	PLD	60 µC/cm^2	---	-----	[48]
BFO-NFO	1-3 type	PLD	------	50 emu/cm^3	-----	[48]
BFO-CFO	1-3	PLD	-----	-----	-----	[114]
BFO-CFO	2-2 type	rf sputtering	73 µC/cm^2	140 emu/cm^3	-----	[8]
BFO-CFO	2-2 type	rf sputtering	72.1 µC/cm^2	61.2 emu/cm^3	-----	[111]
BT-CZFMO	0-3	Solid-state route	-----	28 emu/g	60 (mV/cmOe)	[45]
BNT-CFO	0-3	Sol-gel	10 µC/cm^2	200 emu/cm^3	-----	[115]
BNT-NFO	0-3	Sol-gel	-----	40 emu/g	-----	[50]
BNT-CFO	0-3	Sol-gel	8 µC/cm^2	16 emu/g	2000mV/cm	[51]
BNT-CFO	0-3	Sol-gel	-----	35 emu/g	-----	[136]
CoFe2O4-$SrBaNb_2O_6$	0-3	Solid-state route	-----	-----	23 (mV/cmOe)	[96]
BT-CFO	0-3	Sol-gel	-----	-----	252 (mV/cmOe)	[97]

CHAPTER III
EXPERIMENTAL AND CHARATERIZATION TECHNIQUE

Overview

This chapter give details the processing methods employed for synthesizing the samples of different compositions. A brief details of the various characterization techniques used to study structural, microstructural, dielectric, ferroelectric, magnetic and magnetoelectric properties are provided.

The chapter is divided into two sections. The first section of the chapter details of the experimental procedure adopted for synthesis of samples and the second section will contain a brief description of the characterizations in the present work.

3.1 Sample preparation:

In the present work following series are synthesized by sol-gel method:

1. Pure BFO thin films
2. (1-*x*)BFO-*x*CFO (*x*=0, 0.1, 0.2, 0.3) nanocomposite thin films.
3. (1-*x*)BFO-*x*(NFO) (*x*=0, 0.1, 0.2, 0.3) nanocomposite thin films.
4. (1-*x*)[BNT-BKT-BMgT] - *x*(NFO) (*x*=0, 0.1, 0.2, 0.3) particulate composites.
5. (1-*x*)[BNT-BKT-BMgT] - *x*(CFO) (*x*=0, 0.1, 0.2, 0.3) composites

3.1.1 Synthesis of BFO-CFO and BFO-NFO nanocomposite thin films

A 0.2M BFO precursor solution was prepared by dissolving bismuth nitrate pentahydrate $Bi(NO_3)_3.5H_2O$ and iron nitrate nonahydrate $Fe(NO_3)_3.9H_2O$ with the molar ratio of 1:1 into 2-methoxyethanol and 10 mol % excess bismuth nitrate was used to compensate for the volatile Bi loss during annealing process. To prepare the 0.2M CFO and NFO precursor solution, cobalt nitrate hexahydrate ($Co(NO_3)_2.6H_2O$), nickel nitrate ($Ni(NO_3)_2.6H_2O$) and iron nitrate nonahydrate ($Fe(NO_3)_3.9H_2O$) were dissolved in 2-methoxyethanol with molar ratio of 1:2. Both precursor solutions of BFO and CFO, NFO were mixed together with volume ratio of BFO/CFO, NFO (x = 0, 0.1, 0.2, 0, 0.3) using Hamilton microliter microsyringe, heated and stirred continuously at 70 °C for 1 hours to get a well mixed BFO/CFO and BFO/NFO gel solution. The mixed solution was spin coated onto indium tin oxide coated (ITO) glass substrate at 3000 rpm for 40 sec. and subsequently baked at 300 °C for 5 min. Finally, the thin films were obtained by repeating this spin-coating-baking-annealing process twice followed by annealing at different temperatures like 600 °C and 650°C for 30 min in ambient atmosphere. Fig. 3.1 shows the flow diagram of preparation of composites.

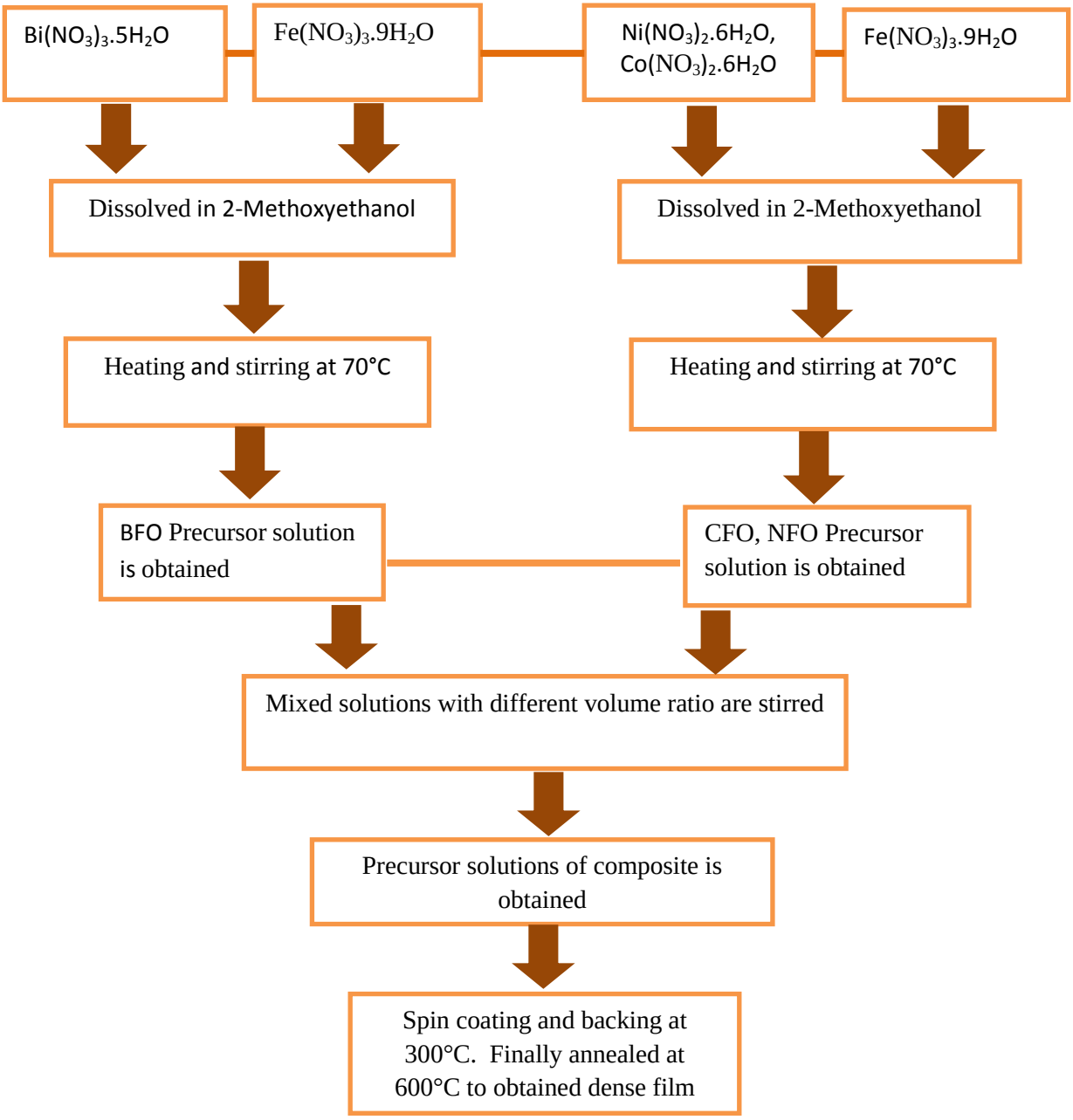

Fig. 3.1 Flow chart of the synthesis of composites.

3.1.2 Synthesis of BNT-BKT-BMgT-NFO and BNT-BKT-BMgT-CFO composites

High purity bismuth nitrate [$Bi(NO_3)_3.5H_2O$], sodium carbonate Na_2CO_3, titanium isoproxide $TiC_{12}H_{28}O_4$, magnesium nitrate $Mg(NO_3)_2{\cdot}6H_2O$, potassium nitrate KNO_3, citric acid $C_6H_8O_7$, and acetyl-acetone $C_5H_8O_2$ of Sigma Aldrich (99.99%) were used for synthesis. In the first step, 72.5BNT–22.5BKT–5BMgT powder was prepared by dissolving all precursors into 2-methoxyethanol and 10 mol % excess bismuth nitrate was used to compensate for the volatile Bi loss during annealing process. The solution of 72.5BNT–22.5BKT–5BMgT stirred and heated at 70 °C until powder is formed. The obtained powder is calcined at 700 °C. To prepare the CFO powder, cobalt nitrate hexahydrate ($Co(NO_3)_2.6H_2O$) and iron nitrate nonahydrate ($Fe(NO_3)_3.9H_2O$) were dissolved in 2-methoxyethanol with molar ratio of 1:2. The solution of CFO heated at 200°C in oven until powder is formed. The CFO powder was also calcined at 600°C. In the next step, (1-*x*)[72.5BNT-22.5BKT-5BMgT]-*x*(NFO, CFO) composite series were prepared, where, *x* = 0, 0.1, 0.2, 0.3). The powders of BNT–BKT–BMgT, and CFO, NFO were thoroughly mixed in desired weight ratio and pressed into cylindrical pellets of 10 mm diameter at a pressure of 12.5 MPa. The pellets were sintered at 900 °C for 4h in ambient atmosphere. Principle and flow diagram of preparation samples using sol-gel method are shown in fig.3.2 and fig. 3.3 respectively.

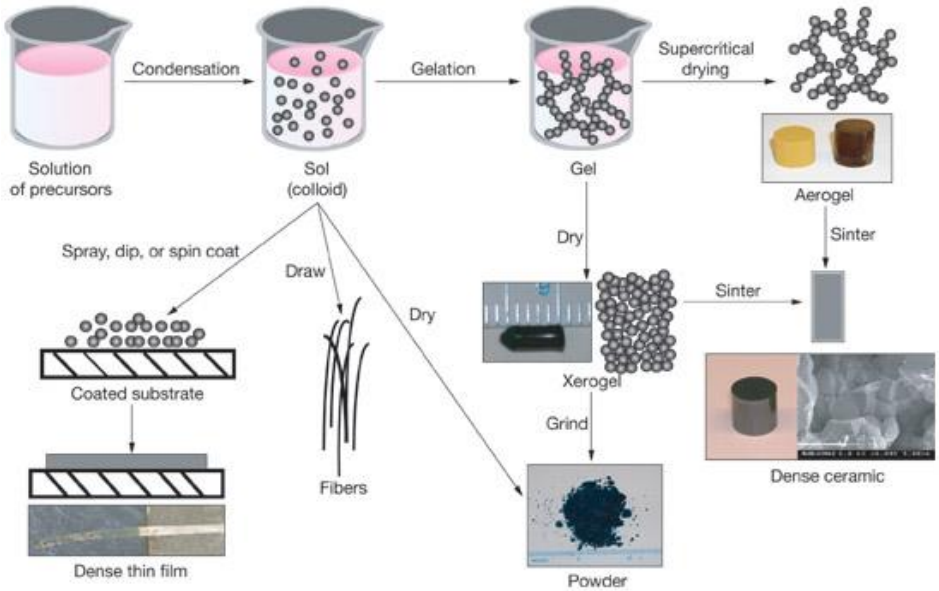

Fig. 3.2 Principle of preparation of bulk pellets and thin films using sol-gel method.

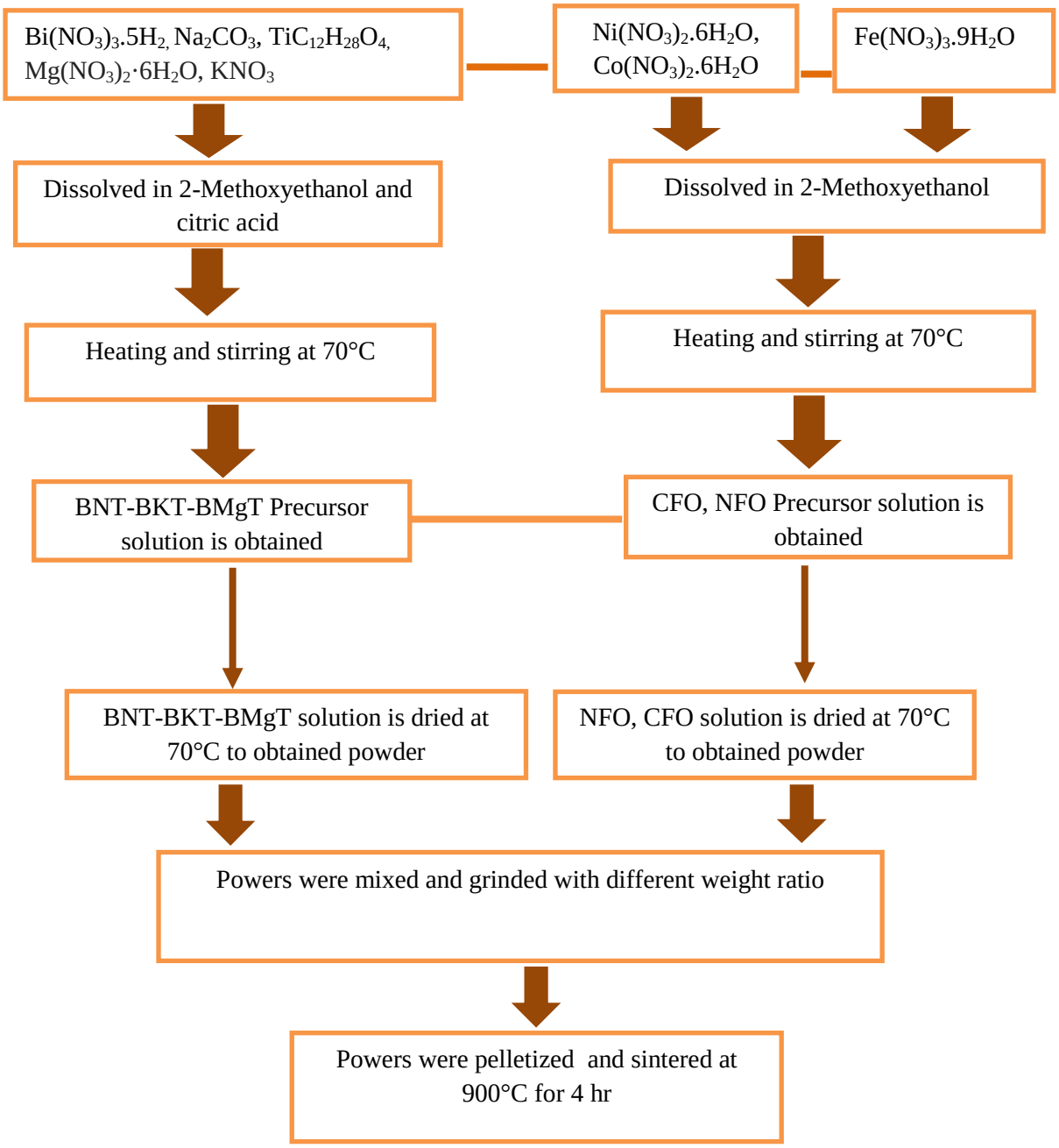

Fig. 3.3 Flow chart of the synthesis of multiferroic composites.

3.2 Characterization Techniques

This section briefly describe the various characterization techniques used to study the different properties of the samples.

3.2.1 X-ray Diffraction

XRD is the characterization technique used for structural and phase analysis of materials. The Philips X'pert PRO X-ray diffractometer with Cu Kα radiations having a wavelength of 1.5418 Å was used to irradiate the samples. The intensity of diffraction peaks in the XRD pattern were recorded as a function of diffraction angle 2θ and indexed with different crystal planes. The X-ray "reflections" took place only at certain angles in the crystal structure that were controlled by the inter-planar spacing and the wavelength of the X-rays. The X-ray reflections follow the Bragg's equation

$$\mathbf{2d \sin\theta = n\lambda}$$

where n is the order of the reflection (basically first order is observed in XRD), λ is the wavelength X-ray source, d is the inter-planar spacing and θ is the incident angle relative to the plane of atoms. Additionally, XRD can be used to address the following issues:

- Identification of the crystalline phases including lattice parameters and crystal structure.
- Detection of unknown phases in materials.
- Identification of the preferred orientation of polycrystals and crystalline texture.
- To measure the certain physical characteristics, such as, strain and stresses in thin films.

3.2.2 Scanning Electron Microscopy (SEM)

The microstructural study of the sample was carried out using scanning electron microscope (SEM) (JEOL JSEM 6510VL). A scanning electron microscopy was used to measure the surface morphology and grain size of the samples. A finely focused electron beam was used to irradiate the samples to producing the images. The various

information including grains distribution and inter-granular pores in bulk as well as thin films are observed. The signals release in SEM from the specimen include secondary electrons, characteristic x-rays, backscattered electrons, auger electrons, and many other radiations. Usually, the secondary electron detectors are standard to collect and form the SEM image. To avoid the charging of electrons a thin layer of conducting gold was deposited before measurements using sputtering technique.

3.2.3 Transmission Electron Microscopy (TEM)

The TEM analysis of nanocomposite thin films was done by transmission electron microscopy (TEM TECNAI G2 20 S-TWIN). The standard ion beam milling procedure was adopted to prepare TEM sample. Transmission electron microscopy is a versatile technique capable of collecting information in wide range of magnification. TEM operates on the same basic principle like light microscope but in TEM we use electrons instead of light. Much lower range of wavelength of electrons used in TEM makes it capable to get a thousand times higher resolution. The selected area electron diffraction pattern (SAED) can be used to determination of the crystal structure at different parts of the sample.

3.2.4 Atomic force microscopy (AFM)

Atomic force microscopy (AFM) model (NT-MDT SOLVER NEXT) was used to see the surface morphology and roughness of the films. AFM uses a fine tip to measure surface morphology and properties through an interaction between the tip and surface. In an AFM a constant force is maintained between the probe and sample while the probe is raster scanned (parallel lines) across the surface. By monitoring the motion of the probe as it is scanned across the surface, a two as well as three dimensional image of the surface is constructed.

3.2.5 Electrical Measurements

For electrical measurements of pellets, the sintered ceramic pellets were ground and polished using different graded polishing paper. These polished samples were ultrasonically cleaned to remove any kind of polishing material left on the sample. Then silver electrodes were deposited on parallel phases of the sample followed by

fired at 150 ^{o}C for 20 mins. For electrical measurements of thin films , the Au dots of 0.8 mm were deposited using the mask on the film by sputtering technique.

Dielectric measurements

Dielectric measurements of the samples were performed using the impedance analyzer model HP4192A interfaced to a temperature controller furnace connected to PC, measurement cable (16048 A test leads), sample holder and software. The dielectric constant and dielectric losses of the samples were measured as a function of temperature and frequencies. The computer interface temperature controller furnace (from room temperature to 873 K) was used to measure the temperature variation of the samples.

The dielectric constant (ε_r') of the samples was calculate using the following relation.

$$\varepsilon_r' = \frac{C.t}{\varepsilon_0.A}$$

where t is thickness, A is the area of the electrode on the sample and ε_0 is the permittivity (8.85×10^{-12} F/m) of free space in the above relation.

Ferroelectric measurements and magnetic measurements

Polarization (*P-E*) electric field hysteresis loops for all samples were performed at room temperature using the ferroelectric tester (Radiant technologies Precision Premier II). The ferroelectric measurement set up includes a main ferroelectric tester, power supply up to 10 kV, high voltage interface, sample holder and a software. To perform the measurements specially on bulk pellet samples the spring loaded sample holder is used to hold the samples. There is a facility in a measurement set up to measure the *P-E* loops at different frequencies (0.1 Hz to 1 kHz). Facility of averaging and cycling of the data points using the softwareis also available in the system. We can calculate all the parameters e.g. P_{max}, P_r and E_c using the recorded *P-E* loops from the system. A SQUID (superconducting quantum interference device) (MPMS XL-7, Quantum design) magnetometer is a very sensitive powerful tool was used for various magnetic measurements of the sample.

3.2.6 Magntoelectric (*ME*) coupling measurements

α_E was measured and calculated using a Lock–in–amplifier technique. The sample were polled in the field of 4 kV/cm at T = 70ºC prior to the *ME* measurements. The d_{33} of all the samples were measured using the YE2730A d_{33} meter from APC Int. Ltd. Magnetoelectric coupling is an essential property for all *ME* multiferroics. The estimation of *ME* coupling was performed by measuring effect of a magnetic field on ferroelectric polarization or, conversely, that of an electric field on magnetic order. Before making the magnetoelectric voltage coefficient measurements, sample is first electrically poled. For electrical poling the sample are heated above its ferroelectric Curie temperature, kept at this temperature in the presence of high electric field and then slowly cooled down to room temperature in the presence this field. Electric poling is essential to align the ferroelectric domain in one direction and make the sample piezoelectrically active. The schematic diagram for ME measurements are shown in fig.3.4.

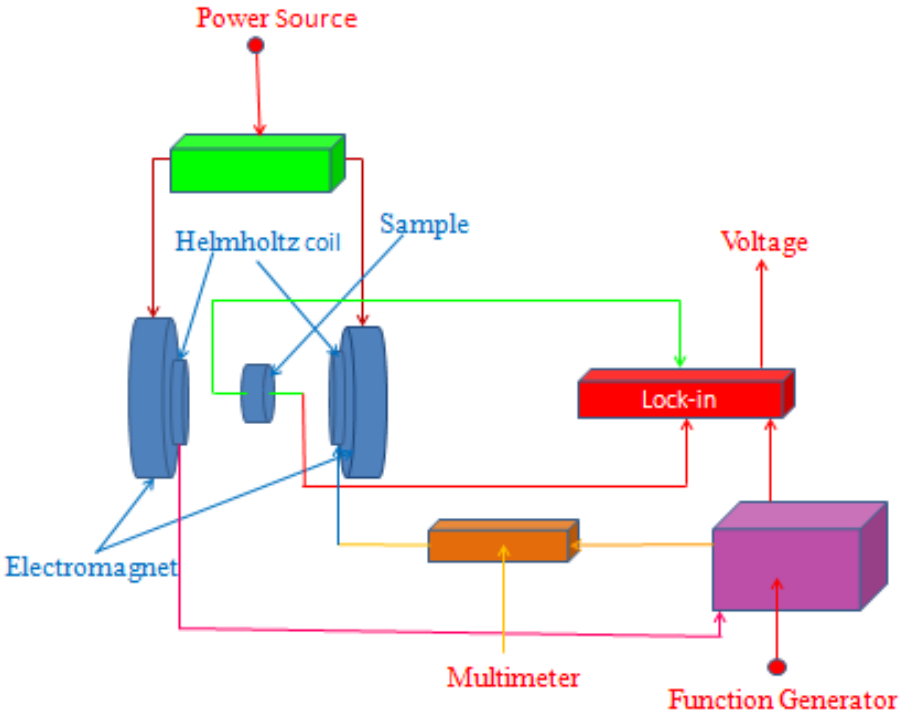

Fig. 3.4. Block diagram for *ME* coupling measurement using Lock-In amplifier technique.

There are two methods for measure the *ME* voltage coefficient (i) static method (ii) dynamic method. We used dynamic method to measure the *ME* coupling of the samples in which induced output voltage is measured in the presence of weak *ac* magnetic field superimposed over strong *dc* magnetic field. There are generally two methods of measuring this output voltage in case of dynamic method (i) direct measurement of output voltage using the lock-in amplifier (ii) measuring the charge (*Q*) using charge amplifier then finding the voltage using relation ($V=CQ$) with measured value of capacitance across the sample. In both the cases induced output voltage (V_{out}) is measured in the direction of electrical poling by applying DC magnetic field under a constant AC magnetic field (H_{AC}) of amplitude ~1 Oe and frequency ~1 kHz. The schematic illustration of particulate composite representing the experimental conditions are shown in fig. 3.5. The value of α_E was calculated using the following relation:

$$\alpha_{E=}\frac{V_{out}}{tH_{ac}}$$

where, '*t*' is the thickness of the sample.

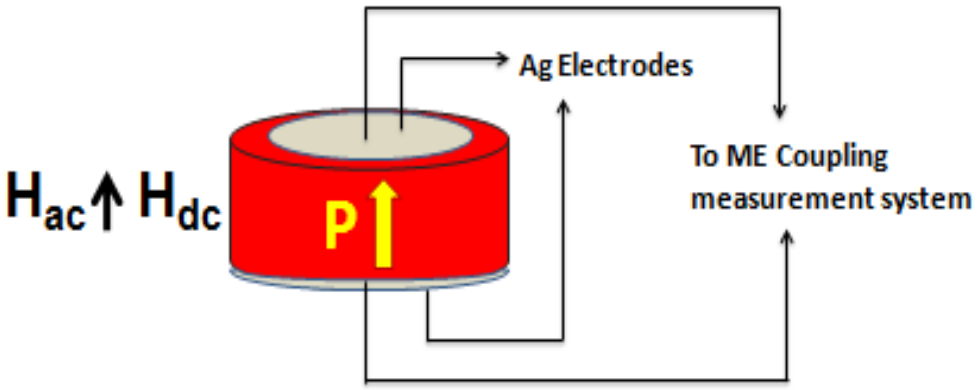

Fig. 3.5. Schematic illustration of particulate composite representing the experimental conditions.

CHAPTER IV
RESULTS AND DISCUSSION

Overview

In this chapter, obtained results of BFO and their composites samples are presented and discussed. This chapter is divided in two sections. In the first section, results of BFO based composites and in second section modified BNT based composites are discussed. Firstly, BFO thin films were synthesized by the sol-gel spin-coating technique at different annealing temperature. The effect of annealing temperature on structural, dielectric and ferroelectric properties has been investigated. Secondly, $BiFeO_3$-AFe_2O_4 (A=Co, Ni) composites have been developed and the effect of addition of ferrites in BFO matrix has been studied on their structural, dielectric, magnetic and ferroelectric properties. In the second section, sol-gel assisted BNT-BKT-BMgT-AFe_2O_4 (A=Co, Ni) particulate magnetoelectric composites have been prepared. The effect of addition of ferrites on their structural, dielectric, ferroelectric, magnetic and magnetoelectric properties has been studied systematically.

4.1 Study on $BiFeO_3$ thin films

Single phase, BFO thin films materials have attracted wide attention due to their potential applications in non-volatile memory devices **[1-3, 137, 138].** Among all single phase multiferroics materials, BFO in thin film form is extensively studied due to room temperature *ME* coupling. **[139-143].** Additionally, its optical band gap in visible range makes them suitable for such applications in photovoltaic cells and novel optoelectronic devices **[144, 145-155].**

4.1.1 XRD analysis

Fig. 4.1 shows the X-ray diffraction (XRD) patterns (a) for as-deposited BFO and annealed films at (b) 450 ºC, (c) 500 ºC, (d) 550 ºC, and (e) 600 ºC for 1 h. No crystalline phase are observed for as deposited film.

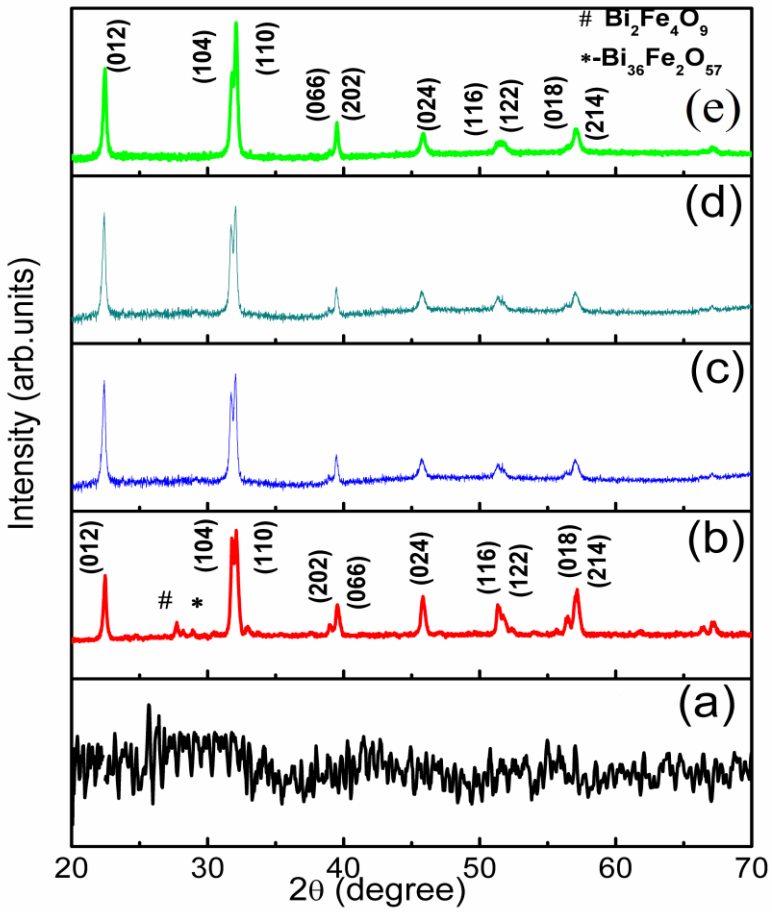

Fig. 4.1. XRD pattern of BFO thin films (a) as deposited (b) 450 ºC (c) 500 ºC (d)550 ºC and 600 ºC.

Films annealed at 450 ºC shows the peaks of the distorted rhombohedral perovskite-type structure with a space group *R3c* which agrees with the respective inorganic Crystal Structure Data Base Nº. 57424 **[156-160].** The peaks of BFO started to appear at 450 ºC however few impurity peaks of $Bi_{25}FeO_{40}$ and $Bi_{46}Fe_2O_{70}$ phase are also observed. The impurity phases completely disappeared as the temperature increases to 500 ºC and single phase BFO thin films were obtained. It is clear from the fig.4.1 that as the annealing temperature increases, intensity of the peaks increases, which shows that the crystallization increases with the temperature. The average grain size increases with increasing the annealing temperature and found to be 52 nm and 83 nm for the films annealed at 500 ^{o}C and 600 ^{o}C respectively.

4.1.2 SEM studies

Fig.4.2 (a, b) illustrate the FE-SEM images of BFO thin films annealed at 500^{o}C and 600 ^{o}C respectively. BFO thin film annealed at 500 ^{o}C indicates equiaxed grains with uniform size distribution; however, few pores are also observed in the films (white circle in Fig.4.2 (a). The film annealed at 600 ^{o}C shows inhomogeneous grain growth with the formation of irregular shape grains. The results are consistent with the previously reported results for BFO thin films **[154, 155].** The average grain size of the films annealed at 500 °C to 600 °C are ~ 62 nm and ~ 90 nm respectively. The smaller grain size values, as calculated from XRD, is due to the peak broadening from structural defects and stress in the thin films **[154].** Fig.4.2(c) shows the cross-sectional image of BFO thin film, the thickness of the film is determined to be ~ 200nm.

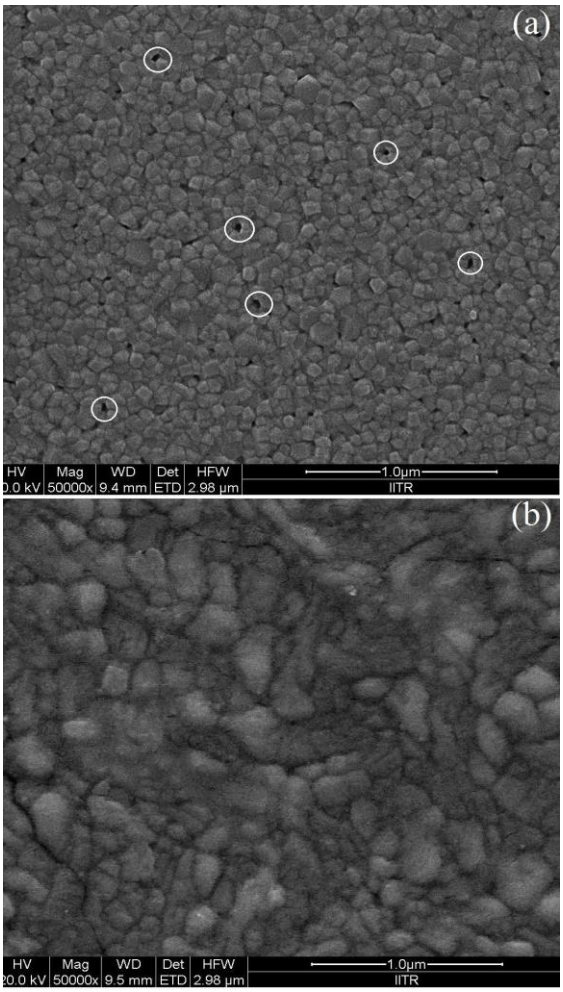

Fig. 4.2. FE-SEM images of BFO thin films annealed at (a) 500 ^{o}C, (b) 600 ^{o}C.

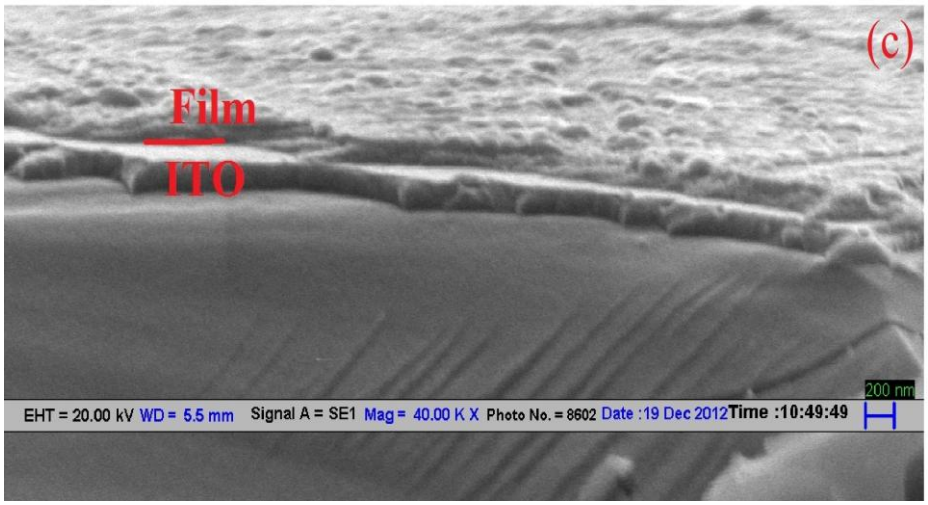

Fig. 4.2. (c) the cross section SEM micrograph of BFO thin film.

4.1.3 AFM analysis

Fig. 4.3 (a-c) illustrate the two dimensional AFM image of BFO thin films annealed at 500 ^{o}C, 550^{o}C and 600 ^{o}C respectively.The micrographs suggest the films are dense and well crystalline.

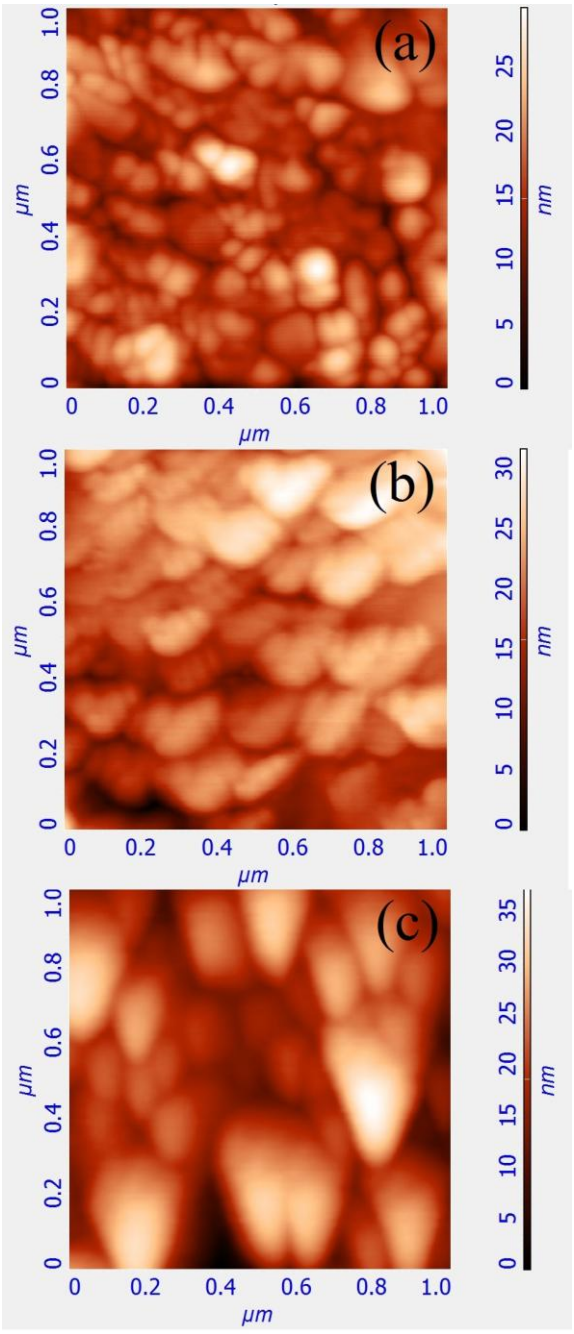

Fig. 4.3. AFM images of BFO thin films at annealing at (a) 500 ^{o}C, (b) 550 ^{o}C and (c) 600 ^{o}C.

It is evident that high annealing temperature, effect the surface morphology of the films. The smaller grain coalesce to form bigger elongated grains. Small grain size and the lower roughness value are observed for the films annealed at low temperature. The root mean square roughness (*Rq*) values are measured using the 10 μm x 10 μm area for better statics and found to increase with temperature. The *Rq* values are ~ 5.32nm and ~9.63nm for the films annealed at 500 ^{o}C and 600 ^{o}C respectively. The increase in *Rq* values with innealing temperature is mainly atributed to the increse in grain size **[154].**

4.1.4 Dielectric properties

Fig.4.4 (a) and (b) shows the *RT* frequency dependent dielectric constant (ε′) and dielectric loss (tan δ) of BFO films in the frequency range of 100 Hz to 10 kHz. There are many factors which can affect the dielectric behaviour of the ferrite materials such as grain size, cation distribution, porosity, crystal defects and sintering method etc. It is found from Fig. 4.4 (a) that increasing the frequency, the value of the ε' decreases slowly up to 10 kHz. The ε′ increases with increasing annealing temperature and found 181, 198 and 209 (at100Hz) for films annealed at 500 ^{o}C, 550 ^{o}C, 600 ^{o}C respectively. The grain growth, improved crystallinity and higher density of the films as observed by XRD patterns, FE-SEM and AFM images may be the reason for increased ε′. The results are comparable with BFO thin films prepared by different technique **[161-163].**

As shown in Fig.4.4 (b), a lower tan δ are observed in the films annealed at higher temperature. Slight increases in tan δ are also observed in the high frequency region (10^5-10^6 Hz). Such frequency dependent ε′ and tan δ behaviour of BFO thin films is expected, by considering the space charges, interface and dielectric relaxation in ferroelectric thin films. Fig.4.5 shows the temperature dependence ε′ behaviour of BFO thin films annealed at 500 °C. The measurement were carried out in frequency and temperature range of 1 kHz ≤ f ≤ 500 kHz, and 20 °C ≤ T≤ 300 °C respectively. It can be seen that ε′ increases with the increasing temperature and then decreases above ~ 270 °C. As the temperature increases, more charge carriers get excitation from their trapping centres and contribute to the polarization which in turn increases the ε′ of the films. In

general, interfacial, ionic and electronic polarization plays a dominant role in determining the dielectric properties of nanoferrite materials.

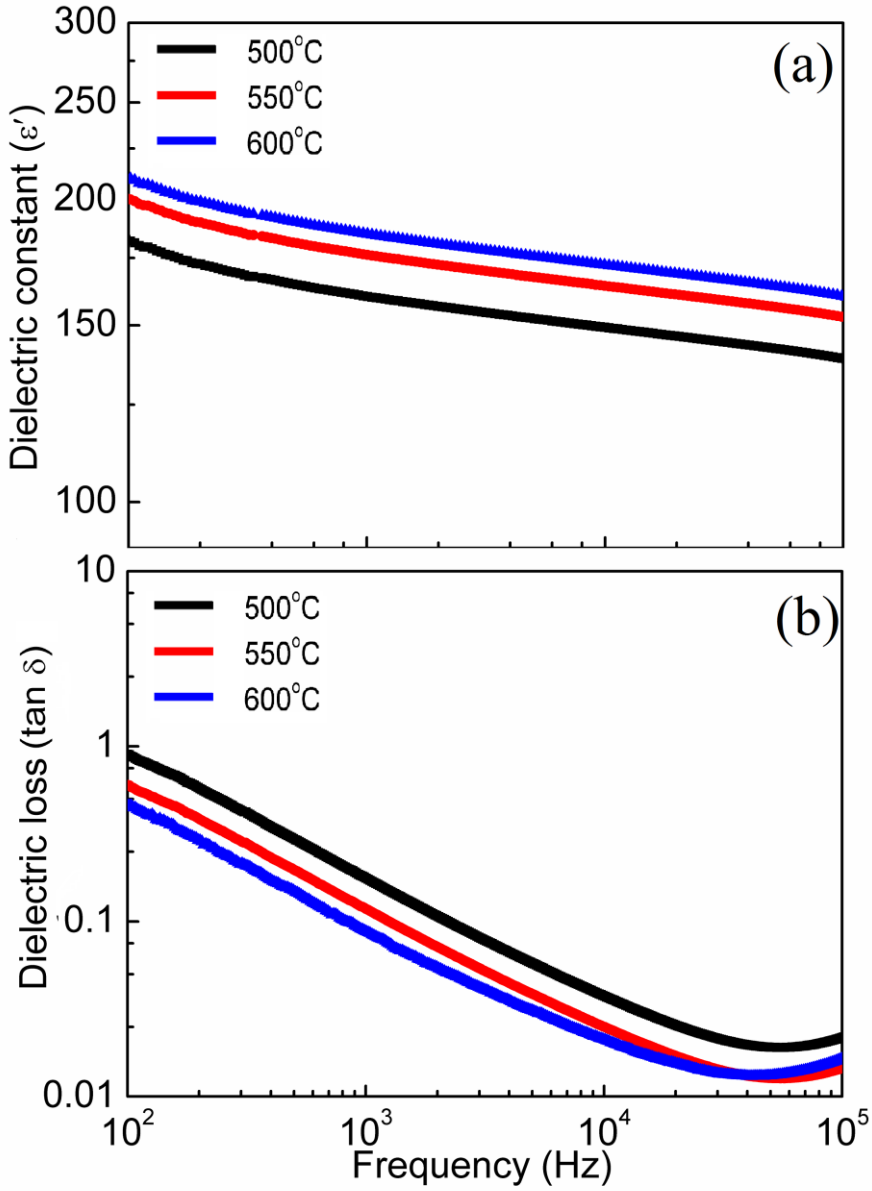

Fig. 4.4. The frequency dependent (a) ε′ and (b) tan δ of BFO thin films annealed at different temperature.

There is a finite contribution from surface polarization at low frequency which are strongly temperature dependent. Therefore, the higher rate of increase in ε′ at 100 Hz is due to the contribution from surface polarization which diminishes at higher

frequencies. The anomaly in ε′ around T_N signifies the antiferromagnetic phase of BFO is coupled to the electric polarization which is essential for a multiferroic system **[131].**

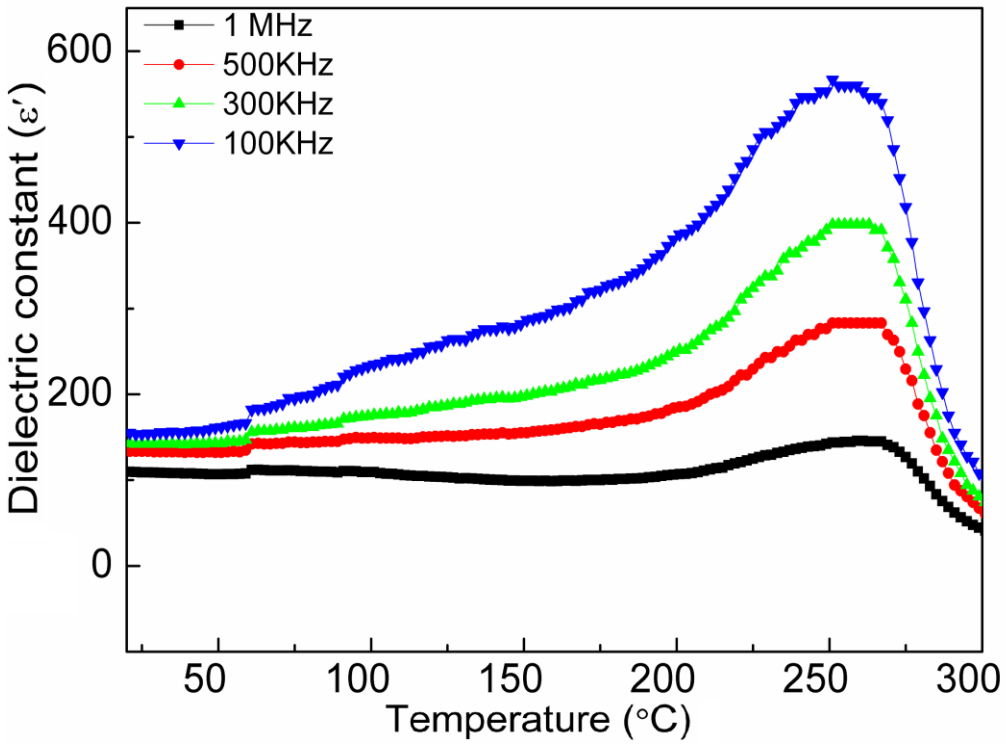

Fig. 4.5. Temperature dependent ε′ of BFO thin films annealed at 500 ^{o}C with different frequencies.

4.1.5 Ferroelectric properties

Fig.4.6 shows the *RT* ferroelectric (*P-E*) hysteresis loops of BFO thin films annealed at different temperature. The films annealed at 500 °C shows well saturated *P-E* loop, however, increasing annealing temperature from 500 ^{o}C to 600 ^{o}C, the $2P_r$ value decreased from ~51 μC/cm^2 to ~ 40 μC/cm^2 respectively. There are several factors contribute to the variation in ferroelectric properties including the Bi volatility, the nucleation and grain growth etc. of the BFO phase. The higher annealing temperature promotes nucleation and grain growth of the films which reportedly improves the ferroelectric properties **[163, 164, 165].** However in the present case, the decreasing trend of ferroelectric properties may be dominated by volatility of Bi at higher annealing

temperature which may lead to the formation of vacancy defects and degrades the ferroelectric properties of BFO thin films.

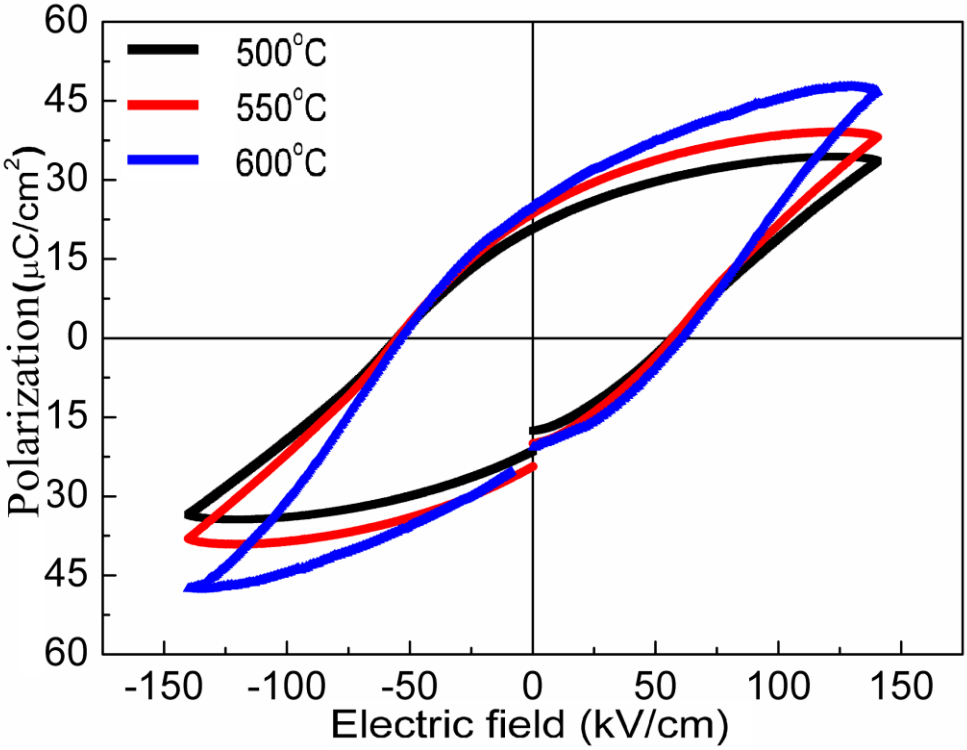

Fig. 4.6. *P-E* loops of BFO thin films annealed at (a) 500 ^{o}C, (b) 550 ^{o}C and (c) 600 ^{o}C.

4.2 $BiFeO_3$-$CoFe_2O_4$ composite thin films annealed at 600 ºC

Despite the problem of weak magnetic behaviour in single phase materials at room temperature, multiferroic composite thin films combining a ferroelectric and magnetic order have been developed **[1-3, 166].** As discussed in previous section BFO is a well known single phase multiferroic material exhibits good ferroelectric properties **[26, 27].** However, the weak magnetic behavior because of its G-type antiferromagnetic structure with nearest neighbor spins canting limits its multifunctional applications **[29].** Therefore, a composite structure have been developed to improve the magnetic properties of BFO by combining with $CoFe_2O_4$ (CFO) **[172].**

4.2.1 XRD analysis

Fig.4.7 shows the glancing angle XRD (GIXD) patterns of $(1-x)BFO-x(CFO)$ with (x= 0, 0.1, 0.2, 0.3) nanocomposite thin films at room temperature. XRD patterns of BFO and BFO/CFO nanocomposite thin films indicate the polycrystalline nature of the samples. Pure BFO thin films crystallize into a perovskite type structure with a space group *R3c* without the formation of any other impurity phases. However, XRD patterns of BFO/CFO establish the presence of two evident sets of well defined peaks indexed to the BFO phase and CFO phase. Furthermore, due to the low volume ratio of CFO as compared to BFO, the CFO grains were trapped around the ferroelectric grains of BFO phase, and its growth was found to be restrained. As a result of which no prominent diffraction peaks rather than (311) for spinel CFO was seen in the XRD spectrum for all composite thin films.

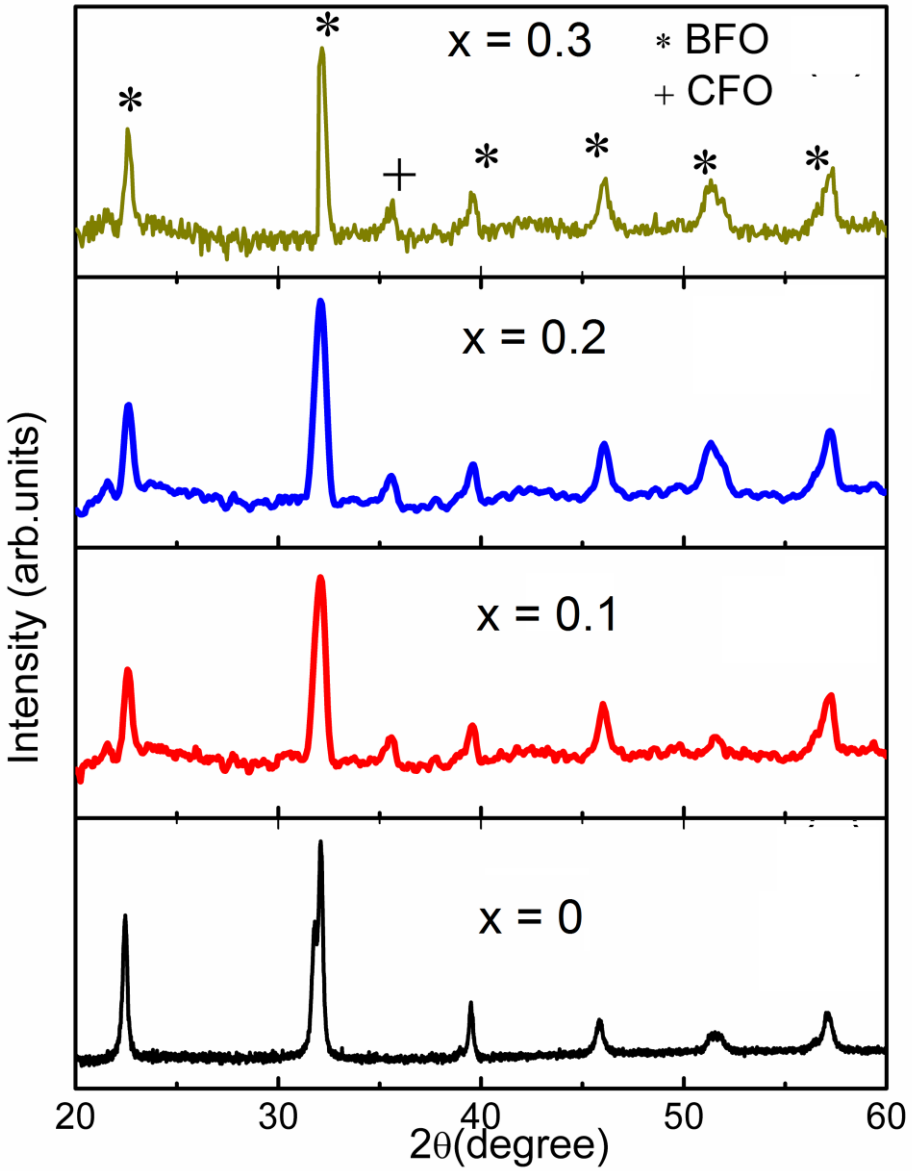

Fig. 4.7. X-ray diffraction pattern of $(1-x)$BFO-x(NFO) with (x = 0, 0.1, 0.2, 0.3)

4.2.2 FE-SEM analysis

The surface morphology (FE-SEM) of the pure BFO and BFO/CFO nanocomposite thin films are displays in fig.4.8 (a) and (c) respectively. Magnified view of BFO and BFO/CFO thin films are shown in fig. 4.8 (b) and (d) respectively.

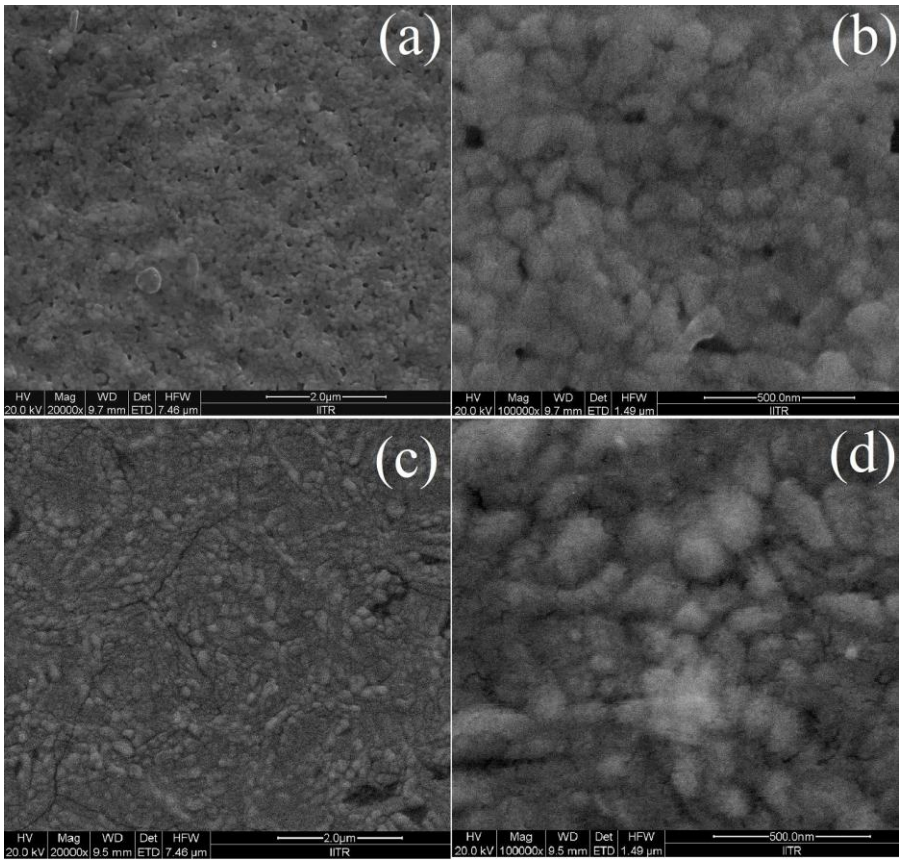

Fig. 4.8. The surface morphology of (a) BFO and (c) BFO/CFO thin films. The magnified view of (b) BFO and (d) BFO/CFO thin films.

It is clear from the micrograph that the BFO and BFO/CFO nanocomposite thin films consist of a fine and dense grain structure. The appearance of developed surface morphology of BFO/CFO nanocomposite thin films as shown in fig. 4.8 (c), consistent with that of surface morphology observed for BFO/CFO nanocomposite thin films in literature **[170-173].** Due to deeply buried CFO particles in the BFO matrix, the BFO and CFO particles could not be separated in FE-SEM image of BFO/CFO nanostructure.

Fig.4.9 (a) shows cross sectional SEM image of BFO/CFO film deposited on ITO coated glass substrate. The cross-sectional SEM image reveal clear boundary between BFO/CFO film and ITO coating. The thickness of the composite film and ITO coating was 170 nm and 150 nm respectively. The EDX spectra acquired from the BFO/CFO composite thin film sample are shown in Fig.4.9 (b) It can be seen clearly from the

fig.4.9 (b) the presence of constituent elements like Bi, Fe, Co and O originating from BFO/CFO. The EDX analysis of all composite samples also confirmed volume of the individual components.

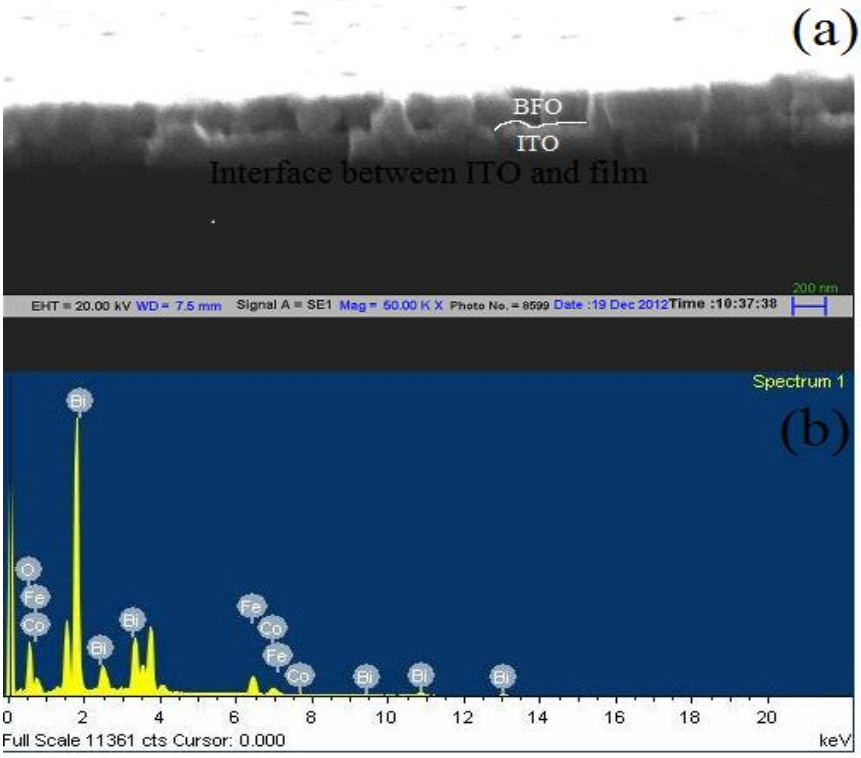

Fig. 4.9. (a) Cross section SEM micrographs (b) energy dispersive X-ray spectra of the BFO/CFO nanocomposite thin film.

4.2.3 TEM analysis

Fig.4.10 shows the plane view TEM image of BFO/CFO(0.7/0.3) nanocomposite thin film annealed at 600 ºC and the corresponding selected area electron diffraction pattern (SAED). Fig. 4.10(a) clearly depicts that CFO having lighter Co atoms appear dark, is embedded in BFO matrix appear bright containing heavier atoms, which indicates nanoscale mixing of the BFO and CFO phases. The diffraction spots of both BFO and CFO were also observed in SAXD of the BFO/CFO nanocomposite thin film structure indicating the distribution of BFO and CFO particles in the area. The calculated d_{hkl}

values as per the respective diffraction ring shown in fig.4.10 (b) for BFO and CFO are found to be d_{110} = 0.278 nm, an d_{311} = 0.252 nm respectively.

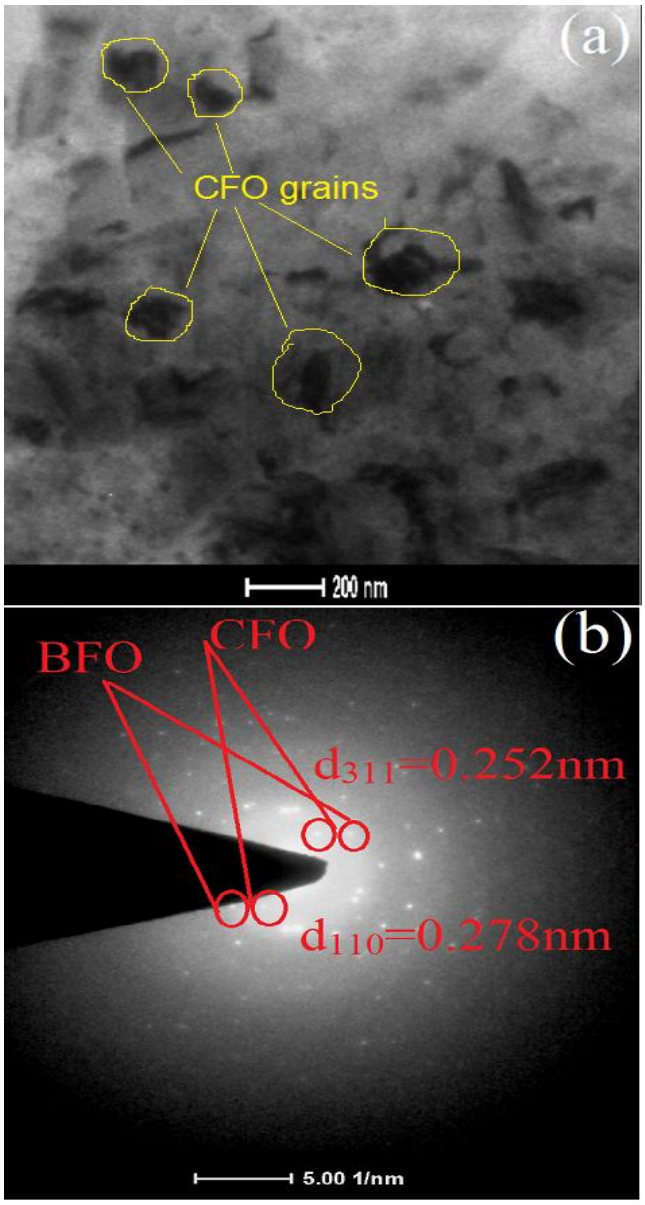

Fig. 4.10. The TEM micrographs of the surface morphology (a) and (b) selected area electron diffraction pattern of BFO/CFO composite thin films.

4.2.4 Raman analysis

The strain analysis of BFO/CFO nanocomposite thin film was studied by Raman spectroscopy. Recently, it has shown a versatile probe for investigating the structural

properties of thin films in literature **[174-177].** Fig.4.11 (a) presents the measured Raman spectra for pure BFO, CFO and Raman signature taken from the BFO/CFO nanocomposite thin films. Firstly, the Raman spectra for BFO and CFO were studied. In BFO which is a rhombohedrally distorted perovskite with space group *R3c*, it has been reported that its phonon modes which are Raman active with A_1 and E symmetry can be summarized using the following irreducible representation $\Gamma = 4A_1 + 9E$ [24]. There are several normal modes shown in fig. 4.11 (a) for the data obtained for BFO thin films with rhombohedral symmetry, including three A_1 symmetry modes relatively intense peaks in the region I of the spectrum and E modes in the region II of the spectrum with weak scattering intensity **[176, 177].**

Among these observed modes, three A_1 modes as well as the E mode at 270 cm^{-1} should be governed by the Bi-O covalent bonds**[175, 176].** According to crystallography, there are five Raman active modes for *Fd-3m* cubic inverse spinal structure of CFO ($A_{1g}+1E_{g1}+3T_{2g}$). We obtained distinct modes at 210 cm^{-1}, 310 cm^{-1}, 474 cm^{-1}, 616 cm^{-1}, and 694 cm^{-1} for CFO nearly at all the mentioned frequencies which has been previously reported **[177].** Under the common assumption of a *Fd-3m* cubic spinel structure, the strong mode of A_{1g} symmetry expected at highest wave number can be assign to Fe-O stretching vibrations along the cubic (111) direction of the FeO_4 tetrahedra **[177].**

We present a comparison among BFO, CFO and BFO/CFO nanocomposite thin films to study the strain behaviour of the composite structure. It is evident from the fig 4.10 (a) that the signal from the BFO/CFO nanocomposite thin film can be dominated by both BFO and CFO phases are present in composite nanostructure and agreement very well with the previously reported Raman spectra for BFO-CFO thin films in literature **[175].** It is clear from the fig.4.11(a) that the remarkable sharpness of the BFO bands indicated by (*) in region I of BFO/CFO composite nanostructure, attesting the good crystalline quality of BFO. Region II present more complex signature with overlapping and superimposing features of BFO and CFO. We note that CFO presents only low intensity signal in the spectral region I and IV due to lower Raman scattering for CFO in BFO/CFO nanocomposite structure. Finally, the region III is characterized by

dominating CFO band indicated by (+) in BFO/CFO nanostructure. The attributes features in region I, III (sign by arrow in fig 4.11) allow a discussion of strain states of both BFO and CFO. The strain in the nanostructure was study by Raman spectrum mainly via shifts of the Raman bands. An increase and decrease in the wave number is a sign of compressive and tensile strain are present in the nanostructure **[175, 177].** In order to characterize the strain state of the BFO and CFO bands in BFO/CFO composite thin film nanostructure, the Raman spectrum of BFO/CFO nanocomposite thin films compare with the reference data for BFO and CFO thin films. Fig.4.11 (b) make enlarge view of some specific bands of BFO/CFO composite thin films around 138 cm^{-1}, 168 cm^{-1}, 217 cm^{-1} and 693 cm^{-1} which are compared to the reference spectra of BFO and CFO thin films and are considered as a reference for BFO/CFO nanostructure.

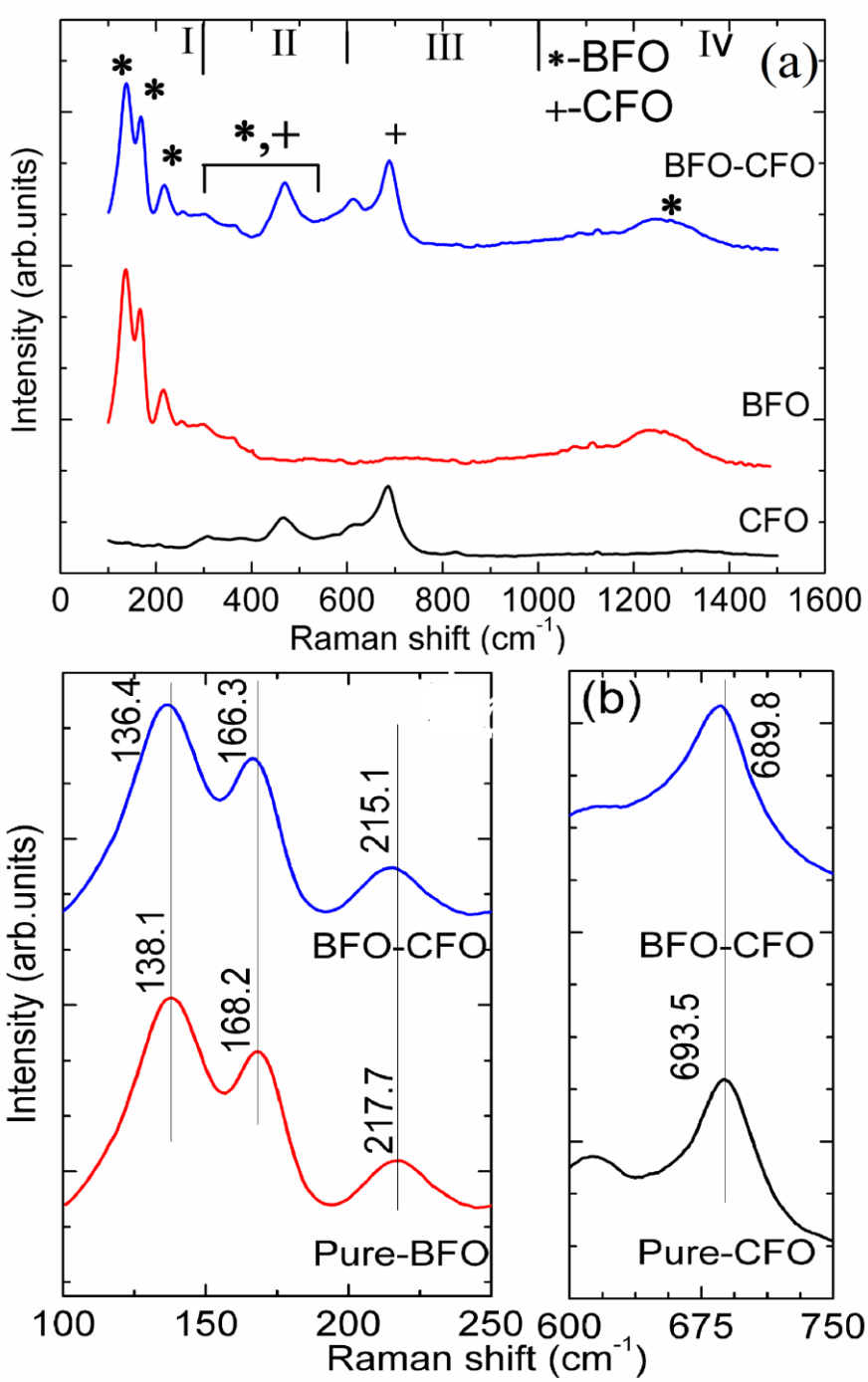

Fig. 4. 11. (a) Raman spectra for a BFO, CFO and BFO/CFO nanostructure. (b) Zoom view of the BFO band at nearly 138 cm^{-1}, 168 cm^{-1}, 217 cm^{-1} and the CFO band at nearly 693 cm^{-1}, 694 cm^{-1}.

It is clear from the fig. 4.11(b) that small but characteristic difference were found to be in the position of BFO and BFO/CFO composite thin films, providing evidence for

different strain states. The bands of BFO and CFO in the BFO/CFO nanostructure exhibits a lower wave number shift with respect to pure BFO and CFO thin film reference data. A closer inspection of nanostructure in fig. 4.11(b) exhibit that there is a 2 cm^{-1} shift in the peak at 136 toward lower wave number side is attributed to a A_1 mode of BFO. There is a significant shift of 4 cm^{-1} were found to be for BFO/CFO nanocomposite thin films as compared to CFO reference peak due to a T_{1g} mode of CFO at 694 cm^{-1}. The lower wave number shift of BFO and CFO bands can be understood by the fact that the change in lattice dimensions of BFO and CFO unit cells in the BFO/CFO nanocomposite thin film spectra indicating that there is a lattice mismatch between BFO and CFO phases, since the unit cell of BFO is smaller than the unit cell of CFO, where BFO is subjected to a tensile strain and CFO is subjected to a compressive strain. Finally, we conclude that the BFO and CFO bands in pure BFO and CFO thin films spectra present the different strain states as compared to BFO/CFO nanocomposite thin films.

4.2.5 Magnetic properties

The in plane *M-H* behaviour for pure BFO and BFO/CFO nanostructures at 300K are presented in fig. 4.12. Pure BFO thin film clearly shows the anti-ferromagnetic behaviour. Whereas, a typical ferrimagnetic hysteresis loop was observed for all BFO/CFO nanocomposite thin films indicating the presence of an ordered magnetic structure. The inset shows the enlargement of the *M-H* curve to clearly show the coercivity of the BFO/CFO composite thin films. The addition of CFO particles in BFO matrix strongly affects the magnetic properties of BFO/CFO nanocomposite thin films. The M_s, M_r and H_c values of BFO/CFO nanocomposite thin films are found to increase with CFO content.

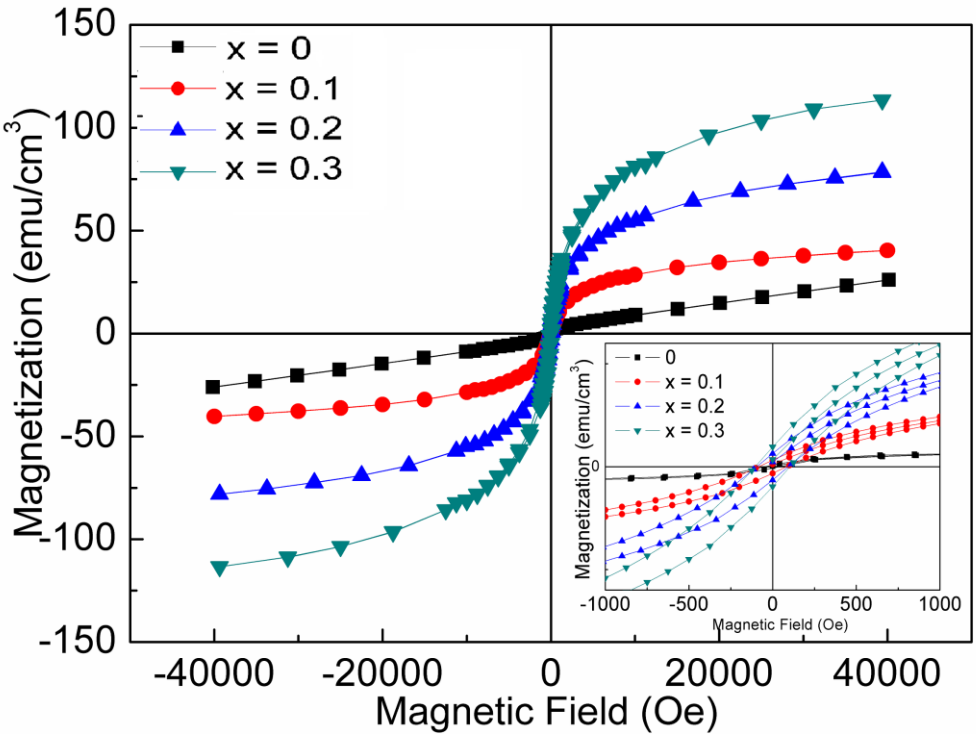

Fig. 4.12 Magnetic hysteresis loops of pure BFO and BFO/CFO nanocomposite thin films. The inset indicates the zoom view of BFO and BFO/CFO nanocomposite thin films at 300K.

The enhancement in H_c in BFO/CFO nanocomposite thin film could be related to magneto-elastic coupling at the interface between anti-ferromagnetic BFO and ferrimagnetic CFO. As discussed above in Raman spectra the CFO phase is under compressive strain caused by the lattice mismatch between the CFO (a = 0.839 nm) and BFO (a = 0.396 nm) phases **[29, 30].** Aimon *et al.* also reported the dependence of strain states on the volume fraction of CFO particles can help to explain the magnetoelastic properties for BFO/CFO nanocomposite thin films **[27, 124].** Fig.4.13 shows the low temperature *M-H* behaviour of the composite thin films. The values of M_r and H_c are found to be increased with decreasing temperature at 100K, although there is no significant change in the value of M_s. Particularly, a large H_c of (~ 6.0 KOe for x = 0.3) is observed for BFO/CFO composite thin films at 100K suggests that the strong exchange coupling between BFO and CFO grains and hard to rotate the spins at low temperature.

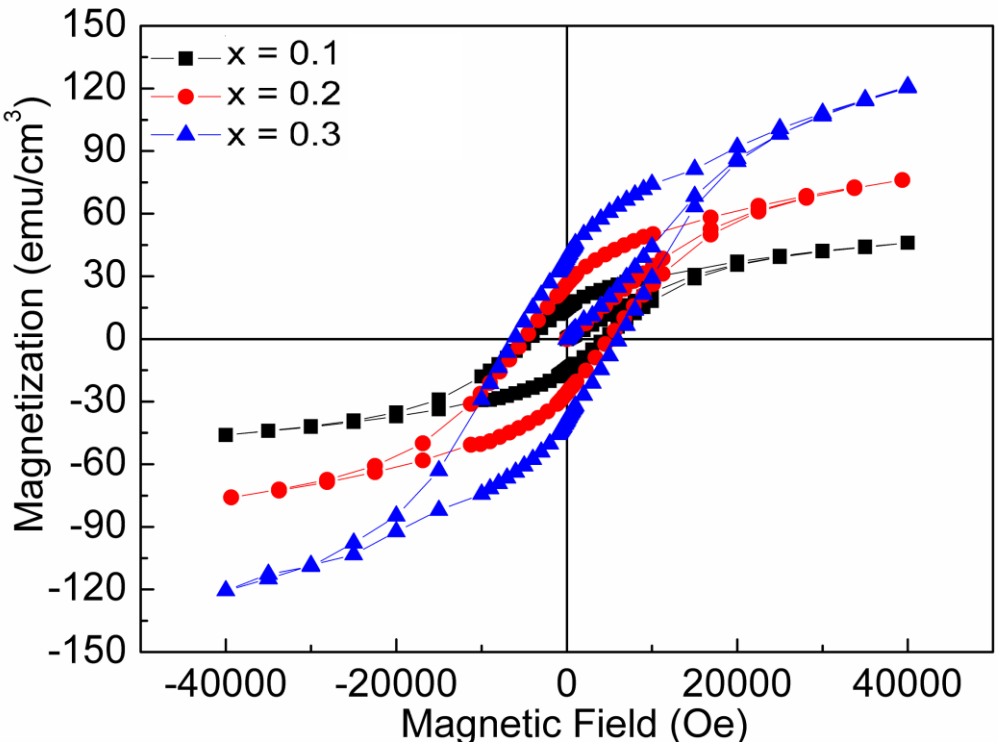

Fig. 4.13 Magnetic hysteresis loop of BFO/CFO nanocomposite thin film at 100K.

4.2.6 Ferroelectric properties

Fig.4.14 shows the ferroelectric (*P-E*) hysteresis loops of the BFO and the BFO/CFO nanocomposite thin films measured at room temperature as a function of CFO concentration at 1Hz. The BFO and BFO/CFO (0.9/0.1) nanocomposite thin films shows the desirable ferroelectric behavior. The P_r value measured for the pure BFO and BFO/CFO(0.9/0.1) thin film are 18μC/cm^2 and 15μC/cm^2 respectively, which are comparable to the previously reported values for thin films prepared by sol-gel method **[124, 178].** While the magnitude of remnant polarization decreases continuously with ferrite content increases and found to be P_r = 12 μC/cm^2, 10 μC/cm^2 for BFO/CFO (0.8/0.2) and BFO/CFO (0.7/0.3) nanocomposite thin films respectively. Remarkable lossy behaviour for BFO/CFO (0.7/0.3) nanocomposite thin film is observed and non saturated *P-E* loops are observed. Such type of lossy *P-E* loops are often observed in samples with higher conductivity and are often named as non- ferroelectric *P-E* loops. The paraelectric cobalt ferrite phase is responsible for the decrease in the ferroelectric properties.

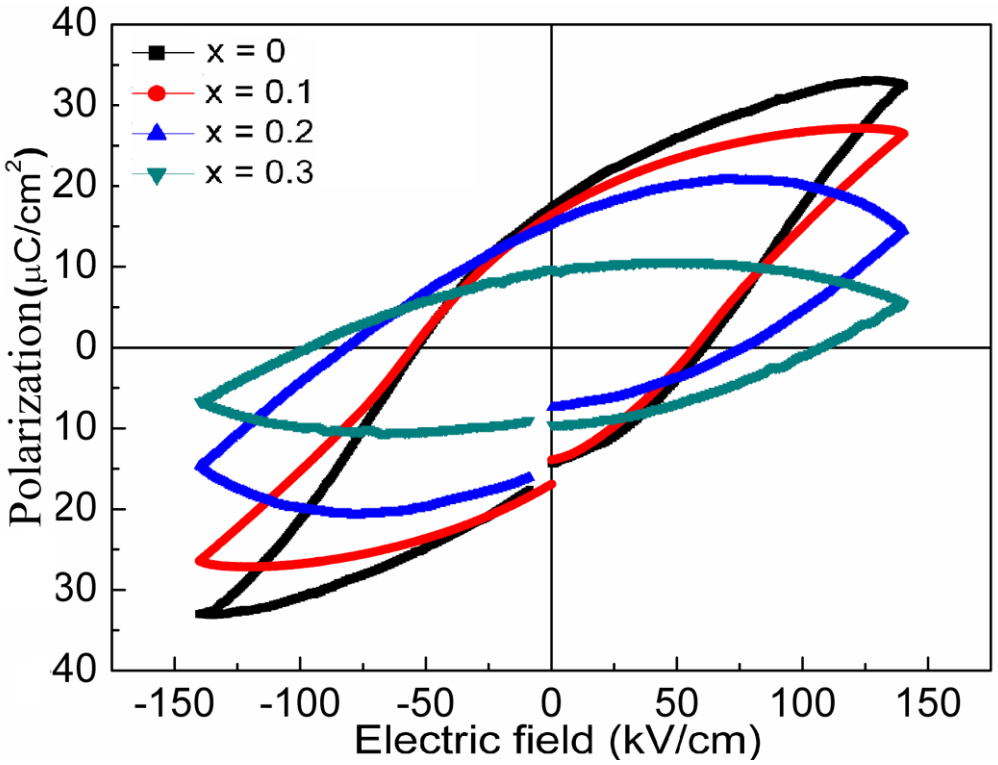

Fig. 4.14 *P-E* loops of pure BFO and BFO/CFO nanocomposite thin films.

4.2.7 Dielectric properties

Fig.4.15 shows the frequency dependence dielectric constant of both BFO and BFO/CFO nanocomposite films at room temperature. There are many factors which can affect the dielectric behaviour of the ferrite materials such as grain size, cation distribution, porosity, crystal defects and method of sintering etc **[161-163].** In a low frequency regime, interfacial/surface polarization plays a dominant role in determining the dielectric properties of nanoferrite materials. The contribution from surface polarization, at low frequency which gives an initial high value that decays rapidly with frequency as it cannot follow the higher applied frequency. It is evident that in low frequency region, all the samples show frequency dispersion i.e. a rapid decrease in dielectric constant with frequency, can be attributed due to the well known interfacial polarization predicted by the Maxwell-Wagner model**.** Also, in this study dielectric behavior of BFO/CFO nanocomposite thin films is found to be higher than that of pure BFO film in low frequency region; as the incorporation of CFO lead to an increase interfacial area and grain boundary resistance of composite material causing an additional interfacial

polarization. It is also seen that the there is a decrease in dielectric constant at higher frequencies and becomes almost constant, which is because of the jumping frequency of electric dipoles does not follow the alternating electric field beyond a certain critical frequency **[163].** However, the dielectric constant decreases slowly in pure BFO thin films with increasing frequency showing that it is more frequency dependent in high frequency region and has higher dielectric constant than CFO/BFO.

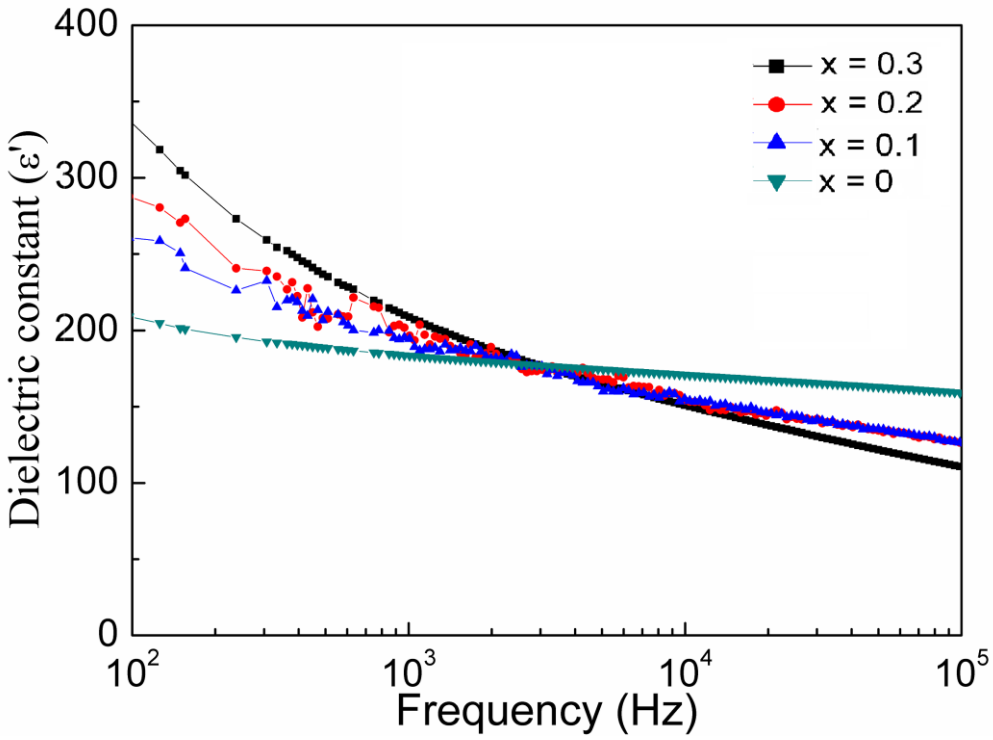

Fig. 4.15 Dielectric constant of BFO and BFO/CFO nanocomposite thin films.

4.3 $BiFeO_3$-$CoFe_2O_4$ composite thin films annealed at 650 ºC

4.3.1 XRD analysis

XRD patterns for (1−*x*)BFO-*x*(CFO) with (*x*=0, 0.1, 0.2, 0.3) nanocomposite thin films annealed at 650 °C are shown in fig.4.16. The XRD pattern indicates that both BFO and CFO phases are polycrystalline in nature and have no preferential crystallographic orientations.

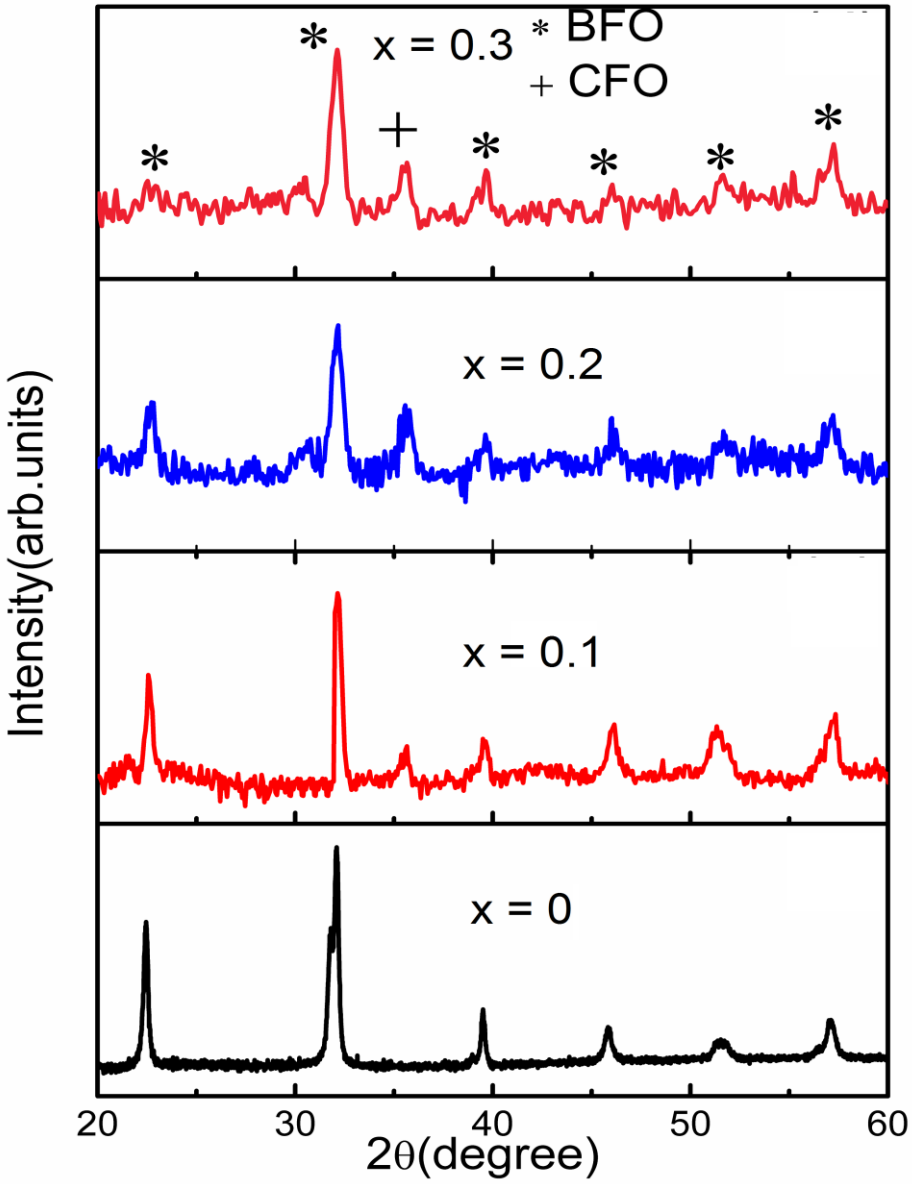

Fig. 4.16. X-ray diffraction pattern of multiferroic pure BFO and BFO/CFO nanocomposite thin films.

XRD pattern of all composite samples establish the presence of well defined peaks of perovskite BFO phase with sharp (110) peak and other to the cubic spinel CFO phase. Moreover, due to the low volume ratio of CFO as compared to BFO, the CFO grains were trapped around the ferroelectric grains of BFO phase, and its growth was found to be restrained. As a result of which no prominent diffraction peaks rather than (311) for spinel CFO is seen in the XRD spectrum for all composite thin films.

4.3.2 AFM analysis

Fig.4.17 (a) and (b) shows the two dimensional AFM images of BFO and BFO/CFO nanocomposite thin films annealed at 650 °C. It is evident from the AFM micrographs that the BFO/CFO composite sample consists of randomly distributed fine CFO particles in BFO matrix. The root mean square roughness (*Rq*) values are measured using the 10 µm x 10 µm area for better statics and found to be ~ 5.32nm and ~ 6.63nm for the films BFO and BFO/CFO nanocomposite thin films respectively.

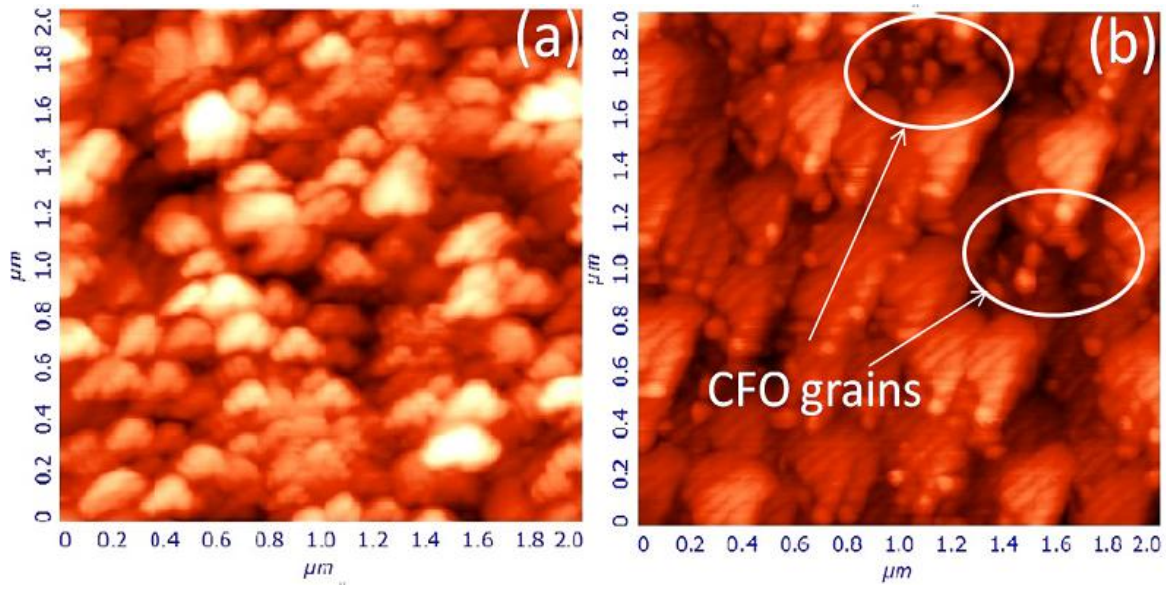

Fig. 4.17. AFM micrographs of (a) BFO and (b) BFO/CFO nanocomposite thin films.

4.3.3 TEM analysis

TEM measurements was done to further confirm the crystallization of CFO phase in the composite structure. Fig. 4.18 (a) and (b) shows the plane view TEM image and corresponding selected area electron diffraction pattern of BFO/CFO composite thin

films respectively. Fig. 4.18 (a) clearly depicts that CFO phase (dark) is embedded in BFO (light) matrix, which indicates nanoscale mixing of the BFO and CFO phases. The diffraction spots of both BFO and CFO were observed in the BFO/CFO composite structure indicating the distribution of BFO and CFO particles in the area.

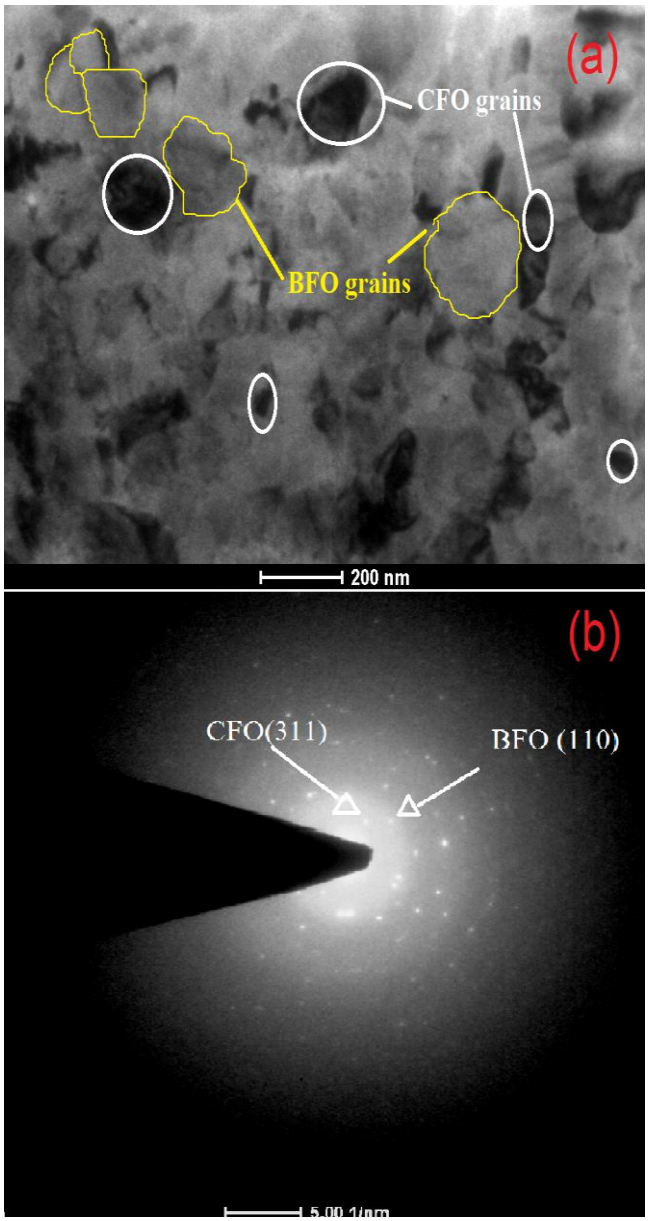

Fig. 4.18. Representative TEM image of (a) BFO/CFO film shows the CFO particles (dark) embedded in BFO matrix (b) selected area electron diffraction pattern of BFO/CFO composite thin films.

The calculated d_{hkl} values as per the respective diffraction ring shown in fig. 4.18 (b) for BFO and CFO are found to be d_{110} = 0.278 nm, an d_{311} = 0.252 nm respectively.

4.3.4 Magnetic properties

Fig. 4.19 shows the in plane *M-H* behavior of all the samples with varying volume concentration of CFO at 300K. Pure BFO thin film clearly shows the anti-ferromagnetic behaviour due to its magnetism arises from the self-canted spin magnetic moments of Fe^{3+}.

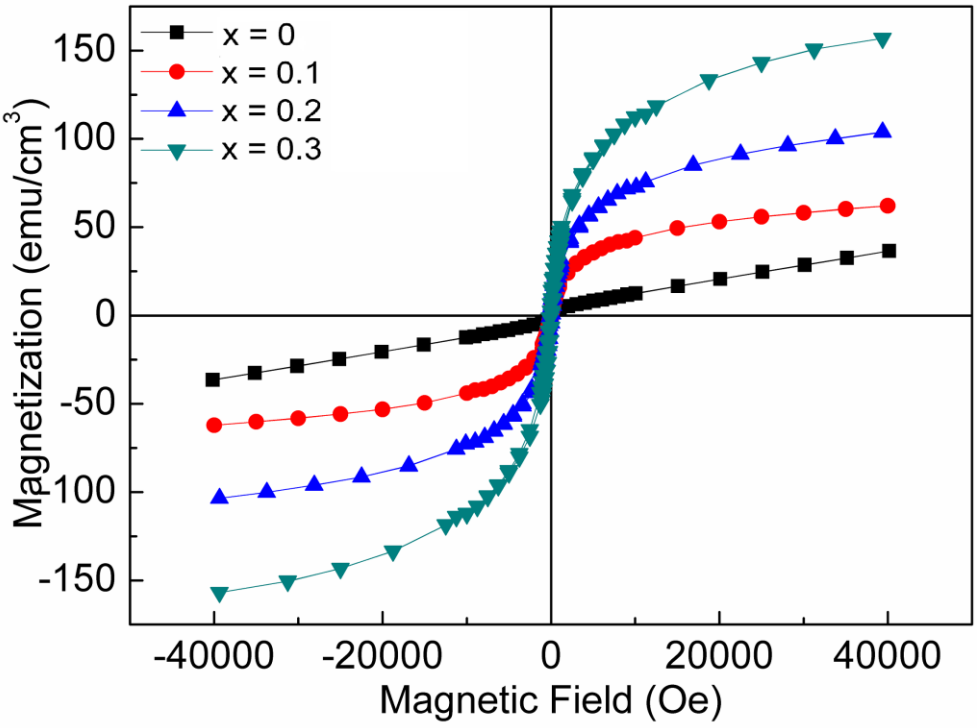

Fig. 4.19. Magnetic hysteresis loops of BFO and BFO/CFO nanocomposite thin films at 300K.

Whereas, a well defined magnetic hysteresis loop was observed in BFO/CFO nanocomposite thin films. Which indicates that the major contribution to magnetic moments of the BFO/CFO nanocomposite thin films mainly arises from the CFO. The concentration of CFO strongly affects the magnetic properties of BFO/CFO. The M_s, M_r and coercivity (H_c) values of BFO/CFO nanocomposite thin films are found to increase with increase in the CFO concentration. The maximum values of M_s and M_r are ~ 158

emu/cc and 12.8 emu/cc respectively for x=0.30 concentration. It is also evident that coercivity increases sharply for x = 0.3 (inset fig 4.19). This could be attributed due to magnetoelastic coupling between anti-ferromagnetic BFO and ferromagnetic CFO phase **[34, 35, 124].** Fig. 4.20 shows the *M-H* hysteresis loops measured at 100 K. The values of M_r, and M_s increase significantly with decreasing temperature due to the suppression of thermal fluctuation of magnetic dipoles at low temperature. A large H_c of 6.25 KOe was observed at 100K which suggests that presence of a strong exchange interaction between BFO and CFO grains is dominant at low temperature.

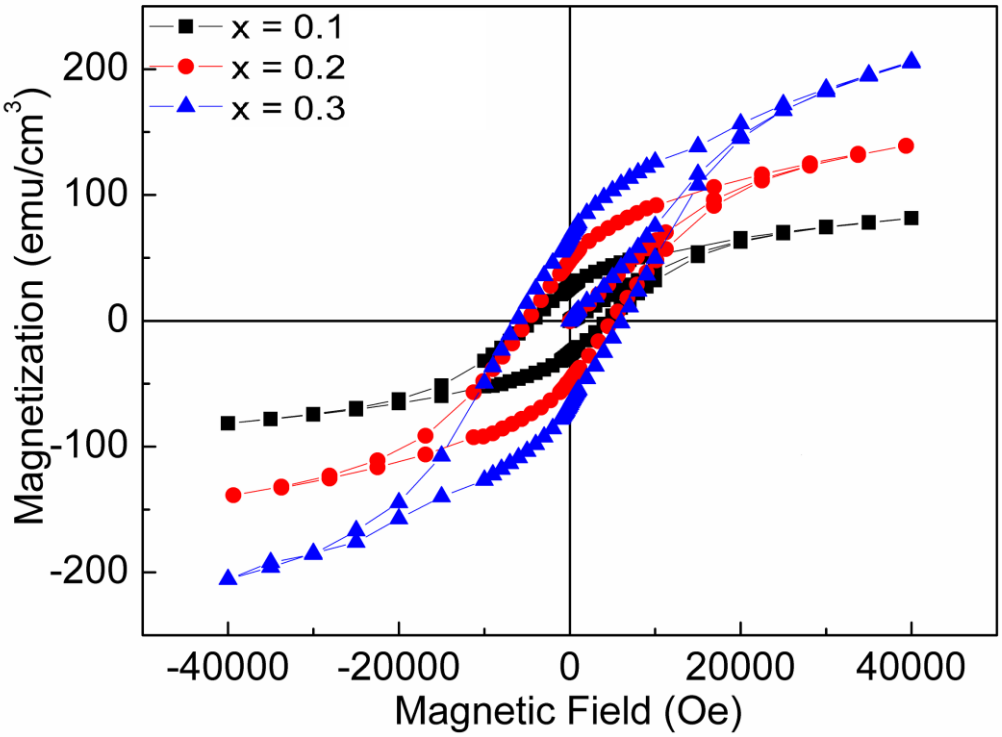

Fig. 4.20. Magnetic hysteresis loops for BFO/CFO nanocomposite thin films at 100K.

4.3.5 Ferroelectric properties

Fig.4.21 shows the *R-T* polarization vs. applied electric field (*P-E*) hysteresis loops for (1-x)BFO-*x*CFO (x = 0, 0.1, 0.2, 0.3) nanocomposite thin films as a function of CFO concentration measured at maximum applied field of 100 kV/cm. The BFO and BFO/CFO nanocomposite thin films show the desirable ferroelectric behaviour. However, ferroelectric properties degraded for all samples annealed at 650 °C as

compared to films annealed at 600 °C in our previous section. BFO being a volatile material at the higher annealing temperature causes higher bismuth loss at 650 °C which strongly affect the ferroelectric properties resulting non saturated ferroelectric loops are observed for all the films annealed at 650 °C. Also, polarization value continuously decrease with increasing magnetic component. The paraelectric cobalt ferrite phase is responsible for the decrease in the ferroelectric properties. Particularly, poor ferroelectric behaviour are observed for BFO/CFO (0.7/0.3) composite due to higher weight % of CFO phase. The remnant polarization (P_r) value measured for the BFO and BFO/CFO (0.7/0.1) thin film are comparable to the previously reported values for thin films prepared by sol-gel method **[124, 178].**

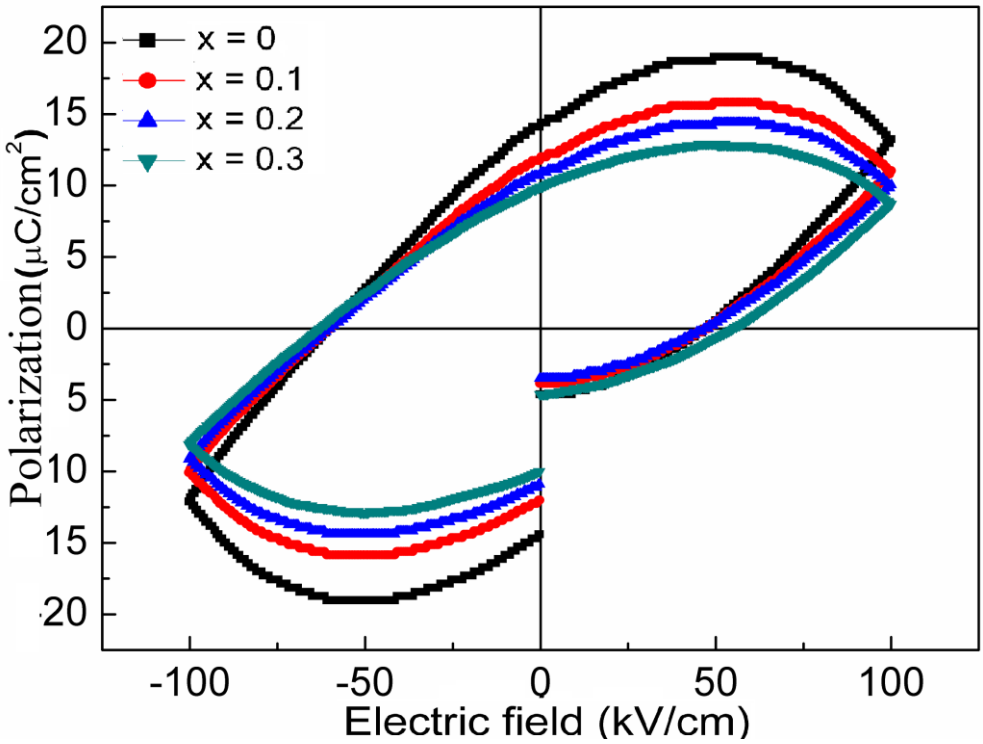

Fig. 4.21. Polarization-electric field hysteresis loops for and BFO/CFO nanocomposite thin films.

4.3.6 Dielectric properties

The frequency dependence dielectric constant of both pure BFO and BFO/CFO nanocomposite films is shown in fig. 4.22. In a low frequency regime, interfacial/surface polarization plays a dominant role in determining the dielectric properties of nanoferrite

materials. The contribution from surface polarization, at low frequency which gives an initial high value that decays rapidly with frequency. It is clear from the fig. 4.22 that in low frequency region, all the samples show frequency dispersion i.e. a rapid decrease in dielectric constant with frequency, can be attributed due to the well known interfacial polarization predicted by the Maxwell-Wagner model**.** Moreover, in this study dielectric behaviour of BFO/CFO nanocomposite thin films is found to be higher than that of pure BFO film in low frequency region; as the incorporation of CFO lead to an increase interfacial area and grain boundary resistance of composite material causing an additional interfacial polarization. It is also seen that the there is a decrease in dielectric constant at higher frequencies and becomes almost constant, which is because of the jumping frequency of electric dipoles does not follow the alternating electric field beyond a certain critical frequency **[180].** However, the dielectric constant decreases slowly in pure BFO thin films with increasing frequency showing that it is more frequency dependent in high frequency region and has higher dielectric constant than CFO/BFO.

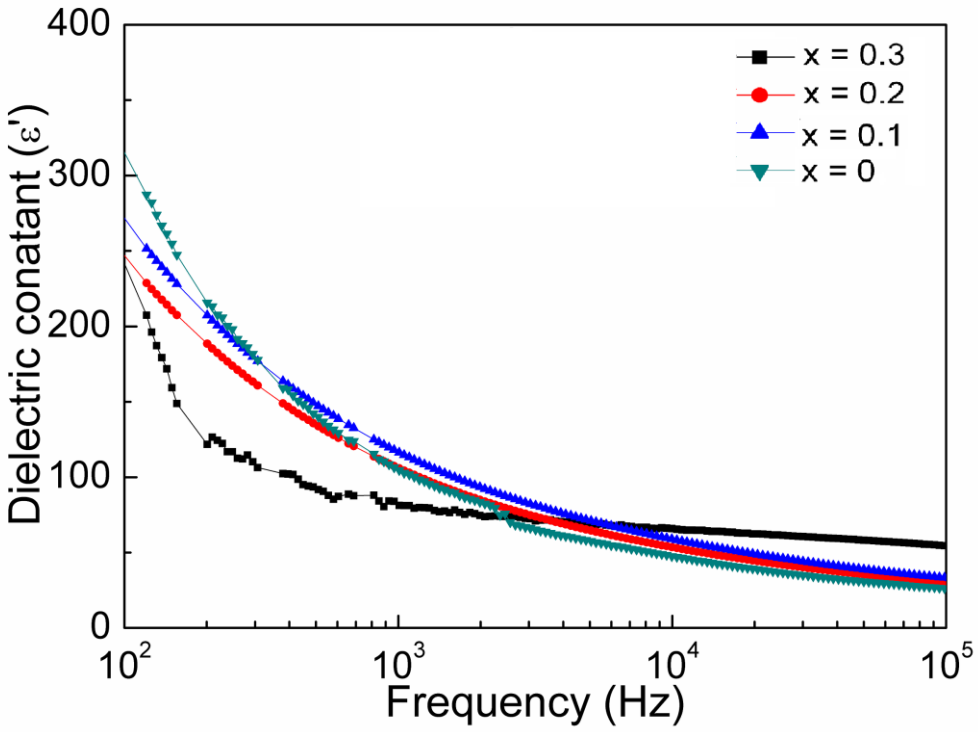

Fig. 4.22 Dielectric constant of BFO and BFO/CFO nanocomposite thin films.

4.4 $BiFeO_3$-$NiFe_2O_4$ composite thin films

In previous part of this chapter, We used CFO as the magnetic component to improve the multiferroic behavior of BFO-CFO nanocomposites thin films. In this chapter another $NiFe_2O_4$(NFO) is used as magnetic phase to improve the Multiferroic behaviour of nanocomposite thin films. NFO, an inverse spinel ferrite having low magnetocrystalline anisotropy energy could be a good candidate for preparation of BFO/NFO nanocomposite thin films. A very few reports are available on BFO-NFO based nanocomposite thin films considering NFO as the ferrite component **[182, 183].** Recently, Gu. *et al.* (2014) reported the effect of NFO on the magnetoelectric coupling effect of BFO thin films [184]. In this part BFO/NFO composite films are prepared and their electrical and magnetic properties with varying NFO fractions are studied.

4.4.1 XRD analysis

Fig.4.23 displays the XRD pattern indium tin oxide (ITO) coated glass substrate, BFO, NFO and for all BFO/NFO nanocomposite thin films after annealing at 600ºC. The XRD patterns of BFO and NFO exhibit the peaks of perovskite BFO and the cubic spinel symmetry NFO respectively. The peaks corresponding to NFO in BFO/NFO composite thin films spectra are not observed due to superimposition of NFO peaks with both BFO and ITO peaks. Moreover, due to the low volume ratio of NFO as compared to BFO, the NFO grains were trapped around the ferroelectric grains of BFO phase, and its growth was found to be restrained **[183].** As a result of which no prominent diffraction peaks for spinel NFO are seen in the XRD spectrum. The intensity of X-ray reflections corresponding to BFO phase can be clearly seen to decrease with increasing the magnetic phase in the composites. No other secondary phases were identified, which confirms the absence of any chemical reaction between two phases during high temperature annealing process.

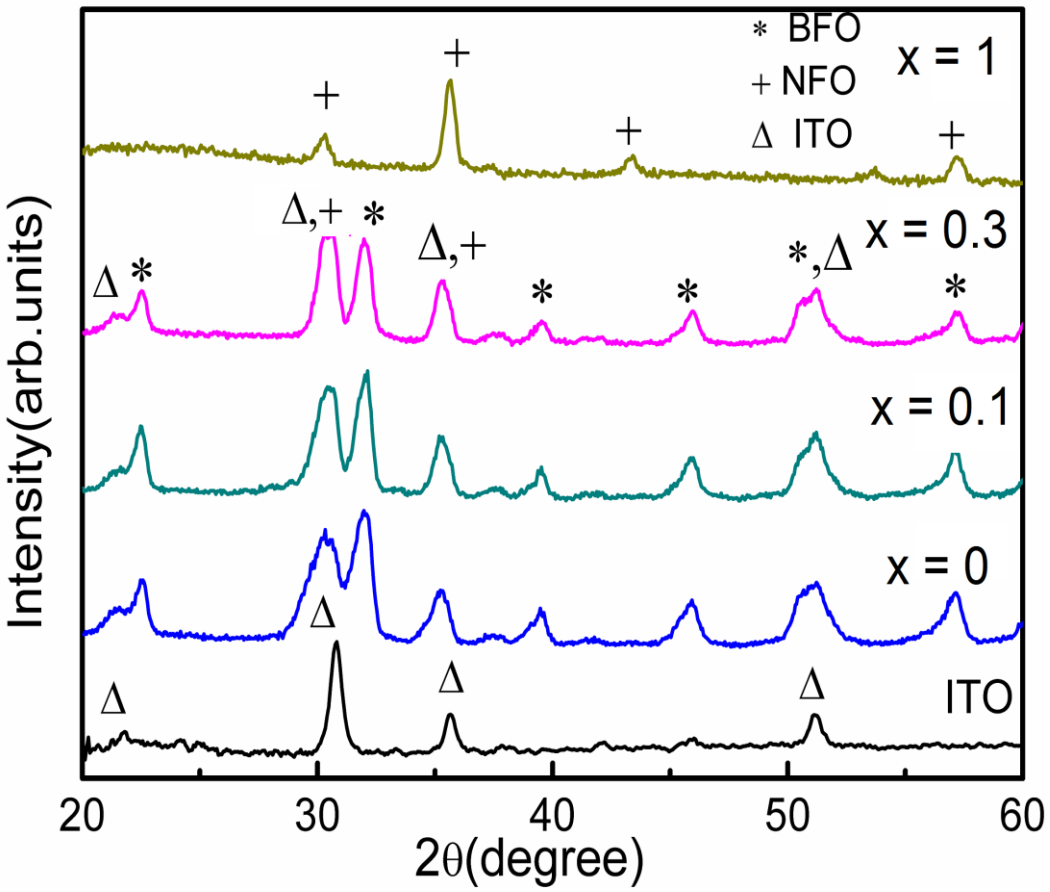

Fig. 4.23. XRD pattern of BFO, NFO and BFO/NFO nanocomposite thin films.

4.4.2 TEM analysis

To further confirm the crystallisation of NFO phase in composite thin film, TEM analysis was done. Fig. 4.24 (a) shows the plane view TEM image of BFO/NFO (x = 0.1) nanocomposite thin film and fig. 4.24 (b) shows the corresponding selected area electron diffraction pattern (SAED). Fig. 4.24 (a) clearly depicts that NFO having lighter Ni atoms appear dark, is embedded in BFO matrix which appears bright because of containing heavier Bi atoms, indicating nanoscale mixing of the BFO and NFO phases **[184].** The diffraction spots of both BFO and NFO are also observed in SAXD of BFO/NFO nanocomposite thin film structure indicating the distribution of BFO and NFO particles in the area. The calculated $d_{h\ k\ l}$ values as per the respective diffraction ring shown in Fig. 4.24 (b) for BFO and NFO are found to be d_{110} = 0.279 nm, and d_{311} =

0.250 nm respectively. Fig.4.24 (c) shows the cross-sectional image of BFO thin film, the thickness of the film is determined to be ~ 200nm.

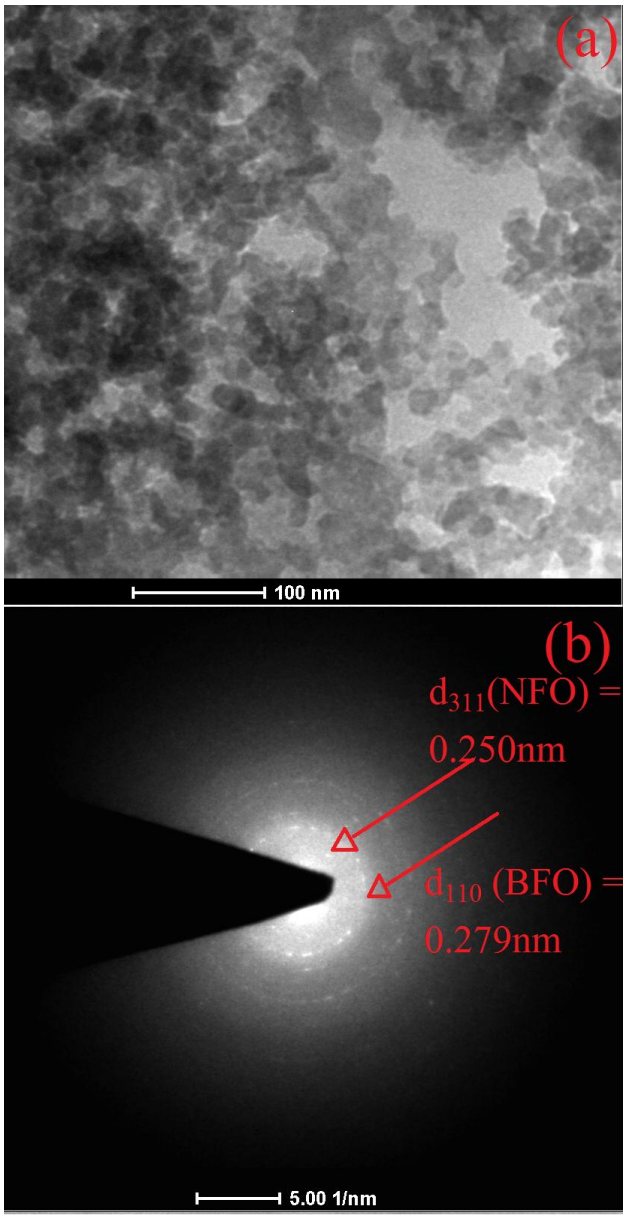

Fig. 4.24. In plane TEM image of (a) BFO/NFO nanocomposite thin films (b) selected area diffraction pattern of BFO/NFO composite thin film**s**

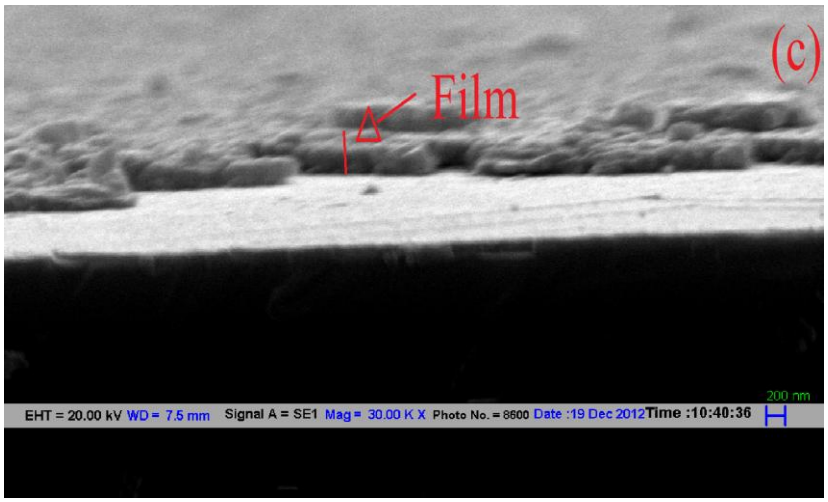

Fig. 4.24. The cross section image of (c) BFO/NFO thin film annealed 600 °C**.**

4.4.3 AFM analysis

Fig.4.25 (a), (b) and (c) shows the surface morphology of BFO, NFO and BFO/NFO (x=0.1) thin films obtained from the atomic force microscopy (AFM). The micrograph suggests the films are dense and well crystallized. The introduction of NFO grains in BFO matrix greatly affect the surface morphology of BFO thin films. Particularly, the fine grain size and lower roughness value of the BFO/NFO nanocomposite thin films are observed as compared to BFO thin films. The root mean square roughness (*Rq*) values are measured using the 10 μm x 10 μm area for better statics and found to decrease for composite thin films as compared to BFO. The *Rq* values are ~ 9.32nm, ~ 6.29 and ~ 5.33 nm for BFO, BFO/NFO and NFO thin films respectively.

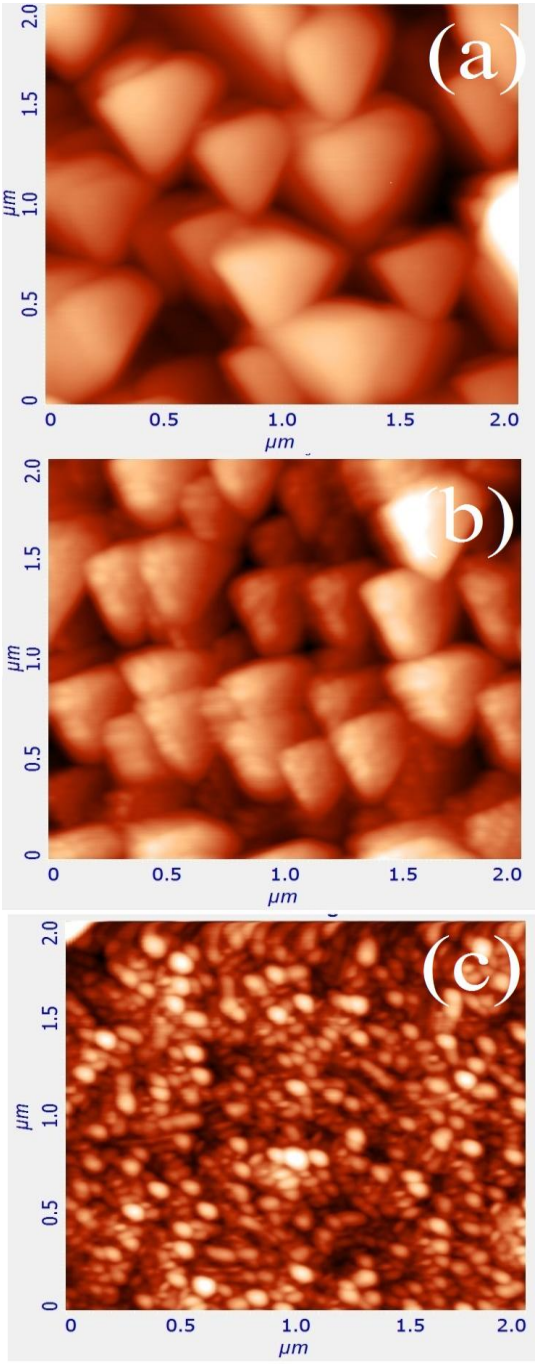

Fig. 4.25. AFM images of (a) BFO (b) BFO/NFO and (c) NFO thin films.

4.4.4 Magnetic properties

Fig.4.26 shows the in plane *M-H* behaviour of BFO and BFO/NFO (x = 0.1) nanocomposite thin films at 300K. BFO sample typically exhibit the anti- ferromagnetic behaviour which arises due to uncompensated spin magnetic moments of Fe^{3+}.

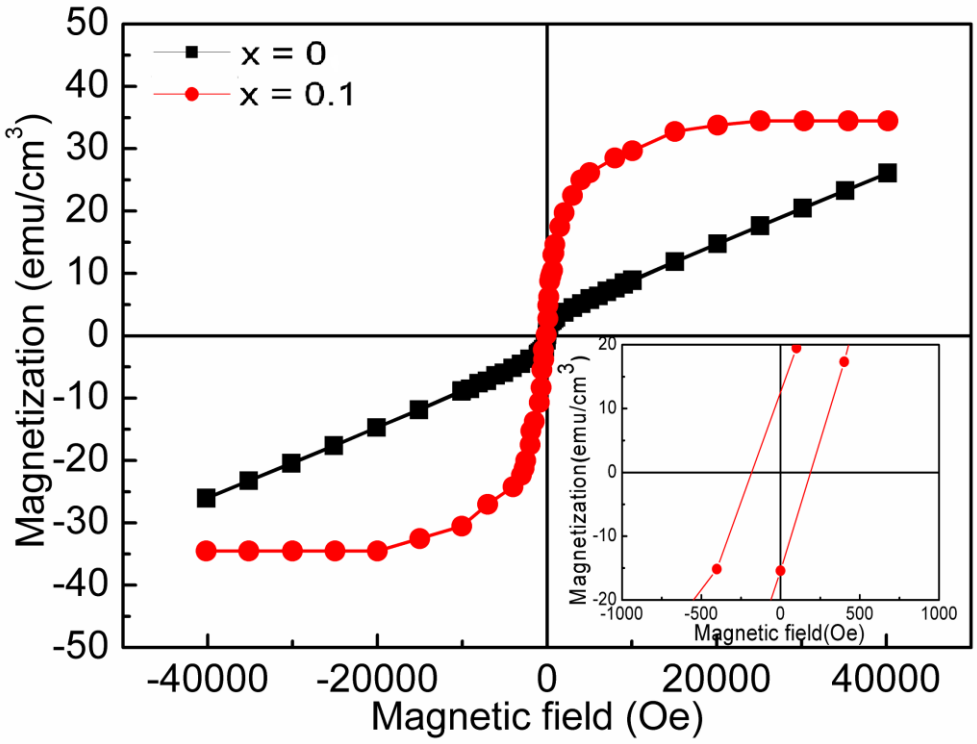

Fig. 4.26 Magnetic hysteresis loops of BFO and BFO/CFO(x = 0.1) nanocomposite thin films at 300K and the inset is zoom view of the central part of the figure.

Whereas, the well saturated *M-H* loop was observed for BFO/NFO nanocomposite thin films. This indicates that the major contribution to magnetic moment of the BFO/NFO nanocomposite thin films mainly arises from NFO. The saturation magnetization (M_s) and remnant magnetization (M_r) were found to be as high as ~ 34 emu/cm^3 and ~ 7 emu/cm^3 respectively for x = 0.1. This suggests that the ferromagnetic character of the composite sample is sustained with NFO content ~ 0.1 in our samples. Moreover, the magnetic properties can be tuned in BFO-NFO nanocomposite strictures.

4.4.5 Ferroelectric properties

Fig.4.27 displays the *RT* ferroelectric (*P-E*) loops for (1-x)BFO–xNFO (x = 0, 0.1, 0.2, 0.3) nanocomposite thin films measured at maximum field of 150 kV/cm. All samples shows non-saturated hysteresis loops due the leakage current **[186].** The polarization continuously decreases with increasing NFO content. Inset of Fig. 4.27 shows the *P-E* loops for BFO measured at 1Hz, 100 Hz and 500 Hz respectively. It can be observed that

polarization values decreases with frequency, demonstrating the frequency dependent ferroelectric behaviour of the samples.

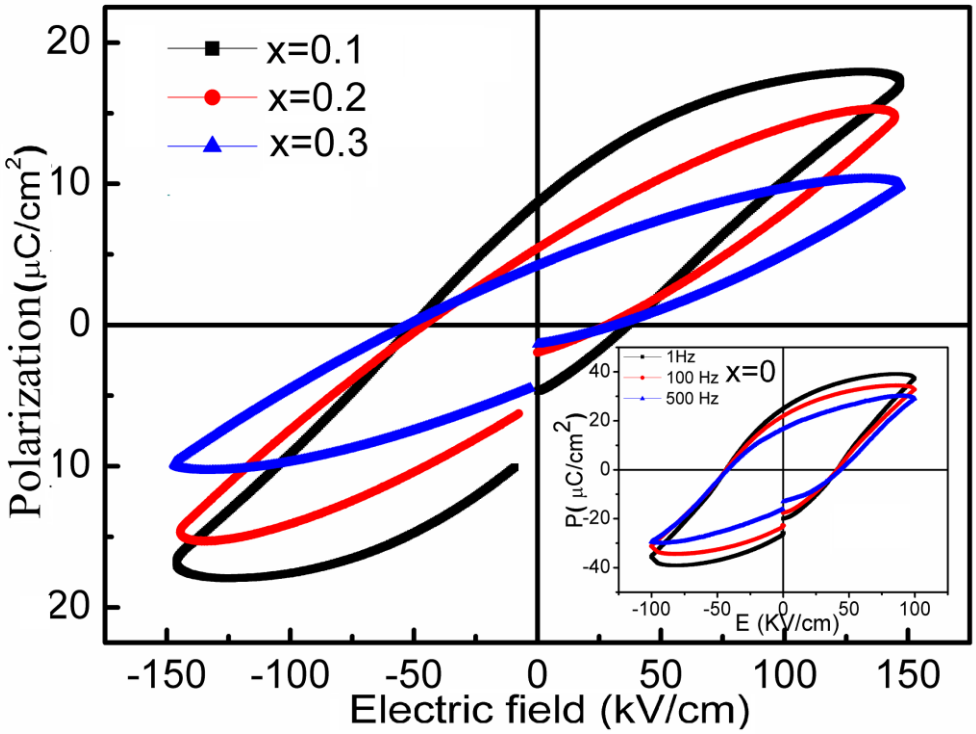

Fig. 4.27 *P-E* loops of BFO and BFO/NFO nanocomposite thin films. Inset of fig. 4.27 shows the P-E loops of *x*=0 sample at different frequencies.

Similar frequency dependent ferroelectric behaviour are observed for remaining samples in our series (not shown) and in accordance with previously reported frequency dependent ferroelectric behaviour in BT-NFO based composite samples **[187].** The value of P_r observed in our study is much higher than those previously reported **[124, 178].** Particularly, the dominant lossy behaviour of *P-E* loop with x = 0.3 composite sample can be attributed to higher content of NFO, which lead to increase in conductivity of composite sample **[186].**

4.4.6 Dielectric properties

Fig. 4.28 (a) and (b) shows the *RT* frequency dependent dielectric constant (ε') and dielectric loss (tanδ) of (1-x)BFO–xNFO (x = 0, 0.1, 0.2, 0.3) nanocomposite thin films measured at 1kHz. It can be observed that ε' for all the samples decreased with

increasing frequency, from 100 Hz to 10 kHz. Particularly, in low frequency region, all the samples show frequency dispersion dielectric behaviour i.e. a rapid decrease in ε' with frequency and becomes almost constant, can be attributed due to well known interfacial polarization predicted by the Maxwell-Wagner model in conformity with koops phenomenological theory **[188, 189].**

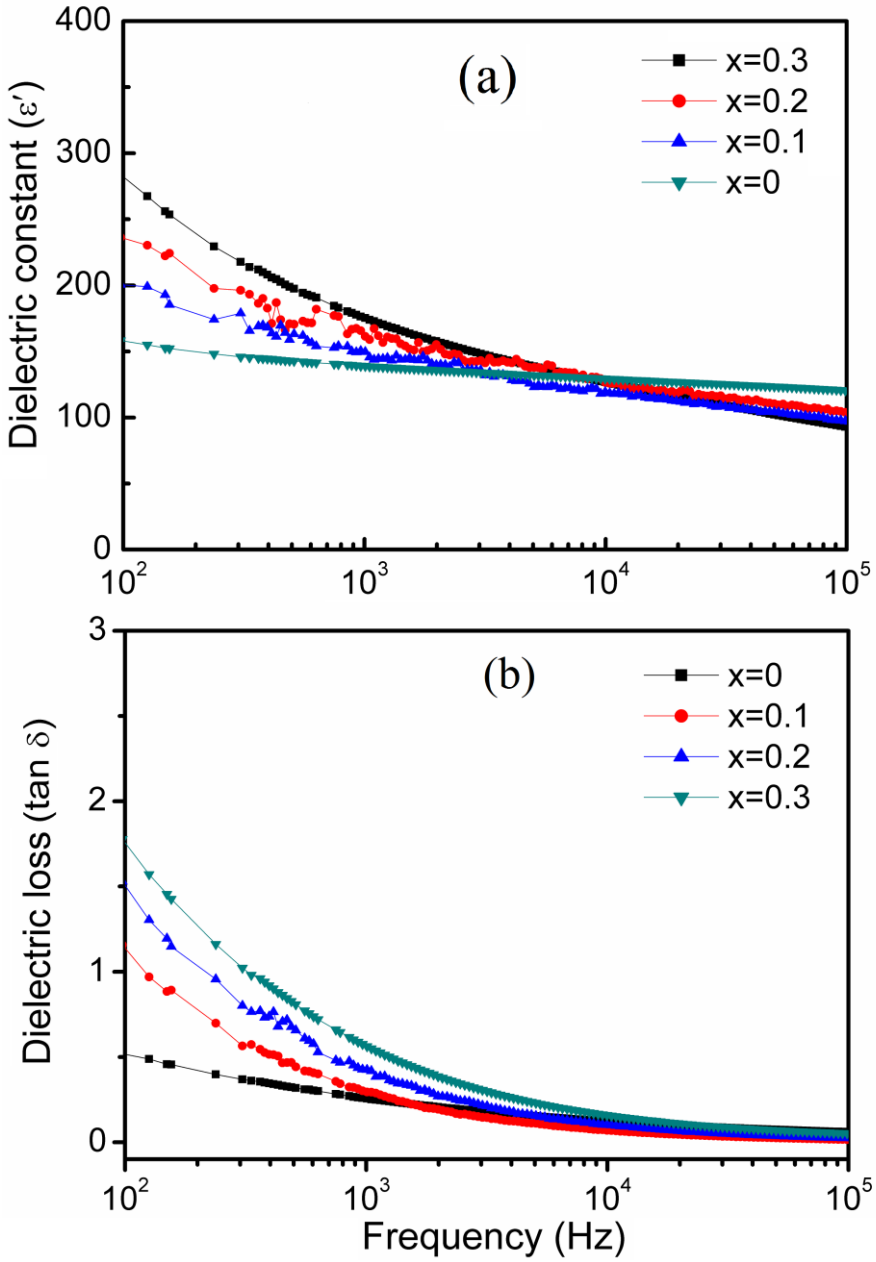

Fig. 4.28 The frequency dependent (a) ε′ and (b) tan δ of BFO and BFO/NFO nanocomposite thin films.

However, ε' value for BFO thin films decreases slowly with increasing frequency as compared to BFO/NFO nanocomposite thin films. This suggest more frequency dependent dielectric behaviour of BFO in high frequency region and has higher ε' than BFO/NFO. In a low frequency regime, interfacial/surface polarization plays a dominant role in determining the dielectric properties of nanoferrite materials, which gives an initial high value that decays rapidly with frequency as it cannot follow the higher applied frequency. More importantly, in this study dielectric behaviour of BFO/NFO nanocomposite thin films is found to be higher than that of pure BFO film mainly in low frequency region. The incorporation of NFO reduces the grain size of the films which leads to an increased interfacial area causing an additional interfacial polarization. As shown in fig. 4.28 (b), a gradual drop in tanδ are also observed in (1-x)BFO–xNFO(x=0, 0.1, 0.2, 0.3) thin films as the frequency increases. This kind of ε' and tanδ behaviour are expected for ferroelectric thin films and are in well agreement with those previously reported in literature for BFO/NFO based composites **[42, 190].**

4.5 72.5BNT-22.5BKT-5BMgT]–NFO particulate composite

The investigations based on piezoelectric–ferrite particulate *ME* composite includes PZT, BT, BFO etc. as the piezoelectric constituents and CFO and NFO as the magnetostrictive constitute **[181, 191-195].** However, high piezoelectric coefficient (d_{33} ~ 600pm/V) and high electromechanical coupling coefficient (k_p ~ 0.7) of PZT is difficult to match with other non lead based piezoelectric materials **[36].** But, due to the toxic nature of Pb, the non lead based *ME* composites were also studied **[45, 194].** Among the other alternatives of non-lead based piezoelectric oxides BNT is one of the widely studied piezoelectric material possessing a high curie temperature (T_c) ~ 320 °C and large remnant polarization (P_r) ~ 38 μC/cm^2 **[37].** However, its high coercivity (E_c ~ 73 kV/cm) makes it difficult to pole and thus have a smaller piezoelectric coefficient (d_{33} ~ 80 pC/N). Therefore, to improve its piezoelectric properties, BNT has been modified with solid solutions of BT, KT, KNN and BMgT **[37-40].** The studies on BNT based particulate composite is very scarce; the few reported studies on BNT-CFO and BNT-NFO based particulate composite has showed evidence of magnetoelectric response in such systems **[50, 51].** In this work, sol-gel assisted (1-*x*)[72.5BNT-22.5BKT-5BMgT] – *x* NFO (x = 0, 0.1, 0.2, 0.3) particulate composite series has been prepared and their structural, magnetic, dielectric and magnetoelectric properties has been investigated.

4.5.1 XRD analysis

Fig.4.29 displays the XRD pattern of BNT-BKT-BMgT, NFO and composites sample. XRD patterns for all the composite samples shows that the composites are prepared in the ferroelectric region. XRD of composite samples consist of all the characteristic peaks of NFO and BNT-BKT-BMgT phases. No other secondary phases were identified, which implies no significant chemical reaction has taken place at the piezoelectric-ferrite interface during the high temperature sintering process, which is essential for proper composite formation. Intensity of X-ray reflections corresponding to magnetic phase increases with increasing magnetic content in the composites.

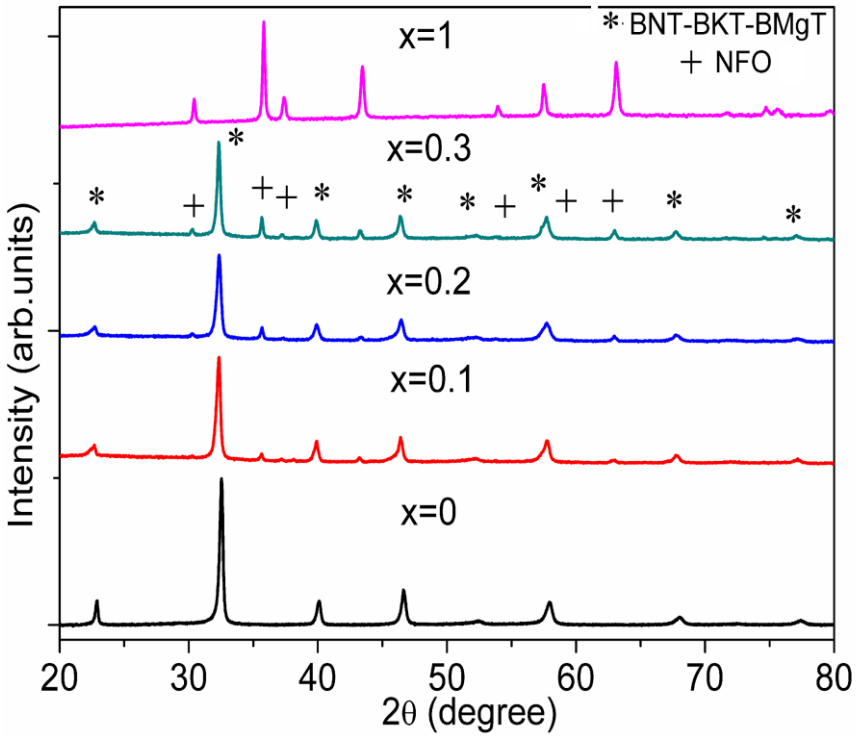

Fig. 4.29. XRD patterns of $(1-x)$[72.5(BNT)-22.5(BKT)-5(BMgT)] − NFO (x = 0.0, 0.1, 0.2, 0.3, 1) *ME* composite.

4.5.2 SEM and EDX analysis

Fig.4.30 (a), and (b) show the SEM micrographs of fracture surface of BNT-BKT-BMgT, NFO and composite sample with (x = 0.2), sintered at 900ºC. In case of particulate *ME* composites, the microstructure plays an important role to get the *ME* output of the composites. To achieve a large value of (α_E), the magnetic phases should be well dispersed in the high resistive piezoelectric matrix. The micrograph suggests the samples are well sintered and dense. The BNT-BKT-BMgT sample shows larger grains as compared to composite sample. The addition of NFO promotes reduction in the grain size with little porosity as reported earlier **[192, 196].** The reduction in grain size could be the result of pinning action by NFO in the composite **[197].** The representative EDX spectra shown in fig. 4.30 (d) acquired from the sample. The representative EDX spectra confirms the presence of Bi, Na, K, Mg, Ti, Ni, Fe and O elements in the composite structure.

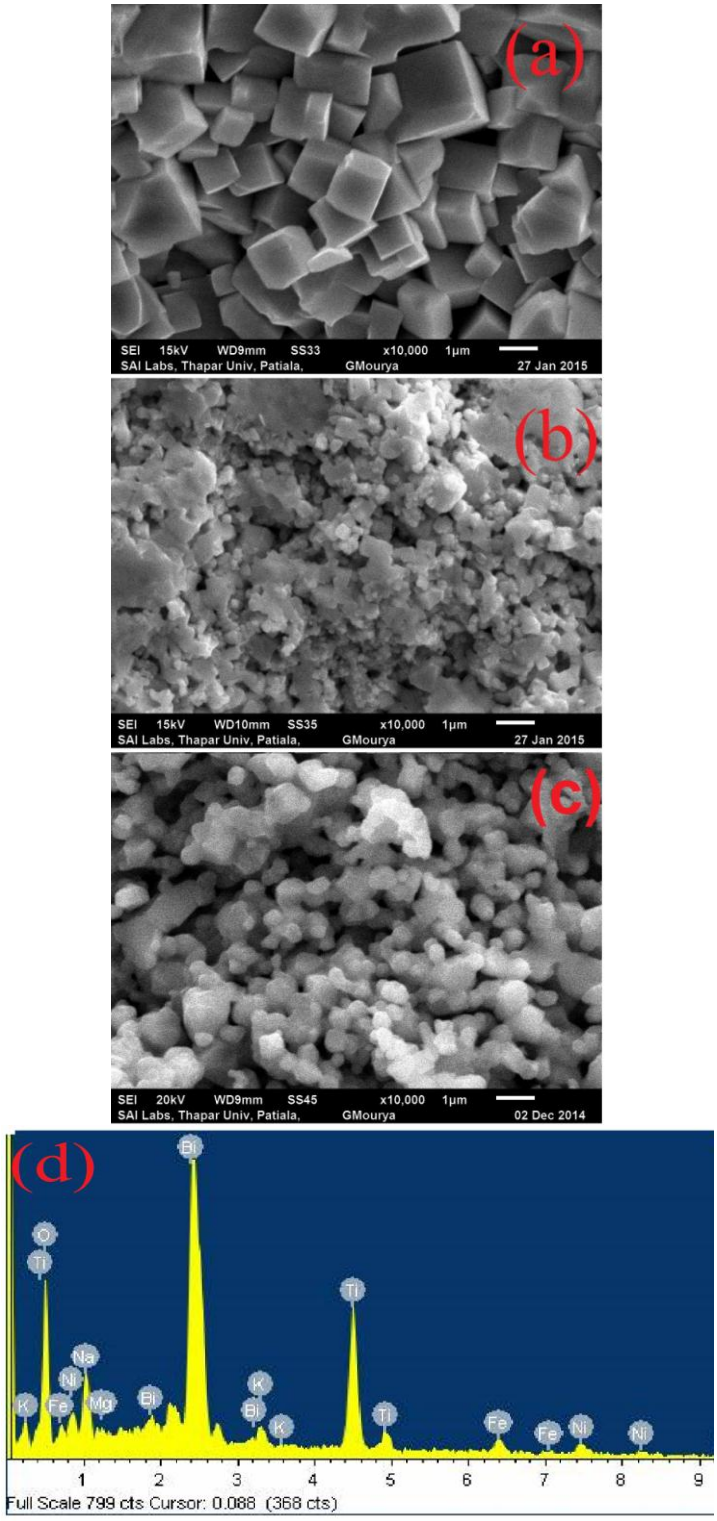

Fig. 4.30. SEM images of (a) 72.5BNT-22.5BKT-5BMgT. (b) (1−*x*)[72.5(BNT) 22.5(BKT)-5(BMgT)] − NFO (*x*=0.2) and (c) NFO (d) EDX spectra of (1−*x*)[72.5(BNT)-22.5(BKT)-5(BMgT)] − NFO (*x*=0.2)

4.5.3 Dielectric properties

Fig. 4.31 (a, b) shows the temperature dependent dielectric behaviour of (1–*x*)[72.5BNT–22.5BKT-5BMgT]–*x* NFO composites where (*x* = 0, 0.1, 0.2, 0.3) measured at 1kHz. The dielectric constant (ε') (fig. 4.31 a) for BNT-BKT-BMgT increases with temperature and then decreases. However, a continuous increase in ε' is observed in composite samples. All samples exhibit two dielectric anomalies at ~ 220 ºC and ~ 320 ºC **[128, 135].** The dielectric anomalies are not visible for *x* = 0.3 against the large background of the ε' with increasing temperature **[37, 128, 135].**

The lower temperature anomaly (T_d ~ 220°C) corresponds to phase transition from ferroelectric to anti-ferroelectric phase and the corresponding temperature is called as depolarization temperature. Peak at ~ 320°C (designated as T_m) corresponds to anti-ferroelectric to paraelectric phase transition **[198].** However, origin of ferroelectric to antiferroelectric transition corresponding to T_d , is under consideration and is only one of the proposed possibility in literature **[39, 135, 198].** The peaks corresponding to T_d in dielectric loss (tan δ) spectra become visibly sharper as compared to ε', shown in the inset of fig. 4.31(b). Moreover, a significant decrease in the peak value of the ε' at T_m can be noticed with increasing the low resistivity NFO content in the composites and totally disappeared in *x* = 0.3 sample, indicating decrease in resistivity of the sample **[199].**

However, particularly at higher temperature for all *x* = 0.1, 0.2, and 0.3 samples, the abrupt increase in ε′ and respective ε″ may due to the increase in conductivity with temperature which may increase the drift mobility of thermally activated charge carriers **[200].** Such kind of behaviour is more prominent in composite with high NFO component (*x* = 0.3). This behaviour can be interpreted through the hopping conduction mechanism of charge carriers between ($Ni^{2+} \leftrightarrow Ni^{3+}$) ions on the octahedral sites and ($Fe^{2+} \leftrightarrow Fe^{3+}$) ions on the tetrahedral sites at high temperature. This electron exchange mechanism between ($Fe^{3+} \leftrightarrow Fe^{2+}$) as well as ($Ni^{2+} \leftrightarrow Ni^{3+}$) causes verwey type electron exchange polarization and therefore enhances the total polarization **[199, 200].**

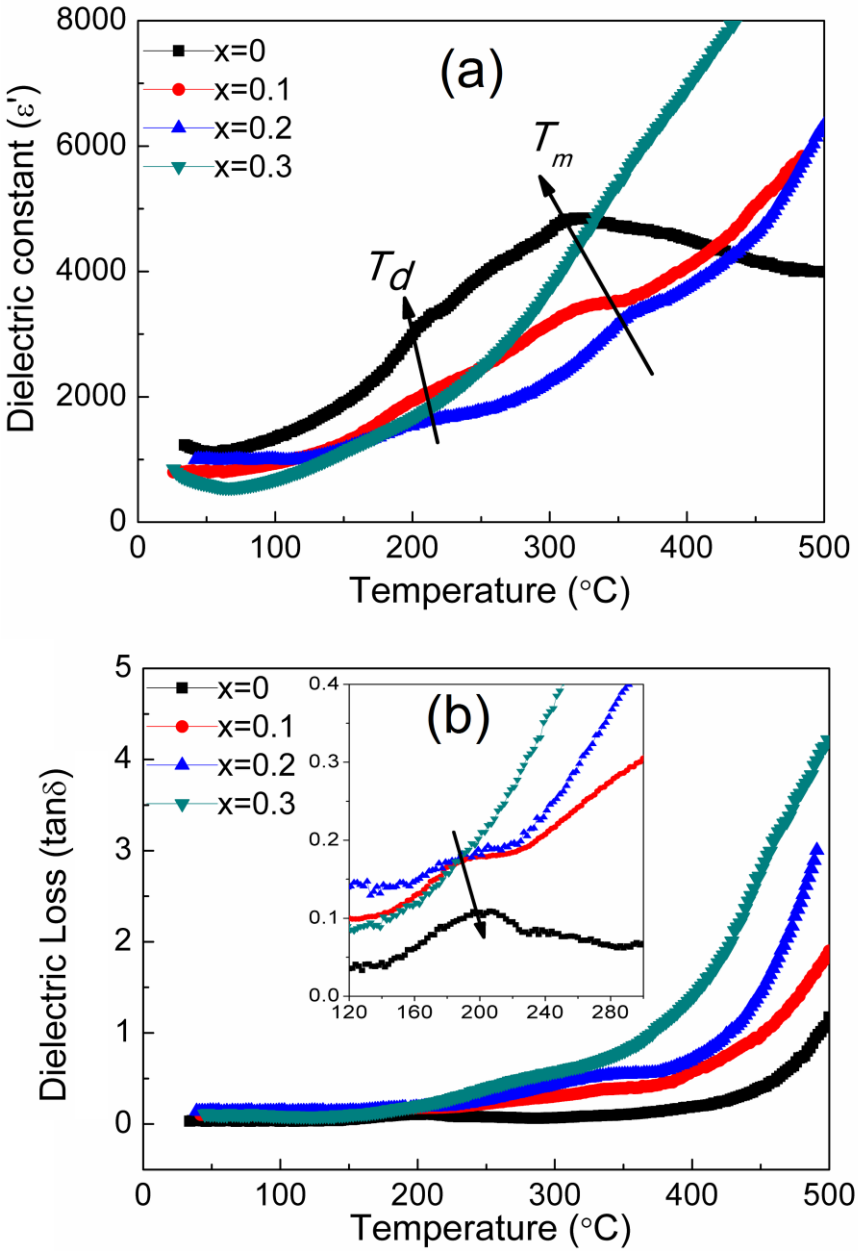

Fig. 4.31. The temperature dependent (a) dielectric constant (ε') and (b) dielectric loss of $(1-x)$[72.5(BNT)-22.5(BKT)-5(BMgT)] − NFO (x = 0.0, 0.1, 0.2, 0.3, 1) *ME* composite at 1kHz frequency.

4.5.4 Ferroelectric properties

Fig. 4. 32 displays the *RT* ferroelectric (*P-E*) loops for all samples, measured at 1 Hz frequency. BNT-BKT-BMgT sample shows well saturated hysteresis loop with large remnant polarization (P_r = 26.2μC/cm^2). The P_r for composite sample decreases continuously with increase in NFO content (inset fig. 4.32) For x = 0.1, 0.2 and 0.3

composite samples, P_r found to be ~ 17.7 μC/cm^2, 14.9 μC/cm^2 and 6.9 μC/cm^2 respectively. Also, the dominant lossy behaviour of x = 0.3 composite sample can be

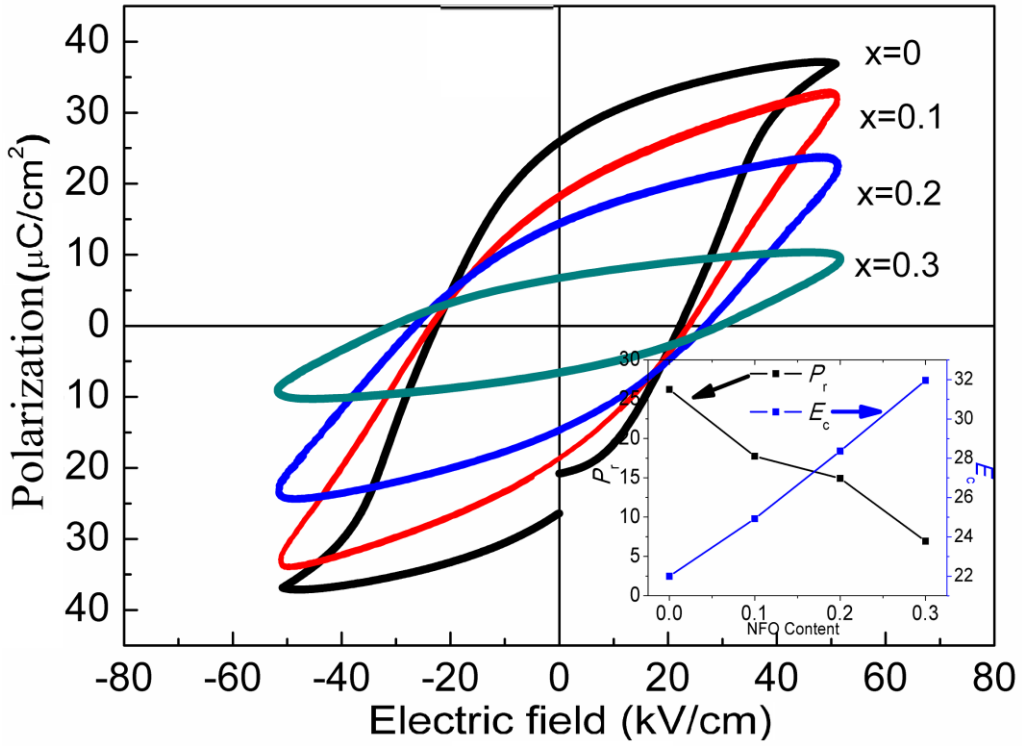

Fig. 4.32. *P-E* loops of (a) (1−*x*)[72.5(BNT)-22.5(BKT)-5(BMgT)] − NFO (*x*=0.0, 0.1, 0.2, 0.3). Inset: variation of P_r and E_c are plotted as a function of increasing NFO content.

attributed to higher content of NFO, which lead to increase in conductivity of composites. Such type of lossy *P-E* loops are often observed in samples with higher conductivity **[186, 199].** The higher tan δ are also observed for x = 0.3 sample (fig. 4. 31 (b)), supporting the higher conductive nature. The E_c of the samples found to increase with NFO content (inset figure 4.32) and is due to the pinning effect of NFO and increased conductivity of the sample.

4.5.5 Magnetic properties

Fig. 4.33 shows the *M-H* loops for all samples with (x = 0.1, 0.2, 1). The well saturated *M-H* loop indicates the ferromagnetic nature of the composite. The saturation magnetization (M_s) and remnant magnetization (M_r) increases with the increase of ferrite

content. The values of M_s and M_r for composites with (x = 0.1, 0.2) were found to be ~ 2.8 emu/g, ~ 5.9 emu/g and ~1 emu/g, 1.9 emu/gm respectively. Thus the ferromagnetic character of the composite sample is sustained even at minimum ferrite content. Also, as shown in zoom view of fig. 4.33, the coercive field is as small as ~ 132 Oe which confirms the soft magnetic nature of the sample.

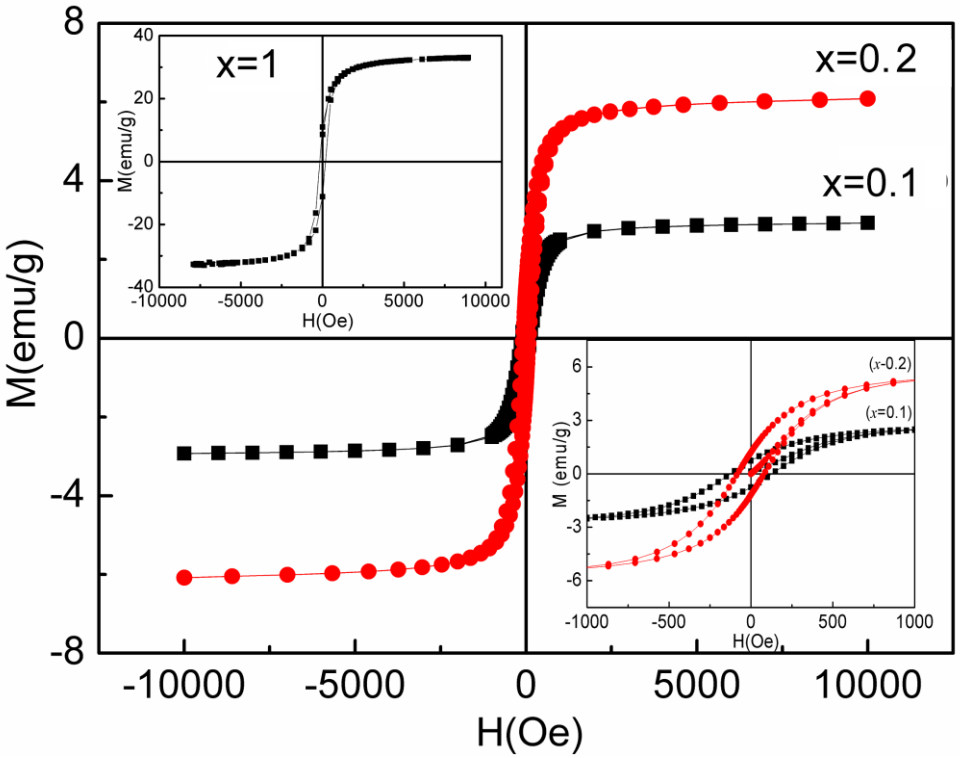

Fig. 4.33. The M-H loop of (1−x)[72.5(BNT)-22.5(BKT)-5(BMgT)] − NFO (x = 0.1, 0.2, 1) and the inset is zoom view of the central part of the figure.

4.5.6 Magnetostriction measurements

Fig. 4.34 (a, b) shows the longitudinal magnetostriction (λ_{11}) as well as their piezomagnetic coupling coefficients (q_{11}= $d\lambda_{11}/dH$) measurements performed on NFO and composite (x = 0.2) upto field of 2500Oe. The saturated λ_{11} values for NFO and composite were ~ -35× 10^{-6} and ~ -18× 10^{-6} at ~ 1000 Oe field respectively. The variation in piezomagnetic coupling coefficients (q_{11}= $d\lambda_{11}/dH$) of NFO and composite with magnetic field is shown in the inset of Fig. 4.34. Initially q_{11} increases with an increase in magnetic field with the maximum value of q_{11} ~ - 0.06×10^{-6} k/Oe for NFO and q_{11} ~ -0.03×10^{-6} k/Oe for composite in the field range (H = 300-400 Oe). The values of q_{11} subsequently decreases with further increase in magnetic field.

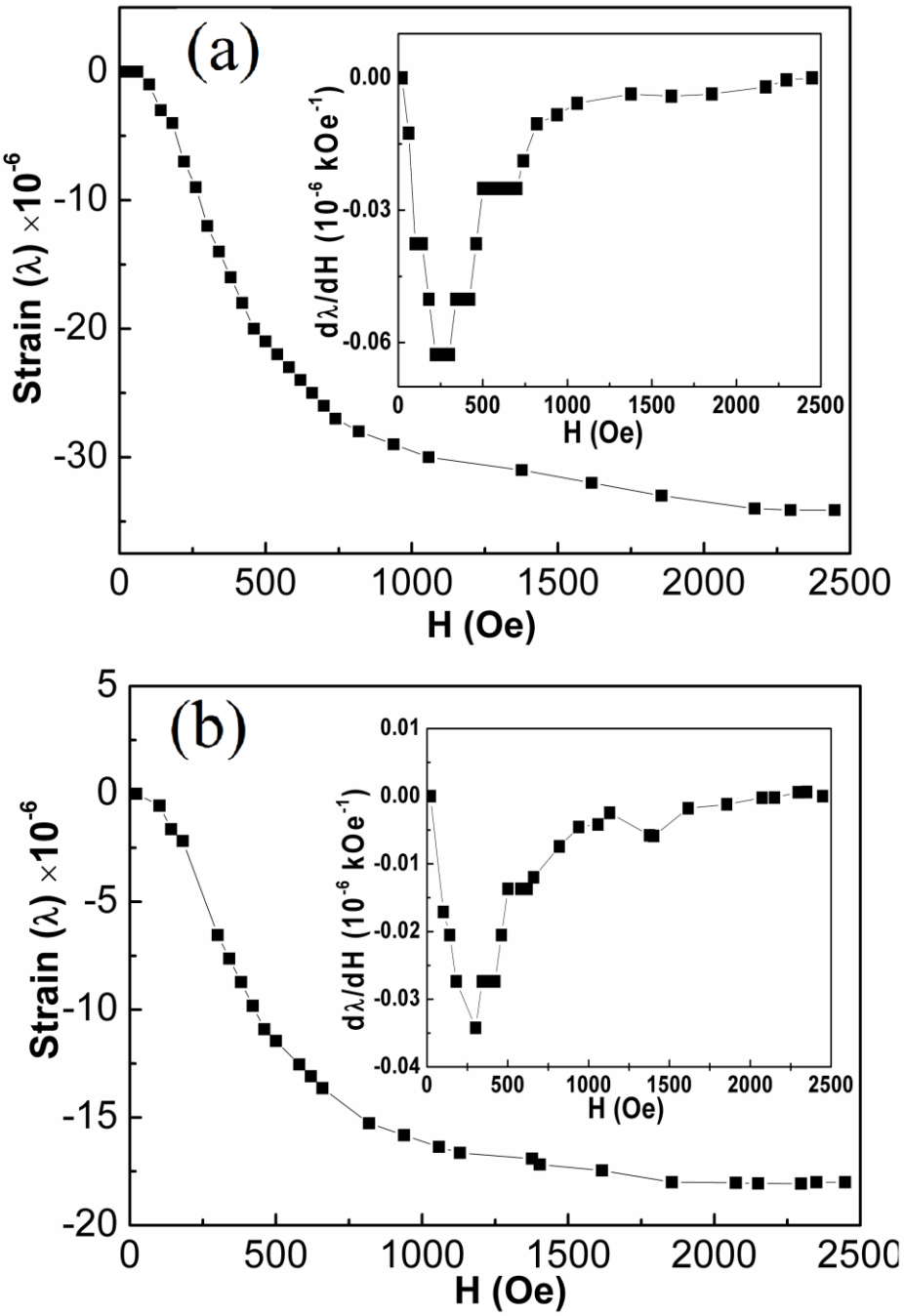

Fig. 4.34. Variation in magnetostriction coefficients λ_{11} with H (a) NFO and (b) $(1-x)$[72.5(BNT)-22.5(BKT)-5(BMgT)] − NFO (x = 0.2) composite. Inset shows variation in piezomagnetic coefficient.

4.5.7 Magnetoelectric measurement

The variation in d_{33} with NFO content is shown in fig. 4.35 (a). The highest d_{33} (145 pC/N) is achieved for x = 0.1 particulate composite and decreases continuously with increasing amount of NFO content. Fig. 4.35 (b) demonstrates the variations of α_E with H for all composite samples.

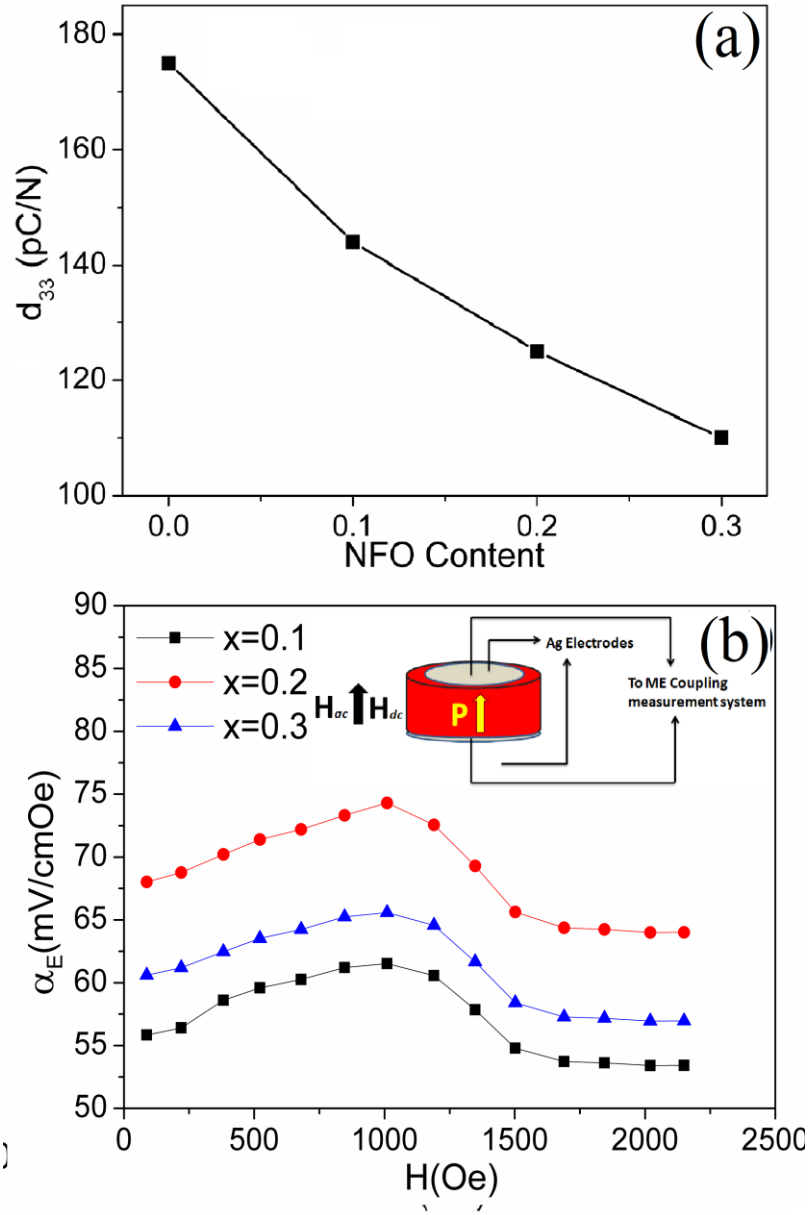

Fig. 4.35. Variation of d_{33} with NFO content and (d) variation of α_E with H of $(1-x)$[72.5(BNT)-22.5(BKT)-5(BMgT)] − NFO (x= 0.1, 0.2, 0.3). Inset shows schematic illustration of particulate composite representing the experimental conditions.

Prior to measurements, all samples were electrically poled along the thickness of the pellet in the field of 4 kV/cm at T = 70 ºC. The induced output voltage (V_{out}) is measured in the direction of electrical poling by applying DC magnetic field under a constant AC magnetic field (H_{AC}) of amplitude ~1 Oe and frequency ~1 kHz. The value of α_E was calculated using the following relation **[201].**

$$\alpha_E = \frac{V_{out}}{tH_{ac}}$$

where, 't' is the thickness of the sample. It can be seen from the fig. 5.7b that α_E initially found to increase with increasing H, attains a peak at ~ 1000 Oe field and decreases with further increase in H. The highest value of α_E (~73.15 mV/cm Oe) was achieved for x = 0.2 composite sample. This sufficiently larger α_E in composites arises due to the large value of d_{33} of piezoelectric component. The lowest value of α_E for x = 0.1 sample is due to the small amount of the NFO phase, which would decrease the ability to elastically respond to magnetostrictions imposed on piezoelectric part by magnetostrictive one. However, comparatively lower α_E with x = 0.3 sample is due to high content of low resistivity of NFO grains, the low resistive grains of NFO provide hindrance to dipole alignment, resulting low α_E values **[200, 202].**

4.6 72.5BNT-22.5BKT-5BMgT]-CFO particulate composite

In previous part of this section we have discussed the structural, dielectric, ferroelectric, magnetic and magnetoelectric properties of 72.5BNT-22.5BKT-5BMgT-NFO particulate *ME* composite and revealed the large value of *ME* coupling (α_E ~73 mV/come). On the same grounds, effect of CFO addition has been studied. The moderate saturation magnetization (M_s ~ 81emu/g), good chemical stability and larger negative saturation magnetostriction coefficient (λ ~ -252× 10^{-6}) suggest it promising candidate for *ME* composites **[203, 204].**

4.6.1 XRD analysis

Fig.4.36 shows typical XRD patterns of BNT-BKT-BMgT, CFO and nanocomposite samples. The XRD of nanocomposite samples can be indexed to two evident sets of well defined peaks, one of which belongs to of BNT-BKT-BMgT and other to CFO.

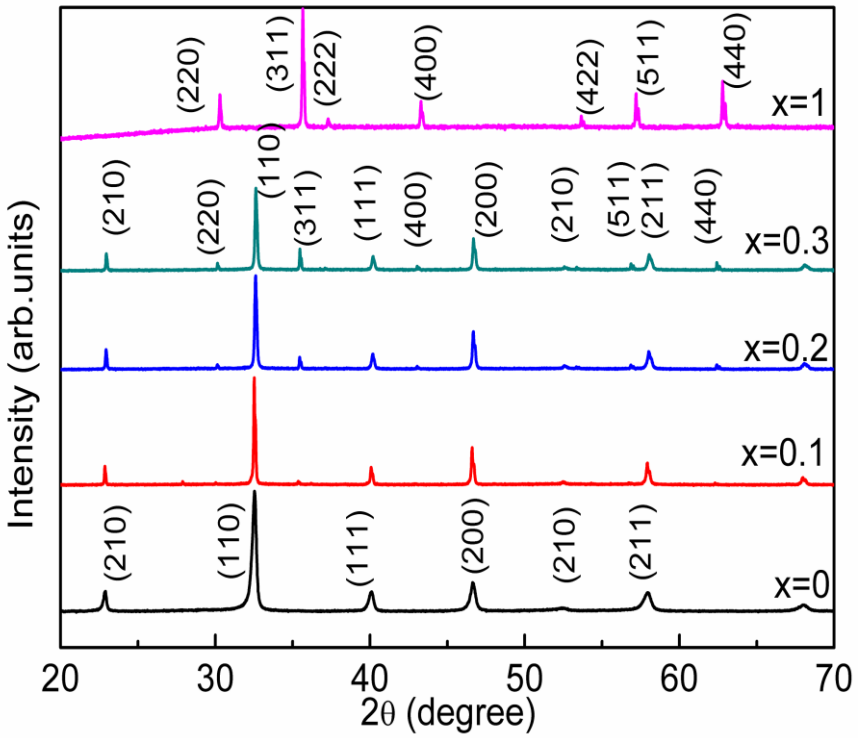

Fig. 4.36. XRD patterns of $(1-x)$[72.5(BNT)-22.5(BKT)-5(BMgT)] − CFO (x = 0.0, 0.1, 0.2, 0.3, 1) *ME* composite.

Intensity of the XRD peaks corresponding to CFO can be clearly seen to increase with the increase in the weight fraction. No additional or intermediate phases were identified, which implies no significant chemical reaction has taken place at the piezoelectric-ferrite interface.

4.6.2 SEM and EDX analysis

Fig.4.37 (a), (b) and (c) shows the SEM micrographs of fracture surface of BNT-BKT-BMgT, CFO and composite with (x=0.2) samples, sintered at 900ºC respectively.

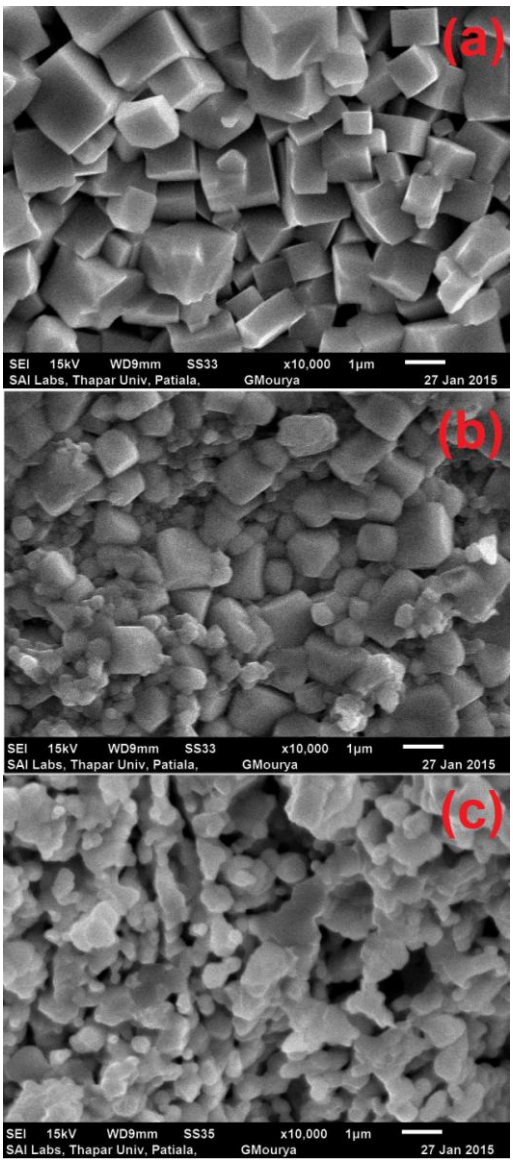

Fig. 4.37. SEM images of (a) 72.5BNT-22.5BKT-5BMgT. (b) (1−*x*)[72.5(BNT)-22.5(BKT)-5(BMgT)] − CFO (*x*=0.2) and (c) CFO.

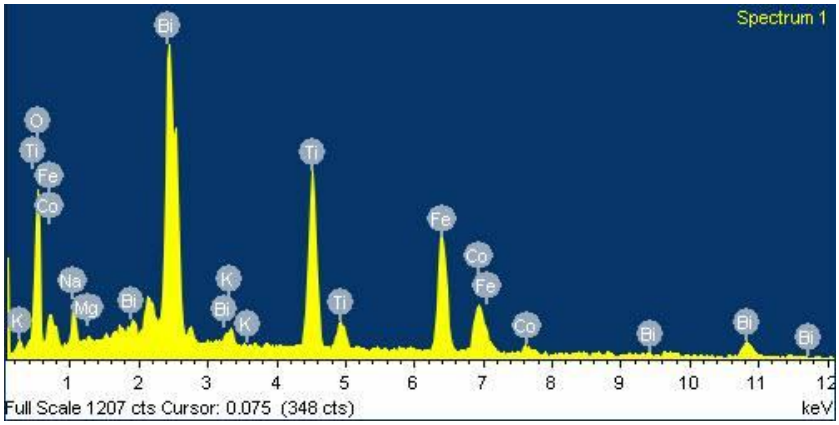

Fig. 4.37. (d) EDX spectra of (1−*x*)[72.5(BNT)-22.5(BKT)-5(BMgT)] − CFO (*x*=0.2)

The average grain size of ~ 1 μm is observed for BNT-BKT-BMgT. However, most of the grains in the CFO micrograph remain with average grain size of 300 nm. The sintering temperature of 900ºC is high enough for the BNT-BKT-BMgT grains to grow but not for the CFO grains, therefore big BNT-BKT-BMgT grains are seen in fracture surface of nanocomposite. The addition of CFO also promotes reduction in the grain size with little porosity as reported earlier **[192].** The reduction in grain size could be the result of pinning action by CFO in the composite **[197].**

4.6.3 Dielectric properties

Fig.4.38 (a, b) shows the temperature dependent dielectric constant along with corresponding dielectric loss tangent (tan δ) for all (1-*x*)[72.5BNT-22.5BKT-5BMgT]–*x*CFO samples measured at fixed frequencies (1kHz ≤ f ≤ 1MHz. The dielectric constant (ε') for BNT-BKT-BMgT increases with temperature and then decreases. All samples in the series exhibit two dielectric anomalies at ~ 220ºC and ~ 320ºC **[128, 135].** The dielectric anomalies are not visible for x = 0.3 against the large background of the ε' with increasing temperature **[37, 128, 135].** The lower temperature anomaly corresponds to phase transition from ferroelectric to anti-ferroelectric phase and the corresponding temperature is called as depolarization temperature (T_d) ~ 220 °C. Peak at ~ 320 °C (designated as T_m) corresponds to anti-ferroelectric to paraelectric phase transition **[198].** However, the peak corresponding to T_d , is under consideration and is only one of the proposed possibility in literature **[39, 135, 198].**

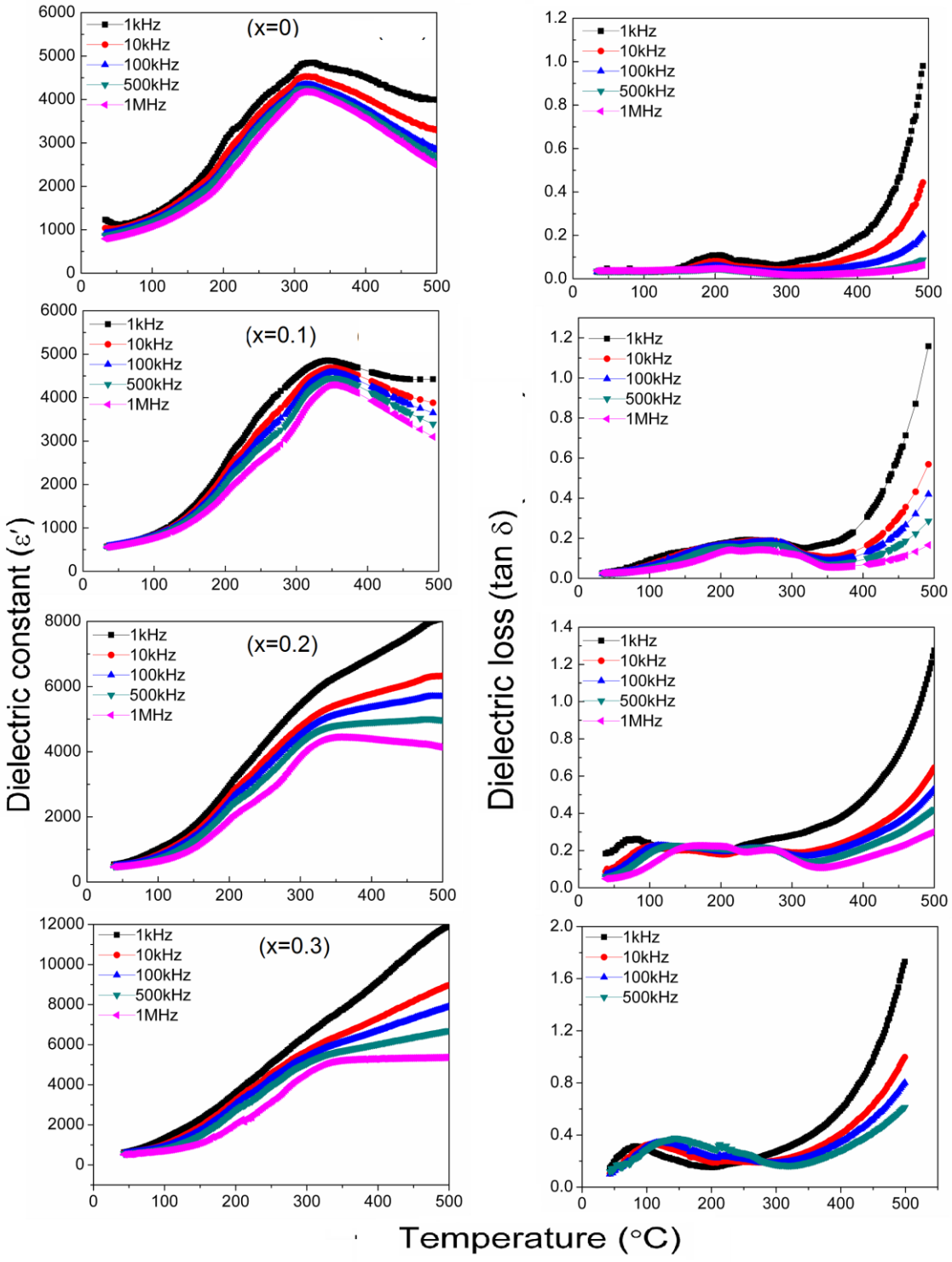

Fig. 4.38. The temperature dependent (a) dielectric constant (ε') and (b) dielectric loss of $(1-x)$[72.5(BNT)-22.5(BKT)-5(BMgT)]−CFO (x=0.0, 0.1, 0.2, 0.3) *ME* composite at 1kHz frequency.

This behaviour is consistent with our study for BNT-NFO based particulate composite. Moreover, a significant increase in ε' at low frequency is due to Maxwell-Wagner type interfacial polarization which plays an important role in composite structures. However, particularly at higher temperature for all x = 0.1, 0.2, and 0.3 samples, the abrupt increase in ε' and respective tan δ may due to the increase in conductivity with temperature which may increase the drift mobility of thermally activated charge carriers **[199, 200].** Such kind of behaviour is more prominent in composite with high CFO content (x = 0.3). This behaviour can be interpreted through the hopping conduction mechanism of charge carriers between ($Co^{2+} \leftrightarrow Co^{3+}$) ions on the octahedral sites and ($Fe^{2+} \leftrightarrow Fe^{3+}$) ions on the tetrahedral sites at high temperature. This electron exchange mechanism between ($Fe^{3+} \leftrightarrow Fe^{2+}$) as well as ($Co^{2+} \leftrightarrow Co^{3+}$) causes verwey type electron exchange polarization and therefore enhances the total polarization **[199, 200].**

4.6.4 Ferroelectric properties

The *RT* ferroelectric (*P-E*) hysteresis loops for all samples measured upto 50 kV/cm are shown in fig.4.39. The well saturated *P-E* loop with large value of remnant polarization (P_r = 26.2μC/cm^2) is observed for BNT-BKT-BMgT sample. The P_r values for composite samples decreases continuously with increase in CFO content. For x = 0.1, 0.2 and 0.3 composite samples, P_r found to be ~ 21.3 μC/cm^2, 15.54 μC/cm^2 and 9.91 μC/cm^2 respectively. Particularly, the round shape *P-E* loop for x = 0.3 composite sample can be attributed to higher content of CFO, which lead to increase in conductivity of composite. Such type of lossy *P-E* loops are also observed in NFO based *ME* composites due to higher conductivity of the samples **[186, 199].** The higher ε'' are also observed for x = 0.3 sample (fig. 4.38 (b)), supporting the higher conductive nature. The E_c of the samples found to increase with CFO content and is due to the pinning effect of CFO.

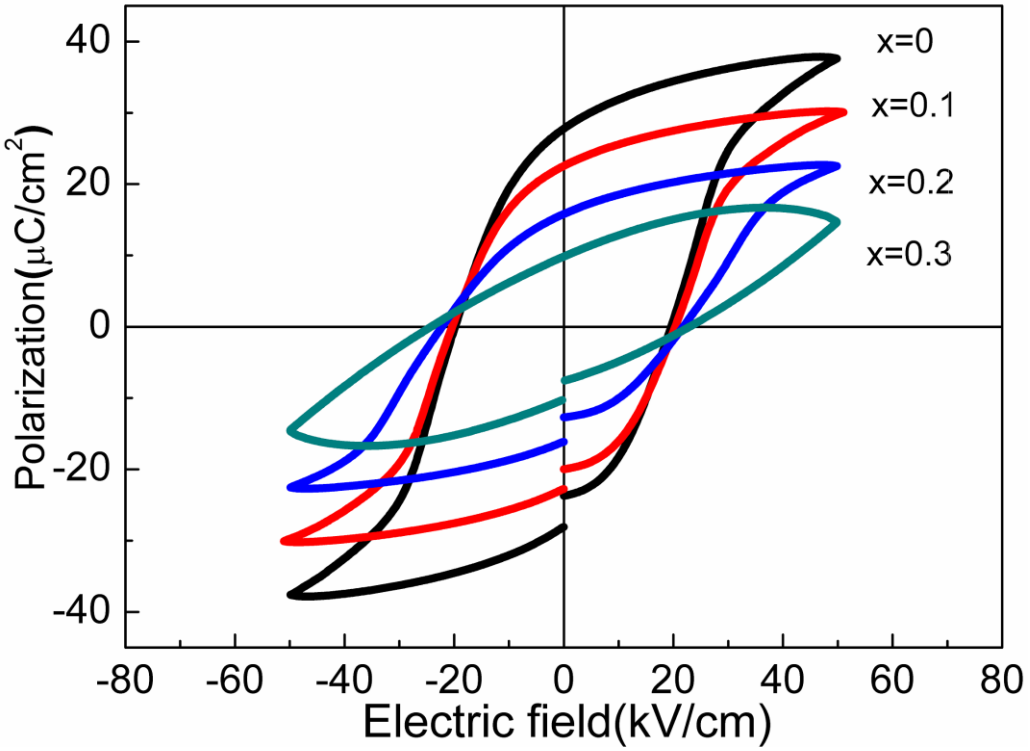

Fig. 4.39. *P-E* loops of (a) (1−*x*)[72.5(BNT)-22.5(BKT)-5(BMgT)] − CFO (*x*=0.0, 0.1, 0.2, 0.3).

4.6.5 Magnetic properties

Fig. 4.40 shows the *M-H* loops for samples with (*x* = 0.1, 0.2 1). The well saturated *M-H* loop indicates the ferromagnetic nature of CFO and the composites. The highest value of saturation magnetization M_s ~ 72 emu/g is observed for pure CFO *x* = 1. As expected, the M_s, remnant magnetization (M_r) and coercivity (H_c) decreases with decrease in CFO content in composites. For minimum CFO content (x = 0.1) the observed values of M_s, M_r and H_c are 16 emu/g, 3emu/g and 370 Oe respectively. Thus the ferromagnetic character of the composite sample is sustained even at minimum ferrite content.

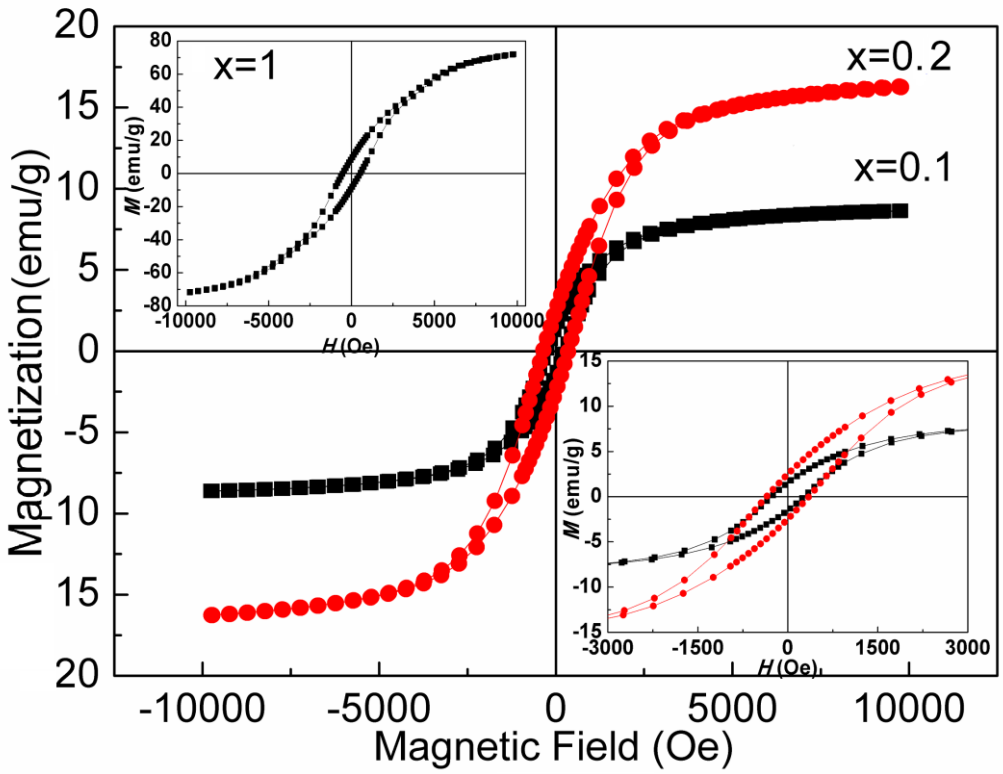

Fig. 4. 40 The *M-H* loop of (1−*x*)[72.5(BNT)-22.5(BKT)-5(BMgT)] − CFO (x=0.1, 0.2, 1) and the inset (left) is zoom view of the central part of the figure.

4.6.6 Magnetoelectric measurement

Fig. 4.41 demonstrates the variations of α_E with H for all composite samples. Prior to measurements, all samples were electrically poled along the thickness of the pellet in the field of 4 kV/cm at T = 70ºC. The induced output voltage (V_{out}) is measured in the direction of electrical poling by applying DC magnetic field under a constant AC magnetic field (H_{AC}) of amplitude ~1 Oe and frequency ~1 kHz. The value of α_E was calculated using the relation as discussed in previous part of this section **[201].** It can be observed from the fig. 4.41 that α_E initially found to increase with increasing H, attains a peak at ~ 5000 Oe field and decreases with further increase in H. The highest value of α_E (~112 mV/cm Oe) was achieved for x = 0.2 composite sample. This sufficiently larger α_E in composites arises due to the large value of d_{33} of piezoelectric component. The lowest value of α_E in our series observed for x = 0.1 sample is due to the small amount of the CFO content, which would decrease the ability to elastically respond to

magnetostrictions imposed on piezoelectric part by magnetostrictive one. However, comparatively lower α_E with x = 0.3 sample is due to high content of low resistivity of CFO grains, the low resistive grains of ferrites provide hindrance to dipole alignment, resulting low α_E values **[200, 202].**

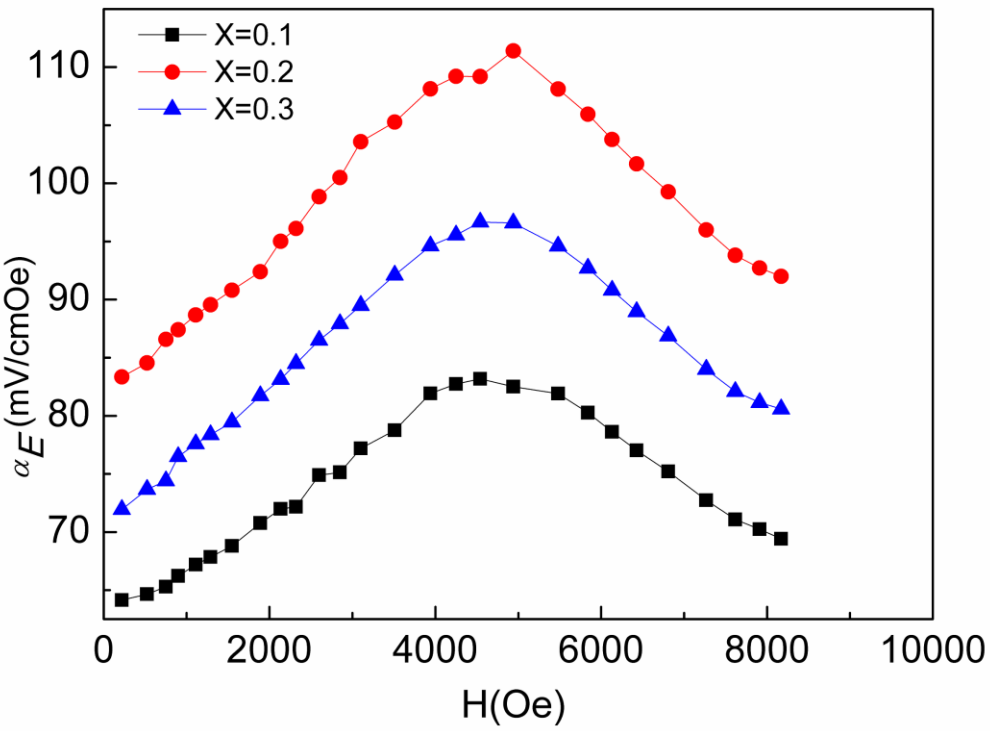

Fig. 4.41 variation of α_E with H of (1−x) [72.5(BNT)-22.5(BKT)-5(BMgT)] − CFO (x = 0.1, 0.2, 0.3).

CHAPTER V
CONCLUSIONS AND FUTURE WORK

This chapter summarizes the major conclusions/findings of the present study and scope of the future work on non lead Bi based multiferroic composites.

Summary of work done in the present thesis is given below.

Studies on $BiFeO_3$ (BFO) thin films

The BFO thin films were synthesized by the sol-gel method and deposited by spin-coating technique. The XRD pattern shows that the as deposited films are amorphous in nature. BFO thin films annealed at 500ºC and above were polycrystalline in nature with no secondary phases. The BFO thin films demonstrate good ferroelectric behaviour. However, the ferroelectric properties are found to decrease with increasing grain size. Dielectric behaviour is also greatly affected by the grain size. The grain growth, improved crystallinity and higher density of the films as observed by XRD patterns and AFM images may be the reason for increased dielectric constant. The anomaly in temperature dependent dielectric permittivity of nanoscale BFO exhibit characteristic features of magnetic transition point. These features establish the formation of a true ferromagnetic-ferroelectric system with a coupling between the respective order parameters.

Studies on $BiFeO_3$ (BFO)-$CoFe_2O_4$ (CFO) composite thin films

The Multiferroic (1-*x*)BFO-CFO (*x* = 0, 0.1, 0.2, 0.3) nanocomposite thin films, were prepared by sol-gel spin-coating method followed by annealing at 600 ºC and 650 ºC respectively. The addition of CFO in BFO matrix shows a strong effect on their structural, dielectric, magnetic and ferroelectric properties. The coexistence of ferroelectric and ferromagnetic ordering at room temperature is confirm by *P-E* and *M-H* measurements. It is found that the relative concentration of *x* in composites strongly modified the dielectric, ferroelectric and magnetic properties of BFO/CFO nanocomposite thin films. Additionally, the annealing temperature also effect the multiferroic properties for composite thin films. The magnetic behviour is improved for all composite films annealed at high temperature. For *x* = 0.3, M_s is found as high as ~ 115 emu/cm^3 and 158 emu/cm^3 for the films annealed at 600 ºC and 650 ºC respectively. However, values of P_r is decreased resulting lossy ferroelectric

behaviour are observed for all (1-*x*) BFO-CFO (*x* = 0, 0.1, 0.2, 0.3) nanocomposite thin films at higher temperature 650 °C. The bismuth loss at higher temperature is responsible for lossy ferroelectric behaviour for all the samples.

Studies on (1-*x*)$BiFeO_3$(BFO)–*x*$NiFe_2O_4$(NFO) composite thin films

Multiferroic (1-*x*) BFO–*x* NFO (*x* = 0, 0.1, 0.2, 0.3) nanocomposite thin films are prepared via sol-gel method. The magnetic and electric behaviour are shown to depend on volume ratio of NFO nanopaticle. The nanocomposite structures were found to exhibit both ferroelectric as well as ferromagnetic behaviour at room temperature. The BFO/NFO thin films demonstrates improved dielectric and magnetic behaviour. The saturation magnetization and remnant magnetization increased as high as ~34 emu/cm^3 and ~7 emu/cm^3 respectively for *x* = 0.1. The dielectric constant of the films increased from 160 (for *x* = 0) to 280 (for *x* = 0.3). However**,** the values of remnant polarization and saturation polarization were decreased with increasing *x* as expected.

Studies on BNT-BKT-BMgT/NFO Particulate composite

Lead free *ME* particulate composites (1−*x*)[72.5(BNT)-22.5(BKT)-5(BMgT)] −*x* NFO (*x* = 0, 0.1, 0.2, 0.3) are prepared without any impurity phase using sol-gel method. XRD and EDXs examinations confirm the co-existence of both phases. The modified BNT-BKT-BMgT showed the piezoelectric coefficient (d_{33}) values of 180 pC/N. The α_E of the composite series found to be strongly dependent on NFO content. Large *ME* voltage coefficient (α_E) ~73 mV/cmOe accompanied by high d_{33} ~125 pC/N and magnetostrictive strains (λ_{11}) ~ -18× 10^{-6} were obtained for *x* = 0.2 composite. The *ME* composite exhibit *P-E* loops and well saturated *M-H* loop, shows that ferroelectric and magnetic properties are well sustained in the composite samples. The temperature dependent dielectrics behavior shows two anomalies at ~220 ºC and ~320 ºC corresponds to phase transition from ferroelectric to anti-ferroelectric and to anti-ferroelectric to paraelectric respectively. The present study demonstrate a new environmental-friendly *ME* particulate composite for future applications.

Studies on BNT-BKT-BMgT/CFO Particulate composite

Lead free *ME* particulate composites (1−*x*)[72.5(BNT)-22.5(BKT)-5(BMgT)] −*x* CFO (*x* = 0, 0.1, 0.2, 0.3) are prepared without any impurity phase using sol-gel method. XRD and EDXs

examinations confirm the co-existence of both phases. The α_E of the composite series found to be strongly dependent on CFO content. Large α_E ~112 mV/cmOe accompanied by high d_{33} ~130 pC/N. The *ME* composite exhibit *P-E* loops and well saturated *M-H* loop, shows that ferroelectric and magnetic properties are well sustained in the composite samples. The temperature dependent dielectrics behavior shows two anomalies at ~220 ºC and ~320 ºC corresponds to phase transition from ferroelectric to anti-ferroelectric and to anti-ferroelectric to paraelectric respectively. Summarized properties obtained for different series are shown in Table 5.1.

Table 5.1. Summarized properties obtained for different series

System	Composition	~ ε'	~ P_r μC/cm^2	~ M_s emu/cm^3	α_E (mV/cmOe)
BFO at different temperature	500°C	183	25	-----	-----
	550°C	200	23	-----	-----
	600°C	212	20	-----	-----
BFO/CFO (600°C)	x = 0.1	260	16	41	-----
	x = 0.2	287	14	78	-----
	x = 0.3	337	9	115	-----
BFO/CFO (650°C)	x = 0.1	247	12	60	-----
	x = 0.2	268	11	106	-----
	x = 0.3	315	9	158	-----
BFO/NFO (600°C)	x = 0.1	201	9	34	-----
	x = 0.2	234	6	-----	-----
	x = 0.3	280	4	-----	-----
				~ M_s emu/g	
BNT-BKT-BMgT/NFO	x = 0.1	-----	19	3	61
	x = 0.2	3500	13	6	73
	x = 0.3	-----	7	-----	65
BNT-BKT-BMgT/CFO	x = 0.1	-----	23	8	84
	x = 0.2	5000	16	16	112

	$x = 0.3$	-----	9	-----	92

FUTURE SCOPE

On the basis of work done in the present thesis few points and directions are addressed for future work in the area of multiferroc composites.

- Two phase bilayer multiferroic nanocomposite thin films having alternating layer of ferroelectric BFO and ferrite NFO/CFO can be prepared and studied. Other combinations of piezoelectric/ferroelectric perovskites and ferrites can be selected for preparation of Multiferroic composites and further studied.
- Bulk laminate *ME* composites consisting of piezoelectric **BNT-BKT-BMgT** and magnetostrictive CFO, NFO phases can be synthesized and studied.
- Two phase particulate *ME* nanocomposite thin films by distributing ferrite particles in piezoelectric **BNT-BKT-BMgT** matrix can be prepared and studied.
- Multilayer *ME* nanocomposite thin films consisting alternating layers of **BNT-BKT-BMgT** CFO/NFO can be prepared and studied.

REFERENCES

[1]. W. Eerenstein, N. D. Mathur, and J. F. Scott, Nature London **442**, 759–765 (2006).

[2]. R. Ramesh and N. A. Spaldin, Nature Mater **6**, 21–29 (2007).

[3]. J. F. Scott and C. A. Paz De Araujo, Science **246**, 4936 (1989).

[4]. J. F. Scott, Nature Materials **6**, 256–257 (2007).

[5]. G. A. Prinz, Science **282**, 1660–1663 (1998).

[6]. C. Chappert, A. Fert, and F. N. Van Dau, Nature Materials **6**, 813–823 (2007).

[7]. Chaoyong Deng, Yi Zhang, Jing Ma, Yuanhua Lin, Ce-Wen Nan, Acta Materialia **56** 405–412 (2008)

[8]. R.Y. Zheng, J. Wang, S. Ramakrishna J. Appl. Phys. **104**, 034106 (2008).

[9]. C. Deng, Y. Zhang, J. Ma, Y. Lin, and C. W. Nan, J. App. Phys. **102**, 074114 (2007).

[10]. H. C. He, J. P. Zhou, J. Wang, and C. W. Nan, Appl. Phys. Lett. **89**, 052904 (2006).

[11]. H. Ryu, P. Murugavel, J. H. Lee, Appl. Phys. Lett. **89**, 102907 (2006).

[12]. Y. G. Ma, W. N. Cheng, M. Ning, and C. K. Ong, Appl. Phys. Lett. **90**, 152911 (2007).

[13]. S. Q. Ren, L. Q. Weng, S. H. Song, F. Li, J. G. Wan, and M. Zeng, J. Matter. Sci. **40**, 4375–4378 (2005).

[14]. F. Yang, Y. C. Zhou, M. H. Tang, J. Phys. D **42**, 072004 (2009).

[15]. L. D. Landue and E. Lifshitz, Electrodynamics of Continuous Media, Addison-Wesley, Reading, Mass, USA (1960).

[16]. G. Catalan, J. F. Scott, Adv. Matter. **21**, 2463-2485 (2009)

[17]. D. Pantel *et al*., J. Appl. Phys. **107,** 084111 (2010).

[18]. I. O. Troyanchuk *et a.l*, J. Phys. Condens. Matter, **8,** 11205–12 (2010).

[19]. T. Kimura *et al*., Phys. Rev. B **67,** 180401(2003).

[20]. T. Zhao *et al*., Nature Mater. Vol. **5**, 823 (2006).

[21]. Zavaliche, *et al.*, Appl. Phys. Lett. **87**, 252902 (2005).

[22]. T. Kimura *et al*, Phys. Rev. B **71,** 224425 (2005).

[23]. D. Rubi *et al*., Phys. Rev. B **79,** 014416 (2009).

[24]. B. J. Kirby *et al*, J. Appl. Phys. **105,** 07D917 (2009).

[25]. X. Marti *et al*, Appl. Phys. Lett. **96,** 222505 (2010).

[26]. R.Y. Zheng, X. S. Gao, Z. H. Zhou, and J. Wang, J. Appl. Phys. **101**, 054104–054104 (2007).

[27]. J. Wang, J. B. Neaton, H. Zheng, V. Nagarajan, S. B. Ogale, B. Liu, D. Viehland, V. Vaithyanathan, D. G. Schlom, U. V. Waghmare, N. A. Spaldin, K. M. Rabe, M. Wuttig, and R. Ramesh, **299**, 1719–1722 (2003).

[28]. S. Y. Yang, F. Zavaliche, L. Mohaddes-Ardabili, V. Vaithyanathan, D. G. Schlom, Y. J. Lee, Y. H. Chu, M. P. Cruz, Q. Zhan, T. Zhao, and R. Ramesh, Appl. Phys. Lett. **87**, 102903 (2005).

[29]. H. Naganuma,Y. Inoue, and S. Okamura, IEEE Trans. Ultrason. Ferroelect. Freq. Contr. **55**, 1046–1050 (2008).

[30]. C. Ederer and N. A. Spaldin, Phys. Rev. B, **71**, 060401 (2005).

[31]. L. Yan, Z. Xing, Z. Wang, T. Wang, G. Lei, J. Li, and D. Viehland, Appl. Phys. Lett. **94**, 192902 (2009).

[32]. L. Yan, Z. Wang, Z. Xing, J. Li, and D. Viehland, J. Appl. Phys. **107**, 064106 (2010).

[33]. Y. S. Oh, S. Crane, H. Zheng, Y. H. Chu, R. Ramesh, and K. H. Kim, Appl. Phys. Lett. **97**, 052902 (2010).

[34]. K. Sone, S. Sekiguchi, H. Naganuma, T. Miyazaki, and T. Nakajima, J. Appl. Phys., **111**, 124101-1–124101-5 (2012).

[35]. H. Zheng, J. Wang, S. E. Lofland, Z. Ma, L. M. Ardabili, T. Zhao, L. S. Riba, S. R. Shinde, S. B. Ogale, F. Bai, D. Viehland, Y. Jia, D. G. Schlom, M. Wuttig, A. Roytburd, and R. Ramesh, Science, **303**, 661–663 (2004).

[36]. R. Guo, L. E.Cross, S. E. Park, B. Noheda, D. E. Cox, and G. Shirane, Phys. Rev. Lett. **84**, 5423 (2000).

[37]. T. Takenaka, K. Maruyama and K. Sakata, J. App. Phys. **30**, 2236-2239 (1991).

[38]. T. Takenaka, H. Nagata, Y. Hiruma, Ferroelectric Ceram, **56**, 1595 (2009).

[39]. J. Hao, B. Shen, J. Zhai, C. Liu, X. Li, X. Gao, J. Appl. Phys.**, 113,** 114106 (2013).

[40]. X. X. Wang, S. H. Choy, X. G. Tang, H. L. W. Chan, J. Appl. Phys. **97**, 104101 (2005).

[41]. P. Jarupoom, E. Patterson, B. Gibbons, G. Rujijanagul, Yimnirun and G. Cann, App. Phys. Lett. **99**, 152901 (2011).

[42]. Amrita Singh and Ratnamala Chatterjee J. Appl. Phys. **109**, 024105 (2011)

[43]. S. Narendra Babu, Leszek Malkinski, J. Appl. Phys. **111**, 07D919 (2012).

[44]. Arti Gupta, A. Huang, Santiranjan Shannigrahi, Ratnamala Chatterjee, App. Phys. Lett. **98**, 112901 (2011).

[45]. Arti Gupta, Ratnamala Chatterjee J. Europ. Ceram. Soc. **33** 1017 (2013).

[46]. J. van den Boomgard and R. A. Born, J. Mat. Sci. **13**, 1538 (1978).

[47]. R. C. Kambale, P. A. Shaikh, C. H. Bhosale, K. Y. Rajpure, and Y. D. Kolekar, J. Alloy Compd., **489**, 310–315 (2010).

[48]. Dong Hun Kim, Nikolas M. Aimon, Xueyin Sun and Caroline A. Ross, Adv. Funct. Mater., 2334-2342 (2014)

[49]. S. S. Chougule and B. K. Chougule, Smart. Mater. Struct. **16**, 493–497, (2007).

[50]. B. S. Narendra, J. H. Hsu, Y. S. Chen, J. G. Lin, J. Appl. Phys. **109,** 07D904 (2011).

[51]. A. Srinivas, R. V. Krishnaiah, T. Karthik, Suresh, S. Asthana, S. V. Kamat, App. Phys. Lett. **101,** 082902 (2012).

[52]. P. Curie, J. Phys-Paris, 3e Serie, **3**, 393 (1894).

[53]. I. E. Dzyaloshinskii, Sov Phys. JETP, **37**, 628–629 (1960).

[54]. D. N. Astrov, Sov. Phys. JETP, **11**, 708–709 (1960).

[55]. D. L. Fox and J. F. Scott, J. Phys. C: Sol. State Phys. **10,** L329–331 (1977).

[56]. R. E. Newnham et al., J. Appl. Phys. **49,** 6088–91 (1978).

[57]. J. R. Teague, R. Gerson and W. J. James, Solid State Commun. **8,** 1073–4 (1970).

[58]. E. F. Bertaut and M. Mercier, Mater. Res. Bull. **6,** 907–21(1971).

[59]. T. Kimura et al., Nature, **425**, 55–8 (2003).

[60]. M. Fiebig et al., Nature,**419**, 818–20 (2002).

[61]. (a) G. A. Smolenskii, I. E. Chupis, Usp. Fiz. Nauk, **137**, 415 (1982). (b) G. A. Smolenskii, I. E. Chupis, Sov. Phys. Usp., **25**, 475 (1982). c) G. A. Smolenskii, I. E. Chupis, Sov. Phys. Solid State, **4**, 807 (1962). (c) J. R. Chen, W. L. Wang, J. B. Li, G. H. Rao, J. Alloys Compd. **459**, 66 (2008).

[62]. J. R. Chen, W. L. Wang, J. B. Li, G. H. Rao, J. Alloys Compd., **459**, 66 (2008).

[63]. Z. V. Gabbasova, M. D. Kuzmin, A. K. Zvezdin, I. S. Dubenko, V. A. Murashov, D. N. Rakov, I. B. Krynetsky, Phys. Lett. A, **l58**, 491 (1991).

[64]. A. V. Zalesskii, A. A. Frolov, T. A. Khimich, A. A. Bush, Phys. Solid. State., **45**, 141 (2003).

[65]. G. L. Yuan, S. W. Or, H. L. W. Chan, J. Phys. D: Appl. Phys., **40**, 1196 (2007).

[66]. a) D. Lebeugle, D. Colson, A. Forget, M. Viret, P. Bonville, J. F. Marucco, S. Fusil, Phys. Rev. B, **76**, 024 116 (2007). b) D. Lebeugle, D. Colson, A. Forget, M. Viret, P. Bonville, J. F. Marucco, S. Fusil, Appl. Phys. Lett., **91**, 022907 (2007).

[67]. Kwi Young Yun, Minoru Noda, and Masanori Okuyama, Appl. Phys. Lett., **83**, 3981 (2003).

[68]. Kwi Young Yun, Minoru Noda, Masanori Okuyama, Hiromasa Saeki, Hitoshi Tabata, and Keisuke Saito, J. Appl. Phys. **96**, 3399 (2004).

[69]. N. M. Murari, R. Thomas, R. E. Melgarejo, S. P. Pavunny, and R. S. Katiyar, J. Appl. Phys. **106**, 014103 (2009).

[70]. J. M. Park, S. Nakashima, F. Gotoda, T. Kanashima, and M. Okuyama, Jpn. J. Appl. Phys. **48**, 09KB03 (2009).

[71]. J. Wu and J. Wang, J. Am. Ceram. Soc. **93**, 2795 (2010). J. Wu and J. Wang, J. Appl. Phys. **106**, 054115 (2009).

[72]. S. K. Singh, H. Ishiwara, K. Sato, and K. Maruyama, J. Appl. Phys. 102, 094109 (2007).

[73]. F. Z. Huang, X. M. Lu, W. W. Lin, X. M. Wu, Y. Kan, and J. S. Zhu, Appl. Phys. Lett. **89**, 242914 (2006)

[74]. G. D. Hu, X. Cheng, W. B. Wu, and C. H. Yang, Appl. Phys. Lett. **91**, 232909 (2007).

[75]. Z. Quan, W. Liu, H. Hu, S. Xu, B. Sebo, G. Fang, M. Li, and X. Zhao, J. Appl. Phys. **104**, 084106 (2008).

[76]. X. Wang, H. Liu, and B. Yan, J. Euro. Ceram. Soc. **29**, 1183 (2009).

[77]. G. L. Yuan, Siu Wing Or, and Helen Lai Wa Chan J. Appl. Phys. **101**, 064101 (2007)

[78]. J. Van Suchtelen, Philips Research Report, **27**, 28–37 (1972).

[79]. J. Van den Boomgaard, A. M. J. G. van Run, and J. van Suchtelen, Ferroelectrics, **10**, 295–298 (1976).

[80]. J. V. D. Boomgaard, D. R. Terrell, R. A. J. Born, and H. F. J. I. Giller, J. Mater. Sci., **9**, 1705–1709 (1974).

[81]. A. M. J. G. Run , D. R. Terrell, J. H. Scholing , J. Mater. Sci., **9**, 1710 (1974).

[82]. J. H. Ryu , S. Priya , A. V. Carazo , K. Uchino , H. E. Kim , J. Am. Ceram. Soc., **84**, 2905 (2001).

[83]. J. Ryu, A. V. Carazo, K. Uchino, and H. E. Kim, J. Electroceram.,**7**, 17–24 (2001).

[84]. S. X. Dong, J. R. Cheng, J. F. Li, D. Viehland, Appl. Phys. Lett., **83**, 4812 (2003).

[85]. C. W. Nan, L. Liu, N. Cai, J. Zhai, Y. Ye, Y. H. Lin, L. J. Dong, and C. X. Xiong, Appl. Phys. Lett. **81**, 3831 (2002).

[86]. J. G. Wan, J. M. Liu, H. L. W. Chand, C. L. Choy, G. H. Wang, and C. W. Nan, J. Appl. Phys. **93**, 9916 (2003).

[87]. C. W. Nan, N. Cai, L. Liu, J. Zhai, Y. Ye, and Y. H. Lin, J. Appl. Phys. **94**, 5930 (2003).

[88]. N. Cai, J. Zhai, C. W. Nan, Y. H. Lin, and Z. Shi, Phys. Rev. B **68**, 224103 (2003).

[89]. N. Cai, C. W. Nan, J. Y. Zhai, and Y. H. Lin, Appl. Phys. Lett. **84**, 3516 (2004).

[90]. Y. H. Lin, N. Cai, J. Y. Zhai, G. Liu, and C. W. Nan, Phys. Rev. B **72**, 012405 (2005).

[91]. T. G. Lupeiko, I. V. Lisnevskaya, M. D. Chkheidze, and B. I. Zvyagintsev, Inorg. Mater. **31**, 1245 (1995).

[92]. M. I. Bichurin, I. A. Kornev, V. M. Petrov, and I. Lisnevskaya, Ferroelectr. **204**, 289 (1997).

[93]. J. Ryu, A. V. Carazo, K. Uchino, and H. E. Kim, J. Electroceram. **7**, 17 (2001).

[94]. J. Y. Zhai, N. Cai, Z. Shi, Y. H. Lin, and C. W. Nan, J. Phys. D **37**, 823 (2004).

[95]. J. Y. Zhai, N. Cai, Z. Shi, Y. H. Lin, and C. W. Nan, J. Appl. Phys. **95**, 5685 (2004).

[96]. X. M. Chen, Y. H. Tang, and I. W. Chen, J. Appl. Phys. **96**, 6520 (2004).

[97]. G Sreenivasulu, V. Hari Babu, G. Markandeyulu, B. .S Murty App. Phys. Lett. **94** 112902 (2009)

[98]. V. M. Petrov, G. Srinivasan, V. Laletsin, and M. I. Bichurin, Phys. Rev. B **75**, 174442 (2007).

[99]. Arti Gupta, Ratnamala Chatterjee J. Magn. Magn. Mater. **322** 1020-1025 (2010).

[100]. J. G. Wan, H. Zhang, and X. W. Wang, Appl. Phys. Lett. **89**, 122914 (2006).

[101]. G. Srinivasan, C. P. DeVreugd, and C. S. Flattery, Appl. Phys. Lett. **85**, 2550 (2004).

[102]. Q. H. Jiang, Z. J. Shen, J. P. Zhou, Z. Shi, and C. W. Nan, J. Eur. Ceram. Soc. **27**, 279 (2007).

[103]. G. Srinivasan, E. T. Rasmussen, J. Gallegos, R. Srinivasan, Y. I. Bokhan, and V. M. Laletin, Phys. Rev. B **64**, 214408 (2001).

[104]. G. Srinivasan, E. T. Rasmussen, B. J. Levin, and R. Hayes, Phys. Rev. B **65**, 134402 (2002).

[105]. G. Srinivasan, R. Hayes, and M. I. Bichurin, Solid State Commun. **128**, 261 (2003).

[106]. G. E. Srinivasan, T. Rasmussen, and R. Hayes, Phys. Rev. B **67**, 014418 (2003).

[107]. J. P. Zhou, H. C. He, Z. Shi, G. Liu, and C. W. Nan, J. Appl. Phys. **100**, 094106 (2006).

[108]. I. V. Lisnevskaya, I. A. Bobrova, and E. A. Bikyashev, Inorg. Mater. **42**, 1147 (2006).

[109]. H. Zheng, J. Wang, L. Mohaddes-Ardabili, M. Wuttig, L. Salamanca Riba, D. G. Schlom, and R. Ramesh, Appl. Phys. Lett. **85**, 2035 (2004).

[110]. J. G. Wan, X. W. Wang, Y. J. Wu, M. Zeng, Y. Wang, H. Jiang, W. Q. Zhou, G. H. Wang, and J. M. Liu, Appl. Phys. Lett. **86**, 122501 (2005).

[111]. J. Wu, and J. Wang J. Appl. Phys. **105**, 124107 (2009)

[112]. T. Wu, M. A. Zurbuchen, S. Saha, J. Mitchellm and S. K. Streiffer, Phys. Rev. B **73**, 134416 (2006).

[113]. J. Slutsker, I. Levin, J. H. Li, A. Artemev, and A. L. Royburd, Phys. Rev. B **73**, 184127 (2006).

[114]. N. Dix , R. Muralidharan, J. M. Caicedo, D. Hrabovsky, I. Fina, L. Fabrega, V. Skumryev, M. Varela, J. Guyonnet , P. Paruch, F. Sanchez, J. Fontcuberta. J. Magn. Mag. Mat. **321** 1790–1794 (2009)

[115]. X. L. Zhong et al., Appl. Phys. Lett. **90**, 152903 (2007).

[116]. M. Liu et al., J. Appl. Phys. **102**, 083911 (2007).

[117]. C. W. Nan, G. Liu, Y. H. Lin, and H. Chen, Phys. Rev. Lett. **94**, 197203 (2005).

[118]. M. I. Bichurin , V. M. Petrov , G. Srinivasan , Phys. Rev. B (2003).

[119]. Y. Zhang, C. Deng, J. Ma, Y. Lin, C.W. Nan, Appl. Phys. Lett. **92**,062911 (2008).

[120]. Z. Li, Y. Wang, Y. Lin, C.W. Nan, Phys. Rev. B **79**, 180406R (2009).

[121]. S. Ryu, J. H. Park, H. M. Jang, Appl. Phys. Lett. **91**, 142910 (2007).

[122]. M. Ziese, A. Bollero, I. Panagiotopoulos, N. Moutis, Appl. Phys. Lett. **88**, 212502 (2006).

[123]. Y. G. Ma, W. N. Cheng, M. Ning, C. K. Ong, Appl. Phys. Lett. **90**, 152911 (2007).

[124]. H. Zheng, F. Straub, Q. Zhan, P. L. Yang, W. K. Hsieh, F. Zavaliche, Y. H. Chu, U. Dahmen, and R. Ramesh, Adv. Mater. Weinheim, Ger. **18**, 2747 (2006).

[125]. F. Zavaliche et al., Nano. Lett. **5**, 1793 (2005).

[126]. H. Zhenget al., Nano Lett. **6**, 1401 (2006).

[127]. G. A. Smolenskii, V. A.Isupov, A. I. Agranovskaya, N. N. Krainik, Sov. Phys. Solid State, **2**, 2651-2654 (1961).

[128]. C. S. Tu, I. G. Siny, V. H. Schmidt, Phys. Rev. B **49**, 11550(1994).

[129]. J. Suchanicz, J. Kwapulinski, Ferroelectr.**165**, 249 (1995).

[130]. G. O. Jones, P. A.Thomas, Acta. Crystallogr. B Struct. Sci., **58**, 168-178 (2002).

[131]. T. Takenaka, K. Sakata, Toda, K. Ferroelectr., **106**, 375-380 (1990).

[132]. S. T.Zhang, A. B. Kounga, E. Aulbach, E. Ehrenberg, Rodel, Appl. Phys. Lett., **91**, 112906 (2007).

[133]. S. T.Zhang, A. B. Kounga, E. Aulbach, T. Granzow, W. Jo, H. J. Kleebe. J. Rodel, J. Appl. Phys., **101** 034107:1-034107:8. (2008).

[134]. S. T. Zhang, A. B. Kounga, E. Aulbach, W. Jo,T.Granzow, H.Ehrenberg, J. Rodel, J. Appl. Phys., **103**, 034108 (2008).

[135]. B. Kounga, S. Zhang, W. Jo, T. Granzow, and J. R. Gel, J. Appl. Phys. Lett. **92**, 222902 (2008).

[136]. B. S. Narendra, Leszek Malkinski, J. Appl. Phys. **111,** 07D904 (2012)

[137]. N.A. Spaldin, M. Fiebig, Science **309**, 391-392 (2005).

[138]. T. Kimura, T. Goto, H. Shintani, K. Ishizaka, T. Arima, Y. Tokura, Nature (London) **426**, 55-58 (2003).

[139]. D. Lebeugle, D. Colson, A. Forget, M. Viret, A. M. Bataille, A. Gukasov, Phys. Rev. Lett. **100**, 227602 (2008).

[140]. Y. Li, Y. Fan, H. Zhang, X. Teng, X. Dong, H. Liu, X. Ge, Q. Li, W. Chen, L. Z. Ge, J. Supercond Nov. Magn. **27**, 1239–1243 (2014).

[141]. M. Muneeswaran, P. Jegatheesan, M. Gopiraman, Ick Soo Kim, N.V. Giridharan Appl. Phys. A, **114**, 853–859 (2014).

[142]. J. Wang, H. Zheng, Z. Ma, S. Prasertchoung, M. Wuttig, R. Droopad, J. Yu, K. Eisenbeiser, R. Ramesh, Appl. Phys. Lett. **85,** 2574-2576 (2004).

[143]. Q. Man, W. Sun, F. Yang, C. Qiu, Y. Zhao, G. Hu, J. Mater Sci. Mater. Electron, **25**, 1269–1274 (2014).

[144]. A. Z. Simoes, L. S. Cavalcante, F. Mourac, E. Longo, J.A. Varela, J. Alloy. Compd. **509**, 5326–5335 (2011).

[145]. X. S. Xu, T. V. Brinzari, S. Lee, Y. H. Chu, L. W. Martin, A. Kumar, S. Mc Gill, R. C. Rai, R. Ramesh, V. Gopalan, S. W. Cheong, and J. L. Musfeldt Phys. Rev. B **79**, 134425 (2009).

[146]. Z. Lin, W. Cai, W. Jiang,C. Fu, C. Li, Y. Song, Ceram. Int. **39**, 8729–8736 (2013).

[147]. C. A. Raj, M. Muneeswaran, P. Jegatheesan, N. V. Giridharan , V. Sivakumar, G. Senguttuvan, J. Mater Sci. Mater Electron, **24,** 4148–4154 (2013).

[148]. V. M. Fridkin, Crystallogr. Rep. **46**,654-658 (2001).

[149]. B.W. Ji, K. Yao, Y. C. Liang, Adv. Mater, **22**, 1763–1766 (2010).

[150]. T. Choi, S. Lee, Y. J. Choi, V. Kiryukhin and S. W. Cheong, Science **324,** 63-66 (2009).

[151]. S.Y. Yang, Appl. Phys. Lett. **95,** 062909 (2009).

[152]. A. Ivan, V. Davalos, M. Moretti, M. Nicklaus, C. Nauenheim, S. Li, R. Nechache, C. G. Yanez, A. Ruediger, Appl. Phys. A **115**, 1081–1085 (2014).

[153]. A. Z. Simões, L. S. Cavalcante, F. Moura, N. C. Batista, E. Longo, J. A. Varela , Appl. Phys. A. **109**, 703–714 (2012).

[154]. B. S. Soram, B.S. Ngangom, H. B. Sharma, Thin Solid Films **524**, 57-61(2012).

[155]. L. S. Cavalcante, J. C. Sczancoski, F. S. De Vicente, M. T. Frabbro, M. Siu Li, J. A. Varela, E. Longo, J. Sol-Gel Sci. Technol. **49**, 35–46 (2009).

[156]. M. Diana, M. Tasca, M. Delibas, G.I Rusu, Appl. Surf. Sci. **156**, 200–206 (2000).

[157]. X. Chen, H. Zhang, T. Wang, F. Wang, W. Shi, Phys. status solidi A, **209**,1456-1460 (2012).

[158]. Y. Xu, M. Shen, Mater. Lett. **62**, 3600-3602 (2008).

[159]. P. Tyagi, A. G. Vedeshwar, Bull. Mater. Sci. **24**, 297-300 (2001).

[160]. F. Gao, Y. Yuan, K. F. Wang, X. Y. Chen, F. Chen, J. M. Liu, Z. F. Ren, Appl. Phys. Lett. **89**, 102506 (2006).

[161]. L. Bi, A. R. Taussig, H. S. Kim, L. Wang, G. F. Dionne, D. Bono, K. Persson, G. Ceder, A. C. Ross, Phys. Rev. B, **78**, 104106 (2008).

[162]. Y. Wang, J. Hu, Y. Lin, C. W. Nan, NPG Asia Matter. **2,** 61-68 (2010).

[163]. A. Z. Simoes, L. S. Cavalcante, C. S. Riccardi, V. J. A, E. Longo J. Sol-Gel Sci. Technol. **44,** 269–273, (2007).

[164]. R. Mazumder, P. Sujatha Devi, Dipten Bhattacharya, P. Choudhury, A. Sen, M. Raja, Appl. Phys. Lett.**91**, 062510 (2007).

[165]. S.K. Singh, Y.K. Kim, H. Funakubo, H. Ishiwara, Appl. Phys. Lett. **88**, 162904 (2005).

[166]. M. Kumari, C. Prakash, R. Chatterjee, J. Appl. Phys, **113**, 17D918 (2013).

[167]. V. R. Palkar, Darshan C. Kundaliya, S. K. Malik, and S. Bhattacharya, Phys. Rev. B, **69**, 212102-1-212102-3 (2004).

[168]. Jing Ma, Jiamian Hu, Zheng Li, and Ce Wen Nan, Adv. Mater. **23**, 1062-1087 (2011).

[169]. Y. J. Chen , Y. H. Hsieh , S. C. Liao, Z. Hu , M. J. Huang , W. C. Kuo, Y. Y. Chin , T. M. Uen, J. Y. Juang, C. H. Lai , H. J. Lin , C. T. Chen , Y. H. Chu, Nanoscale, **5**, 4449 (2013).

[170]. Feng Yan, Guannan Chen, Li Lu, Peter Finkel, Jonathan E. Spanier, Appl. Phys. Lett. **103**, 042906 (2013).

[171]. Ying Hui Hsieh, Ho-Hung Kuo, Sheng Chieh Liao, Heng-Jui Liu, Ying-Jiun Chen, Hong-Ji Lin, Chien-Te Chen, Chih-Huang Lai, Qian Zhan, Yu-LunChueh Ying-Hao Chu. Nanoscale, **5**, 6219 (2013).

[172]. N. C. Pramanik, T. Fujii, M. Nakanishi, J. Takada, J. Math. Chem. **14**, 3328-3332 (2004).

[173]. MintuTyagi , MukeshKumari , RatnamalaChatterjee , An-Cheng Sun and Puneet Sharma, IEEE Trans. Magn:article in press, **50** (2014).

[174]. M. K. Singh, H. M. Jang, S. Ryu, M. H. Jo, Appl. Phys. Lett. **88**, 042907 (2006).

[175]. M. G. Majumdar, Inter. J. Sci. and Engg. Res. **3**,11(2012).

[176]. J. Kreisel, G. Lucazeau, and H. Vincent, J. Solid State Chem. **137**, 127 (1998).

[177]. O. Chaix-Pluchery, C. Cochard, P. Jadhav, J. Kreisel, N. Dix, F. Sánchez, J. Fontcuberta Appl. Phys. Lett. **99**, 072901(2011).

[178]. Zuli Liu, Hongri Liu, Guihuan Du, Jian Zhang, Kailun Yao, J. Appl. Phys. **100**, 044110 (2006).

[179]. (a) Jian-Qing Dai, Yu-Min Song, and Hu Zhang, J.Appl. Phys., **111**, 114301-1-114301-6 (2012). (b) M. C. Dimri, A. Verma, S. C. Kashyap, D. C. Dube, O. P. Thakur, and C. Prakash, Mater. Sci.Eng. B, **133**, 42-48 (2006). (c) S. E. Shirsath, B. G. Toksha, and K. M. Jadhav, Mater. Chem. Phys., **117**, 163-168 (2009).

[180]. V. R. K. Murthy, Sobnandari, J. Phys. Status Solidi A, **36**, 133-137 (1976).

[181]. B. Sarkar, B. Dalal, D. A. Vishal, C. Kaushik, M. Amitava, and S. K. De , J. Appl. Phys. **115**, 123908 (2014).

[182]. S. P.Crane, C. Bihler, M. S. Brandt, S. T. B. Goennenwein, M. Gajek, R. Ramesh, J. Magn. Magn. Matter. **321**, 5–9(2009).

[183]. N. Benatmane, S. P. Crane, F. Zavaliche, R. Ramesh, and T. W. Clinton, Appl. Phys. Lett. **96**, 082503 (2010).

[184]. J. Gu, S. Yang, W. Yang, Y. Qi, G. Zhao, H. Sun, J. Magn. Magn. Matter. **349**, 140–143 (2014).

[185]. Q. Zhan, R. Yu, S. P. Crane, H. Zheng, C. Kisielowski, and R. Ramesh, Appl. Phys. Lett. **89**, 172902 (2006).

[186]. J. F. Scott, J.Phy: Condens Matter **20**, 021001 (2008).

[187]. S. K. Upadhyay and V. R. Reddy, J. Appl. Phys. **113**, 114107 (2013).

[188]. C. G. Koops, Phys. Rev.**83**, 121 (1951).

[189]. K. W. Wagner, Ann Phys. **40**, 818 (1993).

[190]. S. N. Babu, J. H. Hsu, Y. S. Chen, and J. G. Lin, J. Appl. Phys. **107**, 09D919 (2010).

[191]. C. W. Nan, M. I. Bichurin, S. Dong, D. Viehland, G. Srinivasan, J. Appl. Phys. **103,** 031101 (2008).

[192]. D K. Pradhan, R. N. P. Chaudary, T. K. Nath, Appl. Nanosci. **2,** 261-273 (2012).

[193]. Q. Jiang, F. Liu, H. Yan, H. Ning, Z. Libor, K. Q. Zhang, K. M. Cain, and M. J. Reece, J. Am. Ceram. Soc. **94,** 2311–2314 (2011).

[194]. L. P. Curecheriu, M. T. Buscaglia, V. Buscaglia, L. Mitoseriu, P. Postolache, A. Ianculescu, P. Nanni, J. Appl. Phys. **107,** 104106 (2010).

[195]. M. Zeng, J. G. Wan, Y. Wang, H. Yu, J. M. Liu, X. P. Jiang, and C. W. Nan, J. Appl. Phys. **95,** 8069 (2004).

[196]. A. D. Sheikh, A. Fawzi, V. L. Mathe, J. Magn. Magn. Matter. **323,** 740 (2011).

[197]. K. Chang, W. Feng, L. Q. Chen, Acta Materialia, **57,** 5229–5236 (2009).

[198]. Y. Guo, M. Gu, H. Luo, Y. Liu, and R. Withers Phys. Rev. B, **83** 054118 (2011)

[199]. D. K. Pradhan, S. K. Barik, S. Sahoo, V. S. Puli, and R. S. Katiyar, J. Appl. Phys. **113,** 144104 (2013).

[200]. A. Gupta, R. Chatterjee, J. Magn. Magn. Matter. **322,** 1020 (2010).

[201]. M. Lorenz, V. Lazenka, P. Schwinkendorf, F. Bern, M. Ziese, H. Modarresi, A. Volodin, M J V Bael, K. Temst, A. Vantomme and G. Marius, J. Phys. D: Appl. Phys. **47** 135303 (2014)

[202]. C. M. Kanamadi, L. B. Pujari, B. K. Chougule, J. Magn. Magn. Matter. **295** 139 (2005)